

CHAPTER 2

Experiment

2.1 Introduction

A variety of experiments are performed for this thesis. For the studies of cluster formation dynamics and large amplitude motion in weakly bound complexes, the species of interest are formed in a pulsed slit supersonic expansion and probed via direct absorption of a tunable Pb-salt diode laser. Both CO₂ complexes in the ν_3 asymmetric stretch region (4.3 μm) and H₂O complexes in the ν_2 bend region (6.2 μm) are investigated using high resolution spectroscopy techniques. For the studies of rotational alignment in a supersonic expansion, CO₂ is expanded in either a pinhole or slit pulsed supersonic expansion, and the alignment is detected via the polarization dependent direct absorption of a tunable Pb-salt diode laser in the ν_3 asymmetric stretch region. Finally, for the study of CO₂ sublimation dynamics from bulk CO₂, thin films are grown in vacuum at 77 K, warmed to some temperature from 90 to 115 K, and the nascent translational, vibrational, and rotational distributions of the subliming species are measured via direct absorption in the ν_3 asymmetric stretch region. In addition, polarization modulation techniques are used to probe for rotational alignment of the subliming CO₂.

Although particulars for each experiment are briefly covered in each chapter, each experiment has elements that warrant further description. Clearly the heart of all the experiments performed herein is the infrared diode laser spectrometer shown in Fig. 2.1, which will be discussed in detail. Then additions and modifications unique to particular studies will be covered, such as gas handling and supersonic expansions, the

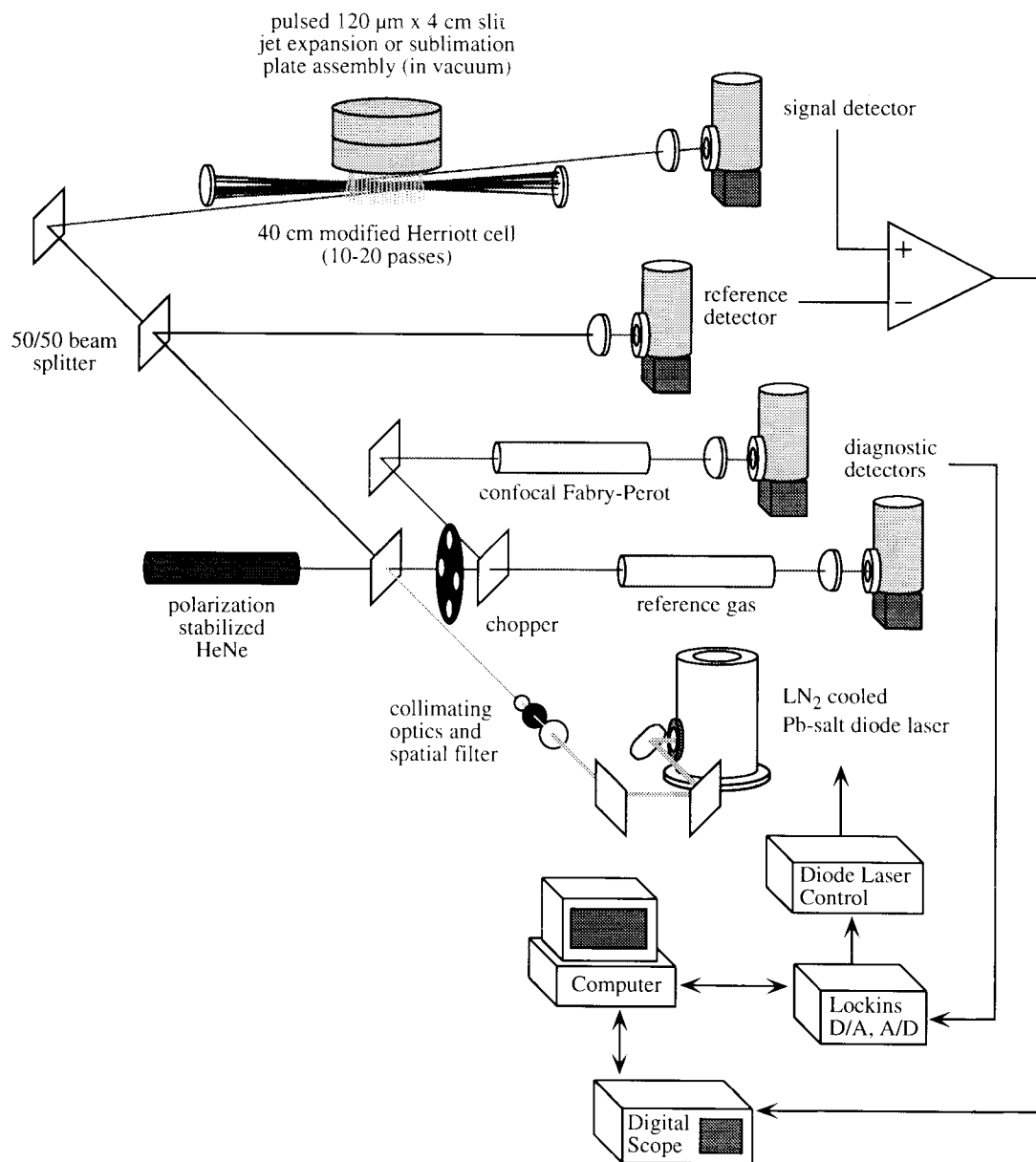


Fig. 2.1: Infrared diode laser spectrometer. This is the general form of the spectrometer; modifications and additions for the various experiments are discussed in detail below.

detection of alignment via the polarization modulation technique, and the cryogenic growth and sublimation of CO₂ thin films. Finally, data acquisition and analysis are considered.

2.2 Pb-salt diode laser

Pb-salt diode lasers provide a relatively inexpensive and efficient way to generate tunable laser light over the 3 to 30 μm wavelength range. In addition to being easy to use, the frequency of these lasers can be rapidly modulated at rates of up to a GHz, making them ideal for the detection of cw absorptions, such as the subliming flux from a thin film. The narrow line width (≤ 15 MHz) is suited for Doppler limited high resolution spectroscopy, and the intrinsically low amplitude noise ($< 10^{-3}$ on a 200 μs time scale) leads to a routine detection sensitivity of $10^{-6}/\sqrt{\text{Hz}}$. There are several books¹⁻³ and reviews^{4, 5} on near ($\lambda \lesssim 3 \mu\text{m}$) and mid ($3 \lesssim \lambda \lesssim 30 \mu\text{m}$) infrared diodes, and an overview of the principles of diode laser operation from these texts is presented in the next section. Then the actual operation of the diode is considered.

2.2.1 Principles of operation

The elements of a laser for a Pb-salt diode, *i.e.*, an optical gain medium and feed-back cavity, are provided by a piece of semiconductor with cleaved ends. As shown in Fig. 2.2, the Fermi level for a semiconductor lies midway between the valence and conduction bands. The band gap (E_{gap}) is such that the majority of the electrons do not have enough thermal energy to access the conduction band. However, a photon with $h\nu > E_{\text{gap}}$ can excite an electron to the conduction band, leaving behind a hole. The opposite process can occur, namely, combination of an electron in the conduction band with a hole, to produce a photon with frequency $\nu \approx E_{\text{gap}}/h$. Given a

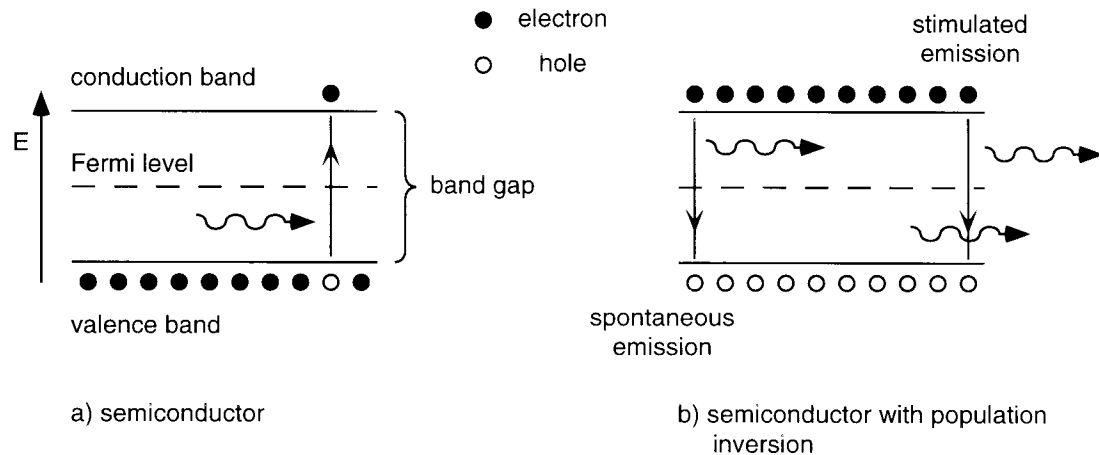


Fig. 2.2: Semiconductor as an optical gain medium. If a population inversion can be formed, electron/hole pairs can be stimulated to recombine, releasing a photon of frequency $\nu \approx E_{\text{gap}}/h$.

population inversion of holes and electrons, electrons can be stimulated to recombine with holes by a photon, creating an optical gain medium.

To create a population inversion in a semiconductor, a p-n diode junction⁶ is used, as shown in Fig. 2.3. The semiconductor is doped with an impurity which typically has one too many or too few valence electrons to bond completely with the semiconductor lattice. This creates either an electron that is very easy to remove from the impurity (known as an n-type impurity), or a "hole" for a neighboring lattice electron to occupy (known as a p-type impurity). Because it takes relatively little energy compared to the semiconductor band gap to excite one of these impurity electrons to the conduction band, or to move valence band electrons into these holes, the impurity electrons and holes can diffuse through the lattice from thermal excitation alone. Also, this moves the Fermi level so that it is just below the conduction band for an n-type material, and just above the valence band for a p-type. As shown in Fig. 2.3a, when a junction is formed between an n and p-type material, holes and electrons diffuse into the junction and recombine. When this occurs, the initially neutral impurity gains a charge. This process continues until the net charges across the junction from

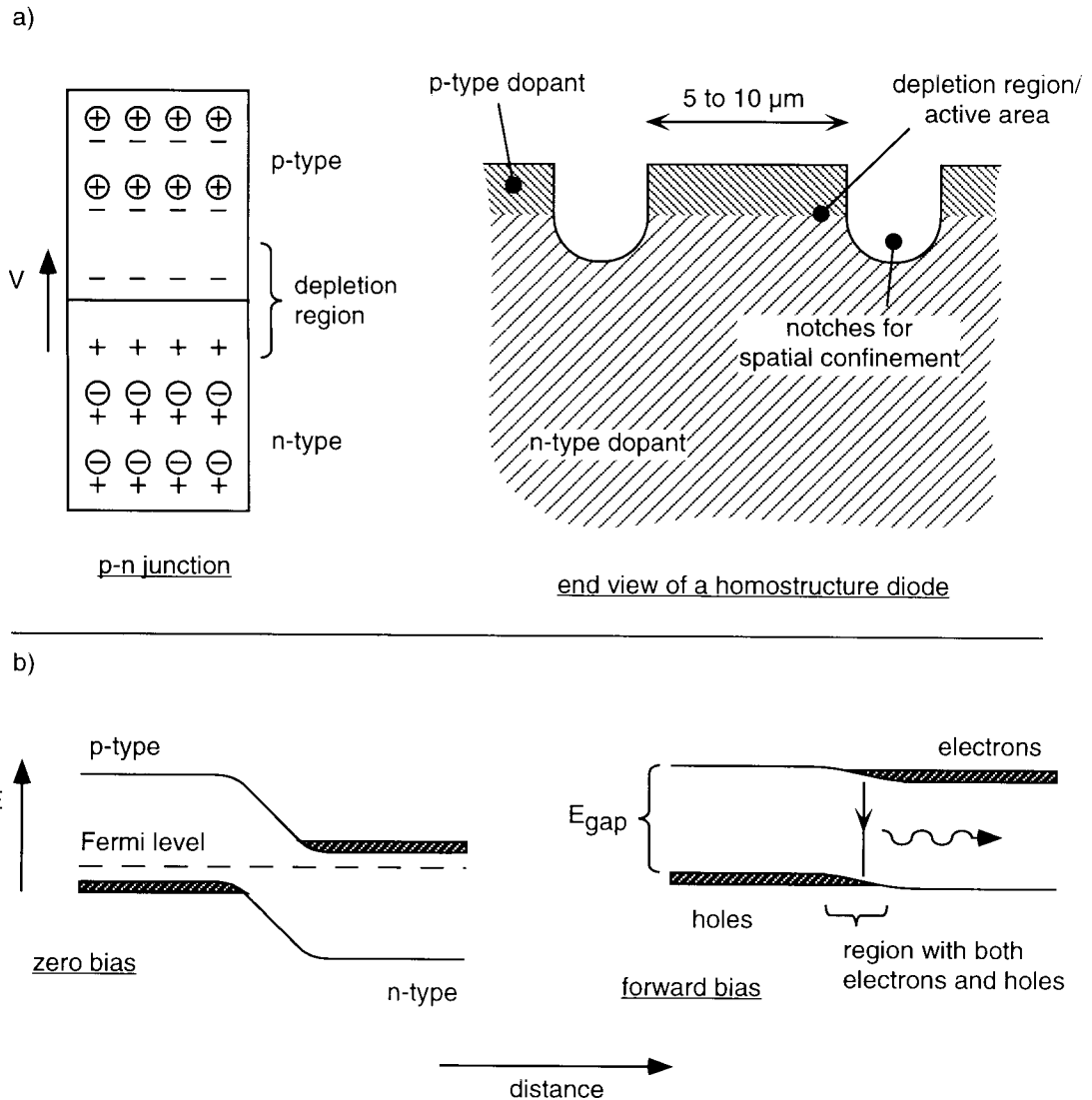


Fig. 2.3: a) p-n junction of a homostructure diode laser. Forward biasing of the junction provides the electron/hole pairs necessary to create a population inversion in the semiconductor. Electrical contact to provide a forward bias is made directly above the active area, and at the base of the diode. b) Fermi diagrams for a p-n junction. For a doped semiconductor, thermal energy places electrons in the conduction band and holes in the valence band. Applying a forward bias to the junction brings the electron/hole pairs into the same region, where they can recombine to form photons.

thermal recombination create a large enough potential such that further electrons and holes do not possess enough energy to diffuse into the junction. This sets up a depletion region with a voltage drop across it.

Another way to represent the p-n junction is with a Fermi-diagram, shown in Fig. 2.3b. The process of thermal recombination leading to the depletion region is equivalent to the n and p-type materials coming to chemical equilibrium. This occurs when the Fermi level is continuous across the junction. As can be seen, the voltage formed across the depletion region is an energy "step" in the Fermi diagram that keeps electrons in the conduction band and holes in the valence band from occupying the same region of space in the semiconductor. If, however, an external voltage is applied to the p-n junction, *i.e.*, it is forward biased, the voltage across the depletion region can be overcome, and electrons and holes are forced into the same region of the semiconductor. They can then recombine, emitting a photon. The external biasing continually injects more electrons and holes into this "active region," providing the population inversion necessary for lasing.

The simplest diode lasers are based upon this p-n junction for the optical gain medium, and are known as homojunction, or homostructure lasers. The 6.2 μm diode (Laser Photonics, model L5621-1600, serial number 5061-07) used to probe the ν_2 bend of H_2O in the present study is a homostructure diode, and a detail of the active area is shown in Fig. 2.3a. In order to provide the other ingredient necessary for lasing, *i.e.*, optical feedback, the ends of the diode are cleaved. Since the index of refraction for Pb-salt semiconductors is ≈ 5 at 6 μm , this provides a mirror with $\approx 44\%$ reflectance. The cavity thus formed is approximately 250 μm long, and is defined to be 5 to 10 μm wide by etching two grooves through the homojunction. The thickness of the active region can vary over a few tenths of a μm , and is not as well defined since the junction is formed by diffusion of an impurity through the semiconductor.

At this point it is worthwhile to discuss the actual semiconductor materials the diodes are made from. It is important to remember that the p-n junction simply provides a means to create a population inversion, and that the material the diode is

based upon must be an intrinsic semiconductor. Additionally, it must be a direct band gap semiconductor, such that transitions from the maximum of the valence band to the minimum of the conduction band do not involve a change in the momentum vector \mathbf{k} of the electron. In the near infrared, the binary semiconductors formed from elements in columns III and V of the periodic table satisfy this criterion, while for wavelengths longer than $3 \mu\text{m}$ the binary complexes SnTe, PbTe, PbS, PbSe, and SnSe are all direct band gap semiconductors. Moreover, these complexes all form a cubic rock salt structure, so it is possible to grow ternary complexes such as $\text{Pb}_{(1-x)}\text{Sn}_x\text{Te}$ or $\text{Pb}_{(1-x)}\text{Sn}_x\text{Se}$ that have band gaps intermediate to the binary complexes. In this way the band gap can be "tuned" by varying the composition. For particular compositions of $\text{Pb}_{(1-x)}\text{Sn}_x\text{Te}$ and $\text{Pb}_{(1-x)}\text{Sn}_x\text{Se}$ the band gap actually goes to zero, so in principle it is possible to make semiconductor lasers for arbitrarily long wavelengths, though in practice wavelengths only out to $34 \mu\text{m}$ have been observed.¹ The homostructure diode used in the H_2O studies is based upon the ternary semiconductor $\text{PbS}_{(1-x)}\text{Se}_x$, where $x \approx 0.7$.

The ability to vary the band gap of these semiconductors by forming ternary or even quaternary complexes leads to a refinement of the diode laser optical gain medium that enhances the efficiency and improves the mode quality of the beam. The second diode laser used in the $4.3 \mu\text{m}$ region to study the ν_3 symmetric stretch of CO_2 is a heterostructure laser (Laser Photonics, model L5622-2100, serial number 87-05). The composition of its active area is $\text{Pb}_{(1-x)}\text{Eu}_x\text{Se}_{(1-y)}\text{Te}_y$, where x and y are ≈ 0.01 . This laser is grown using molecular beam epitaxy (MBE), so the thickness and dimensions of the different semiconductor layers can be precisely determined. A schematic of the heterostructure laser is shown in Fig. 2.4a. Notice that the active layer is undoped, and is surrounded above and below by an n and p-type layer. These cladding layers have slightly different compositions than the active area, and thus have a larger band gap; the

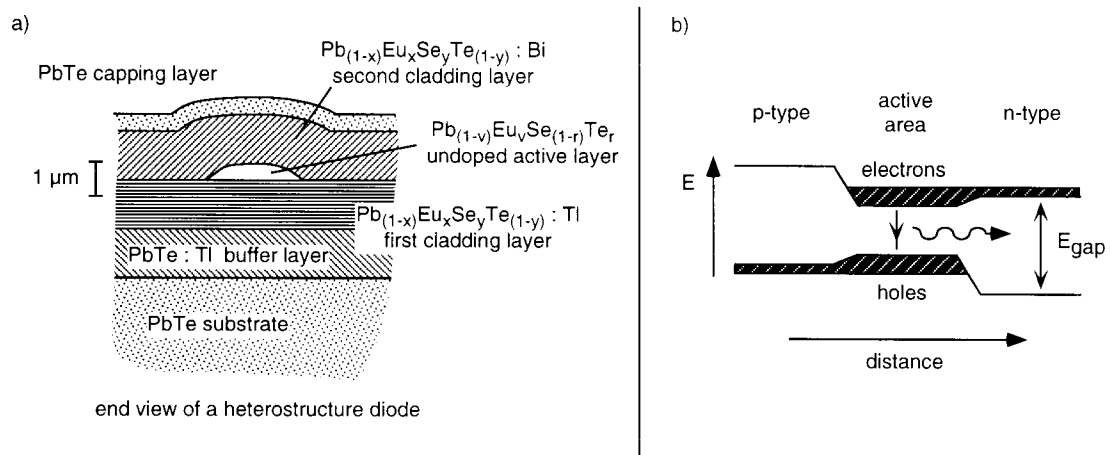


Fig. 2.4: a) Structure of a Pb-salt heterostructure diode laser. By growing these diodes via MBE, the active layer is small and well defined. Electrical contact is made directly above the active region and at the base of the diode. The n or p-type impurity for each layer is listed after the colon. The substrate and capping layers are also doped with Tl and Bi, respectively. b) Fermi diagram of a forward-biased heterostructure diode. Because the p and n-type cladding layers have larger band gaps than the active layer, the electron/hole pairs are confined to a well defined region for recombination.

Fermi diagram for the diode under forward bias is in Fig. 2.4b. With a heterostructure, the electrons and holes are effectively confined to a well defined region for recombination. In addition, the cladding layers have a different index of refraction, leading to a well defined wave guide for the radiation.

To start the lasing in a diode, it is necessary for the round trip cavity gain in photons due to stimulated emission to be greater than the losses. Photons are lost due to reabsorption by the semiconductor, movement out of the active region, or the $\approx 56\%$ transmission at the cleaved ends. In addition, electron/hole pairs injected into the active area can recombine nonradiatively. This type of loss must be compensated by a greater injection current. There are two main nonradiative loss mechanisms: the first is due to electron/hole recombination at lattice defect sites, and the second is due to Auger processes, which is the dominant loss mechanism for Pb-salt diodes.¹ The Auger process involves exciting a second electron in the conduction band to a higher energy

level during the primary recombination, or even excitation of a lower energy electron in the valence band to a hole. This process usually involve a change in the momentum \mathbf{k} of the electrons and is often phonon assisted. The Auger process tends to become more important for smaller band gaps and higher temperatures. Therefore, it is a far greater loss mechanism for the Pb-salt diodes than the near infrared diodes, and is the reason that the Pb-salt diodes must be cooled below 120 K before lasing is observed. This is achieved in the present study by mounting the diodes in a vacuum sealed dewar in thermal contact with a liquid N₂ reservoir (Laser Photonics, model L5736).

When the injection current is large enough that radiative recombination leads to an optical field that can reproduce itself via stimulated emission for each round trip through the cavity, the lasing threshold is reached. For the diodes used in the present study, the threshold current rises from approximately 50 mA at 80 K, to over 200 mA for temperatures in excess of 110 K. The principle reason for this rise is the increasing importance of the Auger process at higher temperatures, which leads to greater nonradiative loss of electron/hole pairs. Although these currents may not seem large, when divided by the actual active area of the diode they translate into currents of 20 kA/cm², highlighting the density of electron/hole pairs needed for lasing.

When considering the lasing properties of the different diodes, the heterostructure lasers tend to be preferable to the homostructure lasers for several reasons. First, the spatial mode quality of the laser beam is improved by the well defined active region. In the present study, it is much more difficult to collimate and focus the beam from the homostructure laser than from the heterostructure laser. Second, concentration of the electron/hole recombination to the active region enhances the efficiency. Threshold currents for lasing are lower, and the heterostructure lasers therefore operate at higher temperatures. Lastly, the heterostructure lasers tend to have better frequency mode structure, often lasing in a single mode (>95% power in one

frequency mode) over a wide range of currents and temperatures. However, the homostructure lasers are easier to produce, since the p-n junction is formed by diffusion, which is a simpler manufacturing process than MBE. Lasers for frequencies less than $\approx 1600 \text{ cm}^{-1}$ are only available as homostructures from Laser Photonics, the only maker of Pb-salt diodes in the U.S. This is likely to change in the next few years, though, as the demand increases for diodes that operate at higher temperatures.

2.2.2 Frequency tuning and noise characteristics

There are two main ways to tune the frequency of the Pb-salt diode lasers. Coarse tuning is achieved by changing the temperature of the diode. For the Pb-salt semiconductors, the band gap increases with temperature at a rate of $3 - 4 \text{ cm}^{-1}/\text{K}$. It should be noted that this is an intrinsic property of the semiconductor material, and is not due to the p-n junction. Also, this is opposite than for near infrared diodes; the band gap of the III-V semiconductors *decreases* with increasing temperature. This dependence of the band gap on temperature can be exploited to tune the diode in discrete steps over nearly 100 cm^{-1} . To do this, the diodes are first cooled to liquid N_2 temperatures in a dewar, and then resistively heated over the range of 80 to 120 K. At temperatures greater than 120 K, the Auger processes dominate the electron/hole recombination, and lasing is not observed.

To achieve the level of frequency stability necessary for Doppler limited spectroscopy, frequency drifts of the diode should be less than $\approx 10 \text{ MHz}$ over a few seconds. Therefore, the temperature servo must be able to achieve a set point from 80 to 120 K, and be stable to 0.1 mK on a time scale of seconds. The temperature servo (Laser Photonics, model SP5720) uses the voltage drop across a silicon diode to determine the temperature, and a $13 \text{ } \Omega$ heater attached to a plate in contact with the diodes as well as the liquid N_2 reservoir via a cold finger to control the temperature.

This proportional and integral servo loop has a specified stability of ± 0.001 K over 10 min, and it is found that the servo is stable enough to average repeated sweeps over a single 75 MHz full width half maximum (FWHM) absorption profile taken over a 10 second interval without any discernible broadening of the line shape.

Fine tuning of the diode laser is achieved by varying the current. This has two effects: the first is a small amount of resistive heating in the active area that temperature tunes the band gap *and* changes the index of refraction, which is also temperature dependent. The second effect is a change in the index of refraction of the active area due to the changing charge density. It is the changing index of refraction that leads to continuous tuning of the diode frequency by effectively changing the cavity length; this process will be considered in detail in Sec. 2.2.5. For the present discussion, however, the typical current tuning rate of a Pb-salt diode is ≈ 1 MHz/ μ A. Therefore, the current supply should be variable and able to supply up to 500 mA (the maximum current for most MBE diodes), plus have current noise of well under 1 μ A in a 10 kHz bandwidth (for fast frequency sweeps) to prevent broadening of the laser linewidth. This is actually a serious issue for diode laser spectroscopy. For example, the best current supply sold by Laser Photonics has a stated current noise of 15 μ A rms in a 10kHz bandwidth. This leads to additional frequency noise on the diode laser of ≈ 15 MHz rms, exceeding the 10 to 20 MHz Doppler widths of most species in the supersonic expansion. Therefore, two current supplies have been used in the present study. The first is a modification of a circuit designed by the Hall labs,^{4, 5} and the diagram is shown in Fig. 2.5. This supply can provide up to 300 mA, with current noise of 160 nA rms in a 10 kHz bandwidth. More recently, a battery powered supply was purchased from ILX Lightwave (model LDX-3620), which can drive up to 500 mA with a stated current noise of 500 nA rms in the same bandwidth.

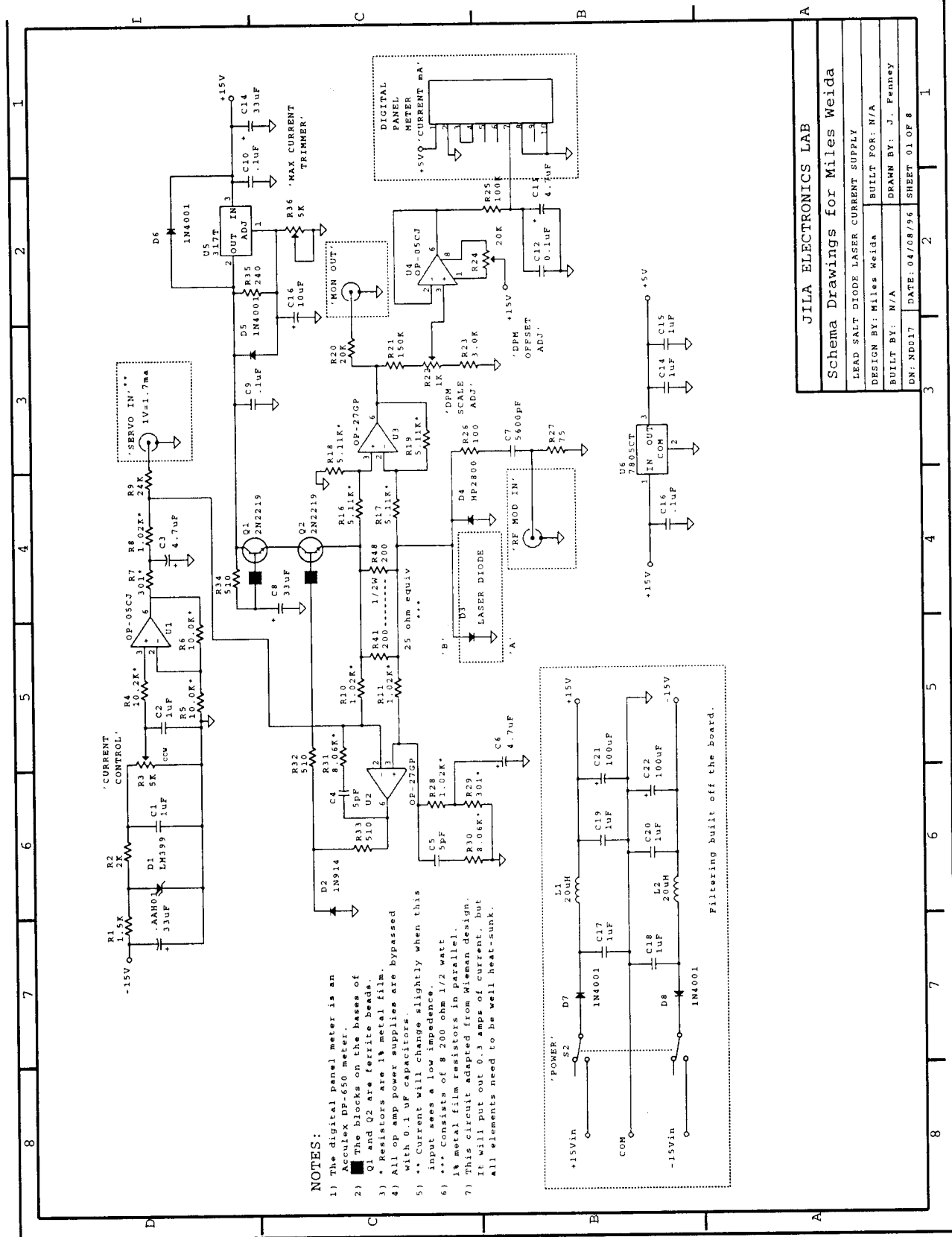


Fig. 2.5: Home built Pb-salt diode laser current supply (based on a design from the Hall labs).

Even after the stability of the temperature servo and current supply is optimized, frequency noise is still observed on the diode laser light. For the heterostructure diode used in the CO₂ studies, the linewidth and line shape of the frequency noise is determined by measuring room temperature CO₂ line shapes in a static cell. The pressure in the cell is ~ 0.1 torr, so pressure broadening is negligible and the measured line shape should be due to Doppler broadening alone, *i.e.*, Gaussian with a FWHM consistent with room temperature. The measured line shapes are slightly broader than expected, however, and in a Voigt deconvolution it is found that the additional broadening is best represented by a Lorentzian with a FWHM of ≈ 15 MHz. This frequency noise is most likely not due to instrumental factors, but is intrinsic to the diode. Free running diode lasers often exhibit linewidths on the order of 10 to 100 MHz. This has been attributed to small changes in the refractive index due to fluctuation in charge density in the active region.⁷ The intrinsic frequency noise can vary from diode to diode, and sometimes from mode to mode for the same diode. Each diode must therefore be tested when it is bought to insure that its intrinsic frequency noise is acceptable.

A relatively simple way to characterize the frequency noise of a diode is by parking the frequency of the laser on the side of an absorption profile or etalon fringe. As shown in Fig. 2.6, this creates a frequency to amplitude transducer, and the measured amplitude noise can be related to the frequency noise. In addition, an approximate measure of the spectral density of the laser frequency noise can be made using this same method. First, the laser is parked on the side of an absorption profile, and the amplitude noise is sent to a fast Fourier transform (FFT) device to record the spectral density of the noise. Since the measured amplitude noise spectrum contains noise due to the transduced frequency noise *plus* the amplitude noise of the laser light and any additional noise due to the detector a similar measurement is made with the

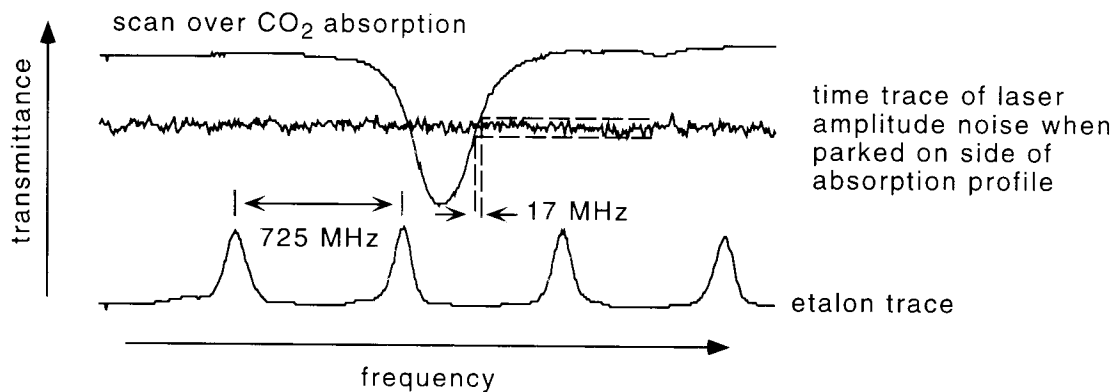


Fig. 2.6: Frequency to amplitude noise transducer.

laser frequency not on the side of the absorption profile. If the absorption profile does not attenuate a significant fraction of the light, this provides an approximate noise floor that can be subtracted from the first spectrum to obtain a true measurement of the frequency noise spectrum. Since incoherent noise adds in quadrature, *i.e.*, $V_{\text{tot}} = (V_1^2 + V_2^2)^{1/2}$, the subtraction is carried out accordingly; the resulting frequency noise spectral density for the heterostructure diode is shown in Fig. 2.7.

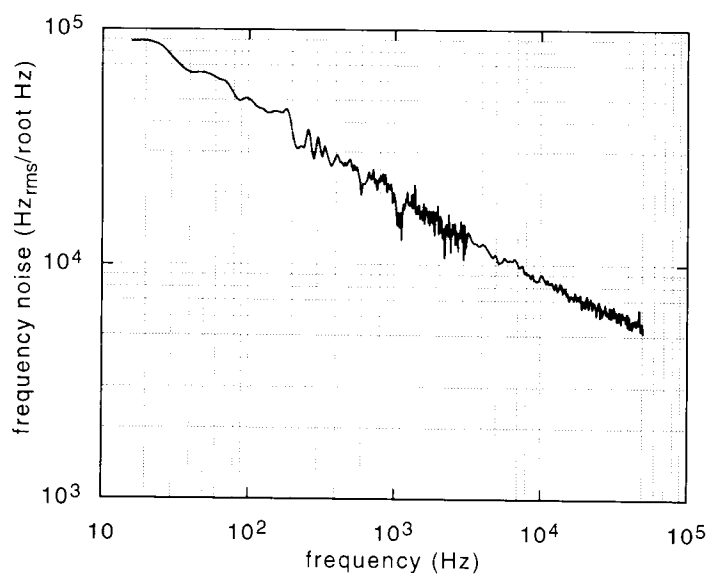


Fig. 2.7: Spectral density of heterostructure diode laser frequency noise.

The spectral density of the frequency noise provides a diagnostic to determine whether low frequency instrumental contributions such as 60 Hz modulation of the current supply are responsible for a large fraction of the frequency noise. As can be seen, the noise drops smoothly with increasing frequency and it appears that additional components due to instrumental factors are not present. This smooth drop is quite similar to measurements made for AlGaAs diodes,⁴ where the noise peaks at low frequencies and steadily decreases for frequencies out to 10^7 Hz. It is then relatively flat until $\sim 10^{10}$ Hz, at which point relaxation oscillations become important (see ref. 4). Due to detector bandwidth limitations, the noise spectrum here is recorded only out to 50 kHz, but the drop off of the noise with increasing frequency is consistent with the near IR diode measurements. In addition, the magnitude of the frequency noise is consistent with the measured linewidth of ≈ 15 MHz. We also mention that the diode laser light has amplitude noise on it as well. This will be discussed in Sec. 2.3 along with signal subtraction for the detectors.

2.2.3 *Beam collimation*

As can be seen in Figs. 2.3 and 2.4, the active area of the diode is comparable to or smaller than the actual wavelength of the light being emitted. Therefore, due to diffraction effects, the exiting beam will expand in roughly a 30° cone. Moreover, since the emitting area is rectangular, the beam is elliptical and can be astigmatic. Also, there can be spatial mode structure in the active region that leads to nodes across the beam profile. Clearly the diode beam is not Gaussian, and it must be collimated and given a reasonable spatial profile to be made useful.

The initially expanding beam can be collimated with an off-axis parabola mirror or a lens; an aluminum, diamond-turned 90° off-axis parabola with a focal length of 1.5" is used in the current experiment. As shown in Fig. 2.8, the focal length of the

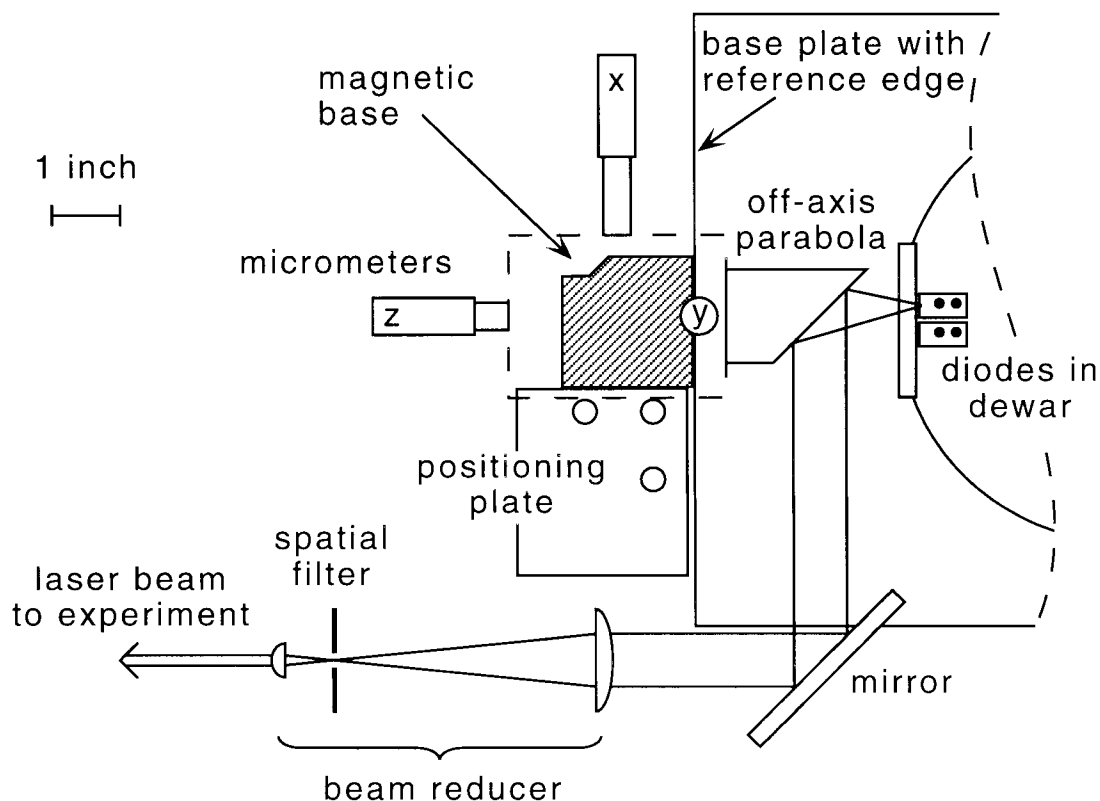


Fig. 2.8: Optics layout for diode laser beam collimation and reduction. The second lens of the beam reducer and the spatial filter are both on x , y , z translation stages as well for fine adjustment.

off-axis parabola is chosen so that it can be placed as close as possible to the exiting diode beam to insure that the resulting collimated beam is as small as possible. The spatial restrictions of the liquid N_2 dewar, however, limit how close the collimating element can be placed to the diode, and the resulting collimated beam has a $1/e$ electric field radius, *i.e.*, a spot size, of ≈ 1 cm.

This initial collimation is one of the trickier aspects of using Pb-salt diodes, particularly since there is no way to "see" the infrared radiation at 4 or 6 μm . Therefore, the steps for doing this are covered here. The off-axis parabola is on an x , y , z translation stage, which is mounted on a magnetic base. This was designed so that

the optic is square to the table and the front of the magnetic base. The dewar that holds the diodes is mounted on a base plate that has a reference edge in front of the diodes. This reference edge was also designed to be square to the exiting diode beam. Therefore, by sliding the edge of the magnetic base along the reference edge of the base plate, the optic is ensured to be square to the exiting laser beam. This provides coarse positioning in one dimension. A positioning plate that bolts into the optics table provides the second constraint, as shown in Fig. 2.8. Sliding the magnetic base along the reference edge then snug to this plate provides a kinematic system to place the off-axis parabola in approximate position.

Now that this element is square to the laser beam, the micrometers on the translation stage can be used to precisely position the off-axis parabola such that its focal point is at the emitting area of the diode laser. To get an approximate position, it is useful to expand a HeNe laser beam to ≈ 0.5 cm diameter, ensure that it is 4" above the table, then bring the HeNe beam along the reverse path the diode laser beam will take. In this way, the HeNe beam will be focused by the off-axis parabola. Using a magnifying glass, one can adjust the micrometers on the translation stage until the HeNe beam is focused on the approximate location of the emitting area on the diode.

Next a suitable infrared detector is placed about 30 cm from the diode laser along the path the HeNe beam took, as shown in Fig. 2.9. A chopper wheel is placed directly in front of the detector aperture to chop the incoming IR light so that it can be viewed on an oscilloscope. When the diode laser is turned on, there should already be light on the detector from this coarse alignment. If not, adjusting the x or y micrometers (see Fig. 2.8) on the off-axis parabola should bring light on the detector.

Once there is light on the detector, the z micrometer can be used to focus the light down on the detector using the off-axis parabola alone, shown in Fig. 2.9. Typically the x and y positions have to be optimized for every movement in the z

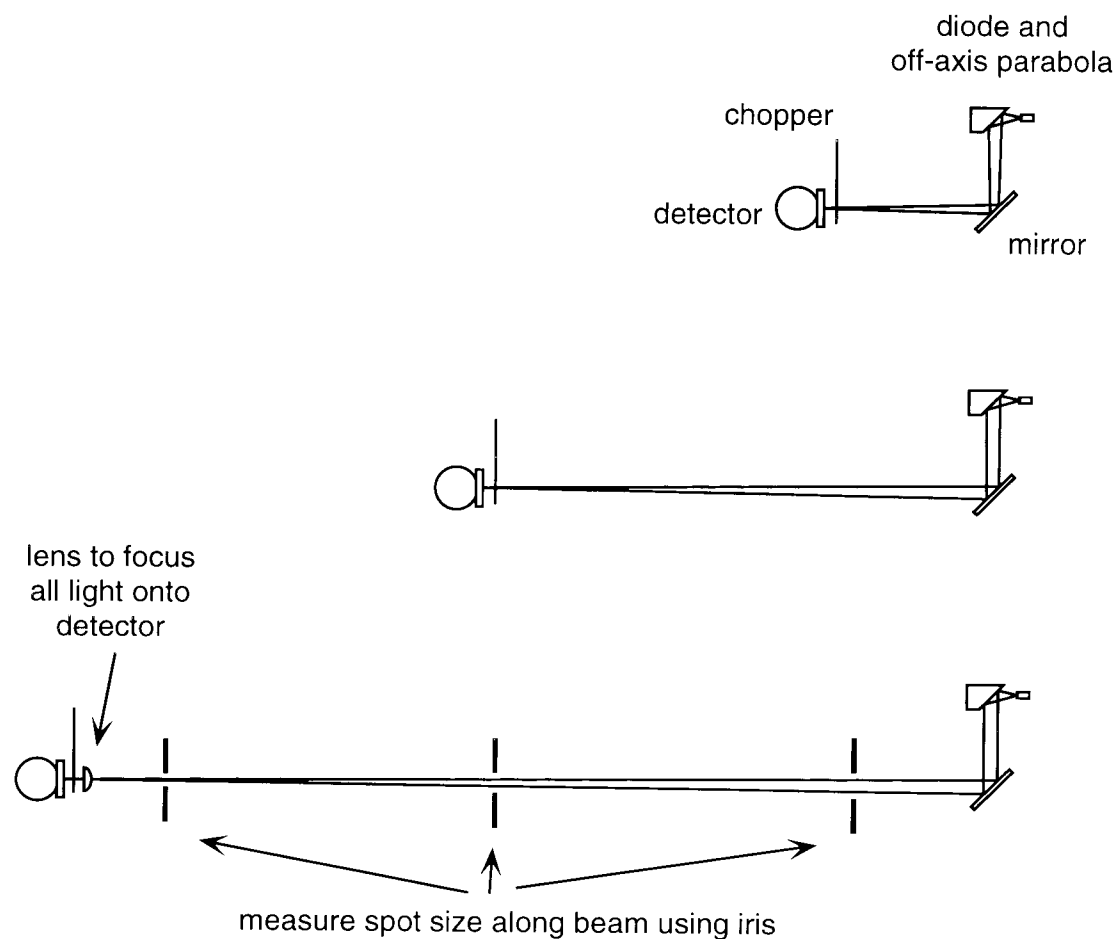


Fig. 2.9 Procedure for collimating diode laser beam using off-axis parabola.

direction. When as much light as possible is focused on the detector element, a 5 cm focal length CaF_2 lens is inserted to ensure that the entire IR beam is on the detector; the off-axis parabola typically does not focus this non-Gaussian beam to a spot smaller than the 1.0 mm diameter detector element. Once the lens is in place, a note card can be used to ensure that the IR beam is squarely on all of the mirrors and lenses, and is not clipping any element (some of the diodes have divergent beams that overfill the off-axis parabola; unfortunately, because of space restrictions, there is nothing that can be done

about this without buying a larger mirror with a longer focal length, leading to an even larger collimated beam).

The size of the diode beam can now be determined by moving an iris along the beam. If the iris is closed down so that 40% of the power is transmitted, then the diameter of the iris is equivalent to the $1/e$ electric field radius for a Gaussian beam. Of course the diode beam is not Gaussian, but this is a useful approximation. In this way, the spot size as a function of distance away from the off-axis parabola can be determined, and also whether the beam is actually being focused down. This focusing process is then repeated for progressively farther distances of the detector from the laser, as shown in Fig. 2.9. If this process could be carried out to infinite distances, the beam would be nearly perfectly collimated. In practice, it is usually adequate to do this until the detector is about 3 m from the diode. Typically this is accomplished by moving the detector 50 cm back, then repeating the focusing procedure. When the divergence of the IR beam is $\leq 0.4^\circ$ over the first 40 cm after the first turning mirror (see Fig. 2.8), this is found to be adequate to continue on to the next step of reducing the beam size.

It cannot be over stressed how important it is to approach this task with a calm mind and caffeine free hands. Write down the final x , y , and z positions of the micrometer after each step, so that hours of work can be recovered if the next step does not work. Once this procedure has been completed for a particular diode in a particular position in the dewar, the optimized settings can be quickly recovered when realigning the diode by using the kinematic positioning shown in Fig. 2.8, and the previous optimized micrometer settings, usually without having to go through the entire focusing down/stepping back procedure.

Once the beam is collimated by this procedure, it still has a spot size of ≈ 1 cm, so it is necessary to use a 5 to 1 reducer to bring it to a manageable size. This is shown

in Fig. 2.8. The first element is a 10 cm focal length, 1.5" diameter plano-convex CaF₂ lens, centered on the beam in a rigid mount. The second element is a similar lens, but with a 2 cm focal length and 0.5" diameter. The second lens is mounted on an x, y, z translation stage so that its focal point can be aligned with the first lens. To align the second element, repeat the focusing/stepping back procedure carried out for the off-axis parabola, but now with this second lens. Due to the non-Gaussian character of the beam, it is usually not possible to focus the beam down for distances of > 30 cm from the lens. Therefore, a $100 \mu\text{m}$ diameter spatial filter, also mounted on an x, y, z translation stage, is inserted at the focal point of the beam reducer to block any non-Gaussian beam elements that do not focus. Once this is done, the beam after the second element can usually be collimated to a 2 mm spot size over 2 m. The resultant beam can be steered through two irises and then overlapped with a HeNe tracer beam via a pellicle; alignment is relatively trivial after this point.

2.2.4 Optical feedback

As opposed to the optical feedback from the cleaved ends of the semiconductor that is necessary for lasing, here optical feedback is due to laser light that is reflected back into the active area after the light is emitted from the diode. Diode lasers are very sensitive to optical feedback, and this has been used to great advantage in the near-infrared. For example, one facet of a near infrared diode is anti-reflection (AR) coated, and a diffraction grating is set up in a Littrow configuration such that the first order reflection is directed back to the diode.^{4,5} In this way, the laser cavity is defined by the uncoated facet of the semiconductor and the external grating. Moreover, the grating feedback is frequency selective, so that the diode lases in just one frequency mode. It is also possible to tune these diodes continuously by varying the temperature, current, and grating position.

There is no reason that such a configuration could not work for the Pb-salt diode lasers, and indeed, we have found that a portion of the diode beam can be fed back using a diffraction grating in a Littrow configuration; changing the length of this external cavity by small amounts enables one to change the frequency of the diode laser (the finesse of the diode laser cavity is quite low, *i.e.*, ≈ 3.7 , so it is possible to tune the laser by small amounts *within* one of the cavity modes). However, no Pb-salt diodes are commercially available with one facet AR coated, so the mode structure of the semiconductor cavity dominates the feedback, and the grating feedback cannot be used to continuously scan the laser. In addition, the grating would ideally be the first element the beam encounters after a collimating lens, creating an external cavity ≈ 1 cm in length. This would have to be performed in the laser dewar, which would require some modification. Leo Hollberg and Joseph S. Wells at the NIST laboratories are currently trying a grating feedback scheme for Pb-salt lasers, and it will be interesting to see their results.

In the meantime, however, optical feedback is at best a nuisance, and must be dealt with to perform accurate frequency measurements when scanning. The simplest way to do this is to ensure that a minimal amount of light is retroreflected to the laser. For example, lenses can be AR coated or tilted slightly away from the beam direction so that reflected light does not return to the laser. In order to combat optical feedback, a diagnostic is needed to tell when it is occurring. Fortunately, the diode laser can be rapidly scanned in frequency, providing a real-time diagnostic. To do this, simply input a sawtooth voltage ramp into the external modulation input of the current supply. Then view the etalon fringes from the confocal Fabry-Perot cavity on a detector. If the optical feedback is bad, the etalon fringes will look jagged, with staircase structure like that shown in Fig. 2.10a. This is an indication that an external element is providing a second cavity for the laser light, such that it has to satisfy two boundary conditions. As

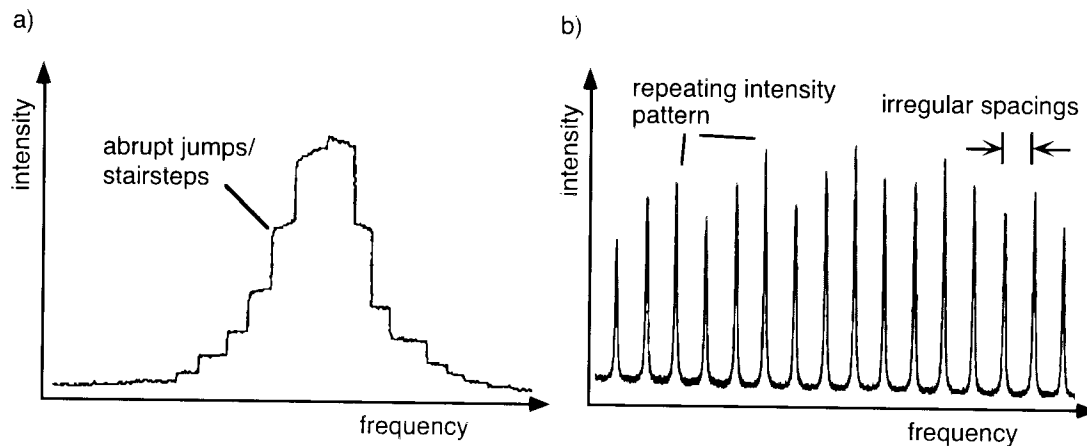


Fig. 2.10: Indications of optical feedback when scanning over etalon fringes. a) Detail of one fringe with staircase pattern, indicating strong feedback. b) Series of fringes exhibiting repeating intensity pattern and irregular spacings due to weak feedback.

the current is rapidly scanned, the diode tries to hold onto the frequency of the external cavity until the internal mode structure dominates; the laser then suddenly jumps to the next external cavity mode.

In more mild cases of feedback, the fringe pattern will look like that in Fig. 2.10b. The etalon fringes have irregular spacings, often repeating, and varying heights due to amplitude variations from etaloning (discussed below). Here the optical feedback is adding a sinusoidal component to the frequency tuning as the current is being scanned linearly. It is easy to determine which optical element or elements are responsible for the feedback. Lightly push on each element along the beam line until the staircase pattern, or sinusoidal pattern on the fringes is seen to move on the oscilloscope. The last element this happens for along the beam line is the offending element. Try realigning this element to reduce the effect. Another diagnostic is to simultaneously view the amplitude of the laser light on one detector and the etalon fringes on another as the diode is being rapidly scanned. Oftentimes the element feeding back to the laser acts like an etalon, and a sinusoidal varying of the light level is a clear indication of this. The free spectral range (fsr) of the external cavity can be

determined from this intensity variation, and the offending element can be found by measuring the cavity length corresponding to this fsr from the diode laser.

In the present studies, it is found that the feedback from the pinhole aperture (shown in Fig. 2.8) used to clean up the spatial profile of the beam is simply too great, no matter what material the pinhole is made from. This is because the pinhole is directly at the focal point of the first lens. Therefore, it is removed after aligning the laser beam, and an iris approximately 1 m from the diode is used to clean up the spatial profile. Also, the 6.2 μm homostructure diode is found to be far more sensitive to optical feedback than the 4.3 μm heterostructure diode. In order to reduce feedback for the H₂O studies to a manageable level, the two elements of the beam reducer shown in Fig. 2.8 were AR coated. The second lens in particular is a source of feedback, and even after it is AR coated, a Ge beam splitter is inserted at the focal point of the reducer at an angle of 45° with respect to the beam; the intensity of the retroreflected light is therefore cut by a factor of four, reducing the feedback to a manageable level.

2.2.5 Scanning the diode laser

In order to use the diode laser for spectroscopy, it is necessary to scan it. This is not as simple as dialing in some frequency on a black box and starting a scan. Instead, it is important to understand how the diode scans, what causes mode hops, why the diode can lase in multiple modes, and how to "pull" the different modes to gain (nearly) complete coverage of the spectrum.

As mentioned above, the semiconductor band gap increases with rising T . However, this is not what scans the laser in small steps. The diode can only lase in discrete cavity modes when $l = n\lambda/2\mu$, where l is the cavity length, n is an integer, λ is the wavelength, and μ is the index of refraction. For $\mu \approx 5$ and a cavity length of 250 μm , this corresponds to a comb of frequencies separated by 4 cm^{-1} . Since μ is both

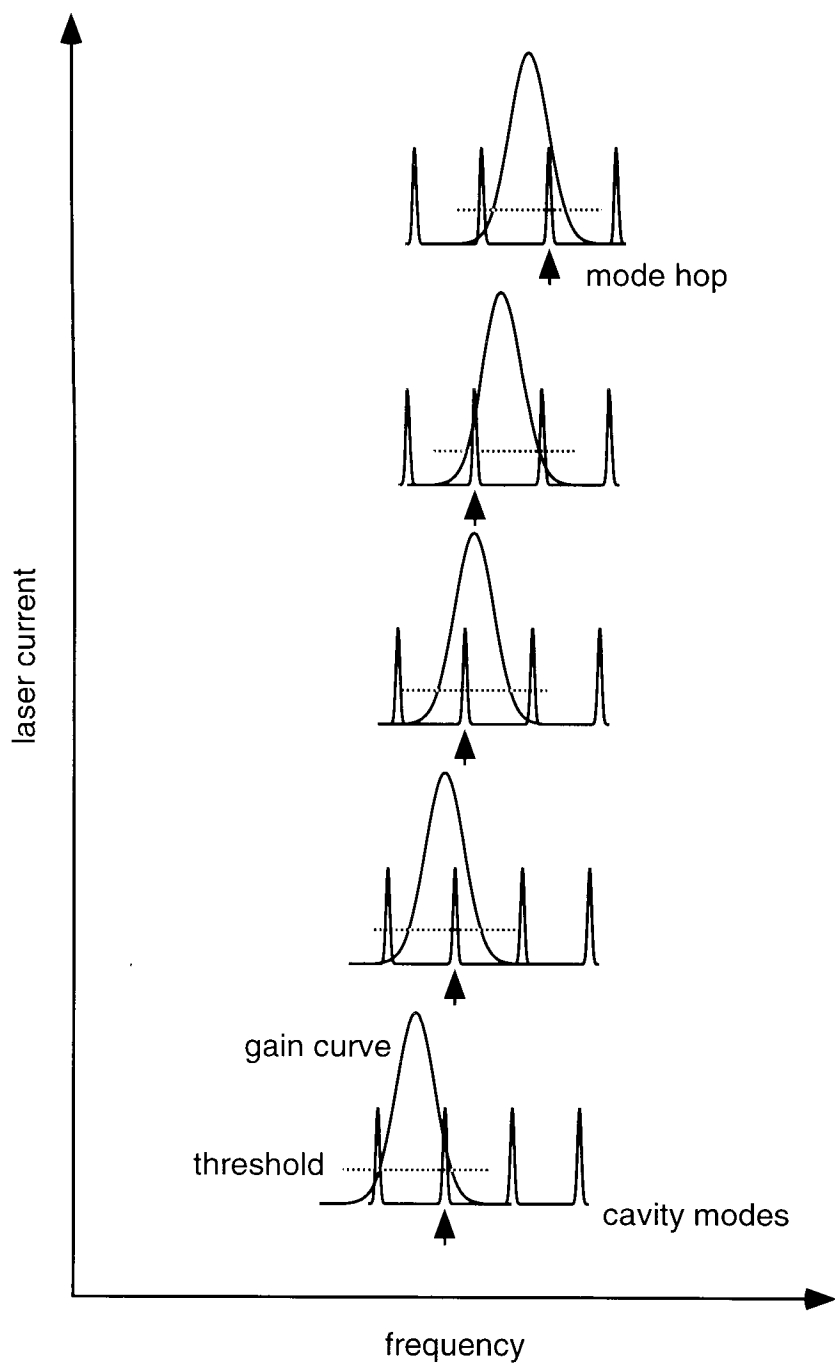


Fig. 2.11: Simple picture for a diode laser mode hop. Increasing the laser current heats the active area through local resistive heating. The band gap increases with T a factor of ≈ 3 greater than the shift in cavity modes, leading to mode hops.

temperature and current dependent, the cavity modes are shifted for a change in T or I ; for small changes in μ , the change in frequency is given by $\Delta\nu \approx -\nu_0(\Delta\mu/\mu_0)$. As seen in Fig. 2.11, if one of the cavity modes is coincident with the gain curve above some threshold value, then the diode can lase at this frequency. Small changes in T due to the resistive heating from the changing laser current, or the change in current density, can move the cavity modes through the gain curve in a continuous fashion, enabling one to scan the diode laser.

The laser cannot be scanned in one cavity mode forever, since the gain curve shifts with temperature about a factor of three faster than the cavity modes.¹ Therefore, as the laser current is increased (which also increases the temperature in the active region) the gain curve moves through the different cavity modes as shown in Fig. 2.11. Continuous scanning is observed for some frequency interval, then the laser hops to the next cavity mode at a higher frequency. This picture is oversimplified, however, since the gain curve not only shifts with temperature, but also increases in magnitude as the current is increased and the density of electron/hole pairs grows in the active region. Therefore, the scenario in Fig. 2.12 is closer to actual diode behavior. At currents just above threshold, typically the gain curve can support lasing in only one cavity mode. As the current is increased, this mode is scanned, but the increasing magnitude of the gain curve mean that additional cavity modes can support lasing above some current. The diode becomes multimode, first in one other mode, then in several modes.

This picture is consistent with observed diode behavior. For example, single mode lasing is observed for both lasers used in the present experiment at threshold conditions. Typically the power is low for threshold, about $1 \mu\text{W}$ on the signal detector for the heterostructure diode. As the laser current is increased, laser power is observed to steadily rise as the gain curve both moves through the cavity mode and increases in magnitude. Typically a mode hop is observed after the current is scanned

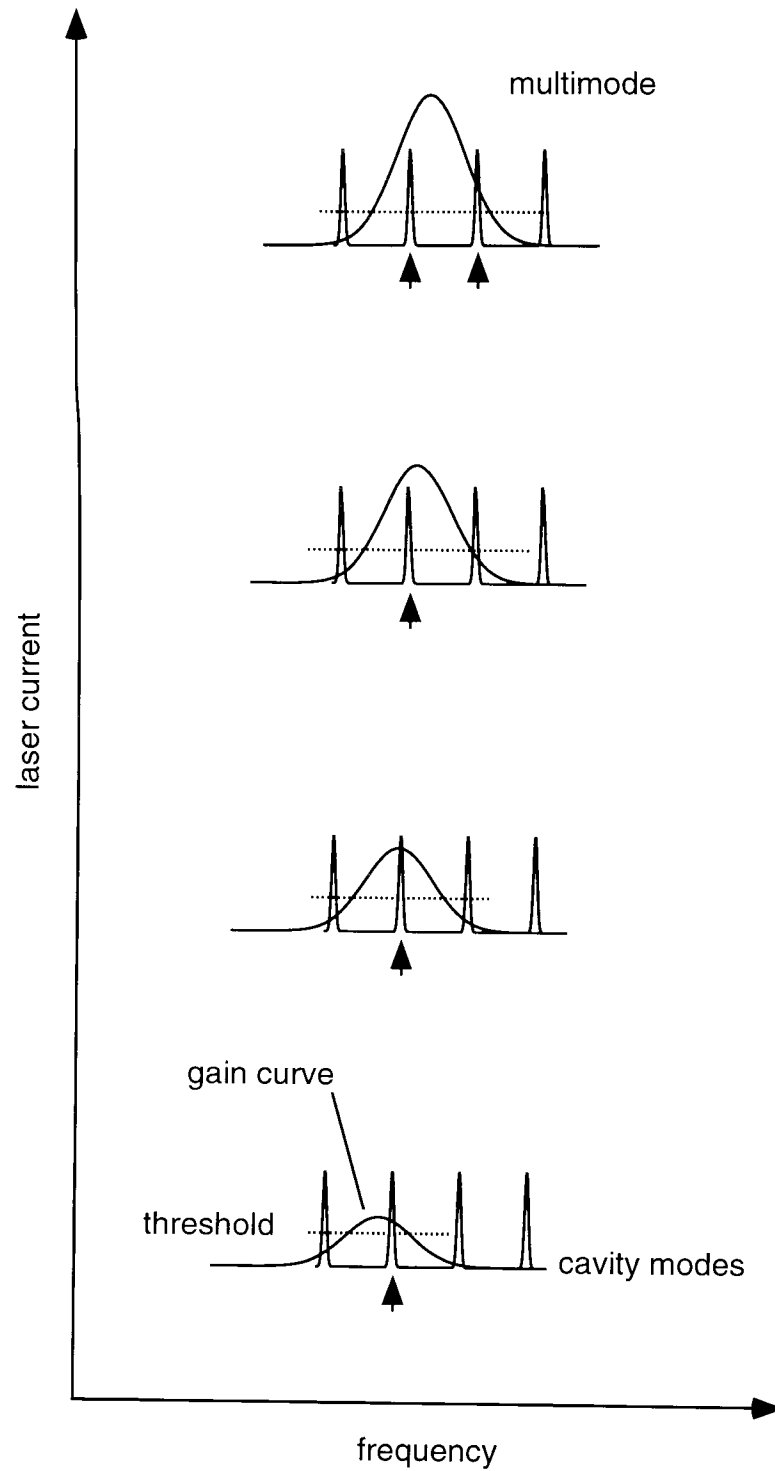


Fig. 2.12: Simple picture for diode laser multimode behavior. At threshold, the gain curve can support lasing in just one cavity mode. As the current is increased, the gain curve not only shifts due to resistive heating in the active area, but also grows in magnitude. At high enough currents, lasing in multiple modes can thus be supported.

over 10 to 20 mA, with the laser jumping anywhere from 3 to 7 cm^{-1} to the next mode. Several additional mode hops might be observed at even higher laser currents, and the laser becomes multimode. For these higher currents, laser powers of 10 to 20 μW are observed on the signal detector.

To gain maximum coverage of frequency space, it is necessary to "pull" different modes of the diode as a function of temperature. From Fig. 2.11, it can be seen that one cavity mode can be scanned continuously until a mode hop occurs. At higher currents, a new cavity mode is scanned; it begins with a mode hop and ends with a mode hop. It is possible to shift at what frequency these mode hops occur for a particular cavity mode by varying the temperature and current; this is referred to as "pulling" a mode. An example of this behavior is shown for the homostructure diode in Fig. 2.13. At higher temperatures and lower currents, the cavity mode supports

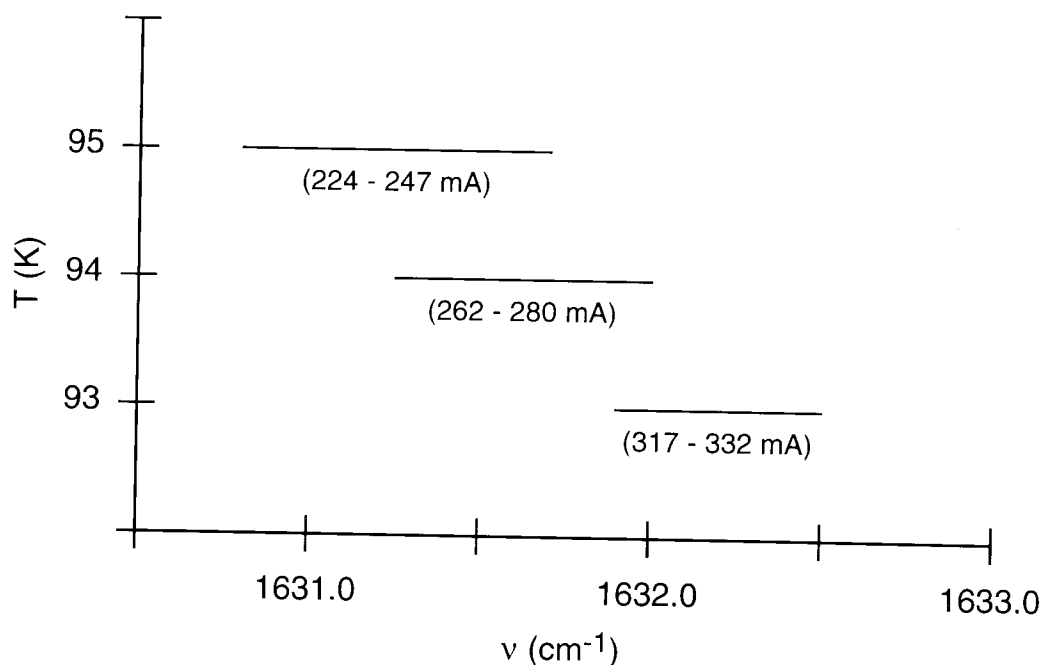


Fig. 2.13: Example of pulling a diode mode with temperature. This is for the 6.2 μm homostructure diode. The current range to scan the mode is shown in parenthesis. Each line represents the same cavity mode that is scanned from a mode hop at the start until a mode hop at the end.

lasing at lower frequencies. As can be seen, the converse is true as well; the cavity mode can be pulled to the blue by decreasing the temperature and increasing the current. This is due to the change in index of refraction of the active area with changing *current*. Even though the resistive heating in the active area due to higher currents would result in the same relative position of the cavity modes with respect to the gain curve as the same effective temperature at a lower current, the cavity modes are shifted by an additional amount due to the difference in current alone.

Normally additional modes appear at higher currents. As long as the majority of the power is in the primary mode, this is generally not a problem. However, secondary modes are usually 3 to 4 cm^{-1} to the red of the primary mode, and strong spectral features that are shifted by this amount from the region of interest can show up as ghost peaks. To test whether a peak is a ghost peak, scan the same region for a slightly different combination of temperature and current; the ghost peaks should shift relative to the primary transitions.

To map out the mode structure of a diode, rapidly scan the diode using a sawtooth wave, and view both etalon fringes and reference gas absorptions on an oscilloscope. For a constant temperature, the center current of the sawtooth ramp can be varied, and it is possible to see the mode structure in real time. Mode hops show up as discontinuities or irregularities in the etalon peaks, or even jumps in power. Multiple modes show up as additional peaks in the etalon trace. By sitting at the start of a mode and changing the temperature, it is possible to watch a particular mode move to the blue or red. The various temperature/current combinations that place the diode at the start of a mode can be recorded for starting subsequent scans. The diode is scanned by starting at these initial settings, then using a 13 bit D/A controlled by the computer to send discrete voltage steps to the diode current supply, which are then converted into current steps.

It should be noted that the heterostructure diode exhibits mode hysteresis. That is, if one starts the diode at a higher current and reduces the current, the mode hop to the next lower cavity mode occurs at a current that is *lower* than that for the mode hop when starting the diode out in the same lower frequency mode and increasing the current. Therefore, there exist several temperature/current combinations where the diode can lase in one of two possible modes, depending on whether the mode was scanned from above or below this current. This enhances the coverage obtainable with the heterostructure diode when combined with the mode pulling techniques. Complete coverage of over 20 cm^{-1} has been observed by piecing these modes together. The homostructure diode, however, does not exhibit mode hysteresis, and there are frequency gaps that cannot be reached. The coverage is still good, though, with $\approx 90\%$ coverage obtained from 1580 to 1640 cm^{-1} . It is possible to slightly alter the homostructure diode's mode structure by temperature cycling, *i.e.*, warming the diode to room temperature and cooling it back down again. This shifts the modes a few tenths of a wave number to the blue. Presumably this is due to small changes in the p-n junction due to additional diffusion of the impurities upon temperature cycling, although this has not been checked for other homostructure diodes in this study. The heterostructure diode in the present study, however, does not exhibit this behavior, presumably because the p-n junction is relatively stable to diffusion of impurities since it is formed via MBE.

2.2.6 Diode laser dewar

The diode laser dewar consists of two separate dewars: the first is a 1.5 liter capacity dewar with the lasers mounted on the underside of the liquid N_2 reservoir, in vacuum. The second is a 11.5 liter auxiliary dewar mounted on top that keeps the smaller dewar completely full. The combined hold time of the two dewars is > 5 days,

but for normal day to day use, the liquid N₂ level should not be allowed to drop below the auxiliary dewar. If it does, the upper portion of the lower dewar warms up, leading to thermal expansion of the dewar reservoir. Since the diodes are mounted on the bottom of the lower dewar, this changes the position of the diode with respect to the collimating optics, causing misalignment.

When the dewar is warmed up to room temperature, it should be pumped on with a liquid N₂ trapped roughing pump. Over a span of months, condensable gases such as H₂O or CO₂ accumulate in the dewar. As this occurs, blackbody radiation can warm the dewar more efficiently, and the ultimate base temperature of 79 K rises by 5 to 10 K. Although no significant pressure rises are observed in the dewar over a time span of months, when these condensable gases evaporate the pressure can rise dramatically. Also, as the dewar is warmed, it is important to heat the outside windows about 10°C warmer than room temperature so that a mysterious white film does not condense out on the windows. This can happen if cold vapor from the boiling liquid N₂ cascades down the outside of the dewar and cools the windows significantly below room temperature. Since this problem has become less severe over time, the white film is most likely due to something used in the manufacturing process of the dewar materials that is slowly outgassing and being pumped away by increments as the dewar temperature is cycled and it is pumped out.

2.3 Detectors

The detectors used to observe the infrared laser light are based on semiconductors, just like the diode laser. The simplest detectors use only a piece of intrinsic semiconductor, and are called photoconductive (PC) detectors. As in Fig. 2.2a, when photons with $h\nu > E_{\text{gap}}$ are incident on the detector, they excite electrons

from the valence band into the conduction band, which increases the conductivity of the semiconductor. This change of conductivity is measured to determine the light level on the detector. The other detectors used in the present experiment are photovoltaic (PV) detectors. These are based on the p-n diode junction in Fig. 2.3. Photons with $h\nu > E_{\text{gap}}$ incident on a PV detector excite an electron into the conduction band and a hole in the valence band in the depletion region of the p-n junction. The bias voltage due to the p-n junction then whisks the electron/hole pair out of the depletion region, creating a photocurrent that is proportional to the number of photons on the detector. Since the quantum yield, *i.e.*, the number of electron-hole pairs created for each photon, is $> 95\%$ for some infrared detectors, this provides an extremely sensitive way to detect infrared radiation, with background noise levels that are close to shot noise limited.

Both the signal and reference detectors used for the $4.3 \mu\text{m}$ CO_2 experiments are InSb PV detectors. These detectors were purchased from Cincinnati Electronics (model SDD-7854-S1), and are "matched," *i.e.*, the detector elements are from the same wafer, so that the frequency response of the semiconductor is the same, and the amplification circuits are identical. The detector elements are circular and 1.0 mm in diameter. Each element is mounted behind a 30° field of view (FOV) cold shield in thermal contact with a liquid N_2 reservoir. The window on the dewar is CaF_2 . The amplifiers are custom built by the manufacturer, and have a feedback resistor of $93 \text{ k}\Omega$. InSb PV detector elements must be cooled to liquid N_2 temperatures to form the depletion region of the p-n junction. When this happens, the resistance across the detector element is very large, and a static discharge across the element will damage the semiconductor itself. Therefore, these detectors should never be connected or disconnected when they are cold. When warm, the thermal energy of the majority carriers in the impurity region is enough so that the depletion region cannot form; the

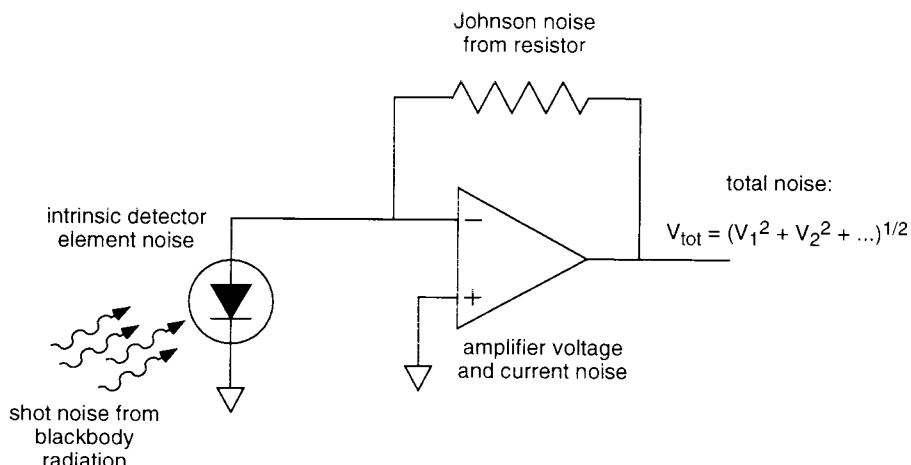


Fig. 2.14: Major noise sources for the InSb detector and preamplifier.

conductivity across the junction is thus high, and the element is not as likely to be damaged by a static discharge.

The InSb detectors are exceptionally sensitive, but to use this sensitivity to its full advantage it is important to understand the noise limitations of these devices. The detector consists of the InSb PV element attached to a transimpedance amplifier, shown schematically in Fig. 2.14. The transimpedance amplifier converts the photocurrent I from the element into a voltage given by $V = -IR$, where R is the resistance used in the transimpedance amplifier. There are fluctuations in this voltage, however, due to noise from different parts of the circuit. The four main noise contributions include

- 1) thermal Johnson noise from the resistor, which goes as $V_{\text{rms noise}}/\sqrt{\text{Hz}} = (4kTR)^{1/2}$. For a $93 \text{ k}\Omega$ resistor at room temperature, this gives a noise level of $39 \text{ nV}_{\text{rms}}/\sqrt{\text{Hz}}$.
- 2) The amplifier has both current and voltage noise at the input. The stated specs for the InSb preamps are $V_{\text{noise}} = 7 \text{ nV}_{\text{rms}}/\sqrt{\text{Hz}}$ and $I_{\text{noise}} = 1.5 \times 10^{-15} \text{ A}_{\text{rms}}/\sqrt{\text{Hz}}$. (The current noise leads to a negligible contribution across the $93 \text{ k}\Omega$ resistor.)
- 3) Intrinsic noise from the detector element itself, due to effects such as dark current, can add to the noise. This number is not provided by the manufacturer, but it is something we can estimate from a noise measurement.
- 4) Finally, since the InSb detectors are sensitive

to light with wavelengths out to $5.5 \mu\text{m}$, blackbody radiation incident on the element will lead to a photocurrent that has shot noise on it. Reducing this shot noise can lead to the biggest benefits in noise reduction.

To calculate the shot noise from background radiation, first it is necessary to determine the number of photons incident on the detector element. The spectral flux density, *i.e.*, the power incident on an area due to blackbody radiation at some T , is given by

$$S(\lambda) = \frac{2\pi hc^2}{\lambda^5} \left(\frac{1}{e^{hc/\lambda kT} - 1} \right). \quad (2.1)$$

The units of flux density are W/m^3 , which means that Eq. (2.1) must be integrated over some wavelength region to obtain the power incident on an area. Dividing this by the energy of a photon at a given wavelength, we obtain

$$\frac{\# \text{ photons}}{\text{sec} \cdot \text{m}^3} = \frac{2\pi c}{\lambda^4} \left(\frac{1}{e^{hc/\lambda kT} - 1} \right). \quad (2.2)$$

Since the bulk of the blackbody photons at room temperature are at wavelengths longer than $3 \mu\text{m}$, and since the InSb elements are sensitive to photons out to $5.5 \mu\text{m}$ with a quantum efficiency from 80% to $> 95\%$ over the 3 to $5.5 \mu\text{m}$ range, Eq. (2.2) is integrated over this spectral region to obtain a photon flux of 2.5×10^{16} photons/(sec cm^2). These photons are due to an unrestricted 2π steradian view of room temperature blackbody radiation above the detector element. The number of incident photons can be greatly reduced by restricting the FOV using a 77 K cold shield. The InSb detectors have a 30° FOV cold shield, which reduces the room temperature photon flux by a factor of 0.034. With this reduction and a detector element size of 1.0 mm in diameter, the photon flux on the detector element is 6.7×10^{12} photons/sec. Because of the high quantum efficiency, it is assumed that each of these photons creates an electron-hole pair, which leads to a photocurrent of $1.1 \mu\text{A}$. Finally, the shot noise due to this current is given by $I_{\text{rms noise}}/\sqrt{\text{Hz}} = (2qI_{\text{dc}})^{1/2}$, where q is the electron charge and I_{dc} is

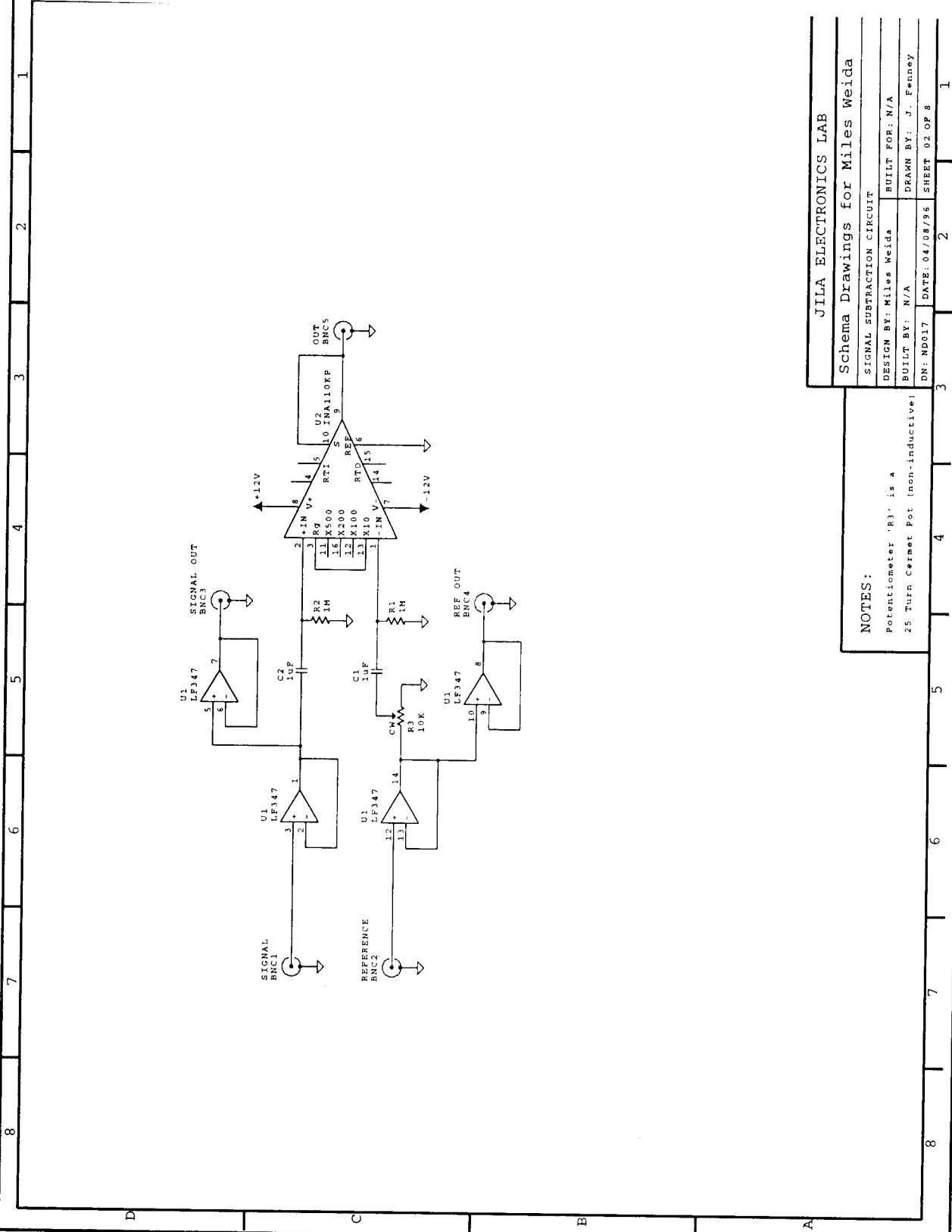


Fig. 2.15: Signal subtraction circuit.

| | |
|---------------------------------|---------------------|
| JILA ELECTRONICS LAB | |
| Schema Drawings for Miles Weida | |
| SIGNAL SUBTRACTION CIRCUIT | |
| DESIGN BY: Miles Weida | BUILT FOR: N/A |
| BUILT BY: N/A | DRAWN BY: J. Fenney |
| DN: ND017 | DATE: 04/08/96 |
| SHEET 02 OF 8 | |

NOTES:
 Potentiometer 'R3' is a
 25 Turn Cermet Pot (non-inductive)

| | | | | | | | |
|---|---|---|---|---|---|---|---|
| 1 | 2 | 3 | 4 | 5 | 6 | 7 | 8 |
|---|---|---|---|---|---|---|---|

the dc photocurrent. Thus $I_{\text{rms noise}} = 5.86 \times 10^{-13} \text{ A}_{\text{rms}}/\sqrt{\text{Hz}}$, which leads to a voltage noise across the resistor of $54 \text{ nV}_{\text{rms}}/\sqrt{\text{Hz}}$.

These main noise contributions are summed in quadrature to obtain a background noise level of $67 \text{ nV}_{\text{rms}}/\sqrt{\text{Hz}}$ for the InSb detectors. This is the rock bottom noise floor for these conditions; the measured noise will most likely be higher, especially since the intrinsic noise due to the InSb element is not included in this sum. It is possible to compare the actual noise level with this limit. First, a signal subtraction scheme is employed, such that the output from the signal and reference detectors is fed to the high common mode amplifier in Fig. 2.15. By subtracting the reference and signal detector output, amplitude noise on the diode laser light from low frequency technical contributions, such as liquid N₂ boiling off in the diode laser dewar, can be reduced. However, by subtracting the output of the two InSb detectors, we actually increase the noise level due to the incoherent noise contributions of each detector as well. The rock bottom limit for the subtraction scheme will thus be $95 \text{ nV}_{\text{rms}}/\sqrt{\text{Hz}}$, *i.e.*, the above number summed in quadrature for the two detectors.

The noise spectral density is measured for the two InSb detectors with the full subtraction circuit with an FFT, and the results are presented in Fig. 2.16. (To compare these noise levels with the above calculations, the scale in Fig. 2.16 has been divided by 10 to account for the $\times 10$ gain of the subtraction circuit). As can be seen, the noise floor for the detectors with no laser light incident on them is $118 \text{ nV}_{\text{rms}}/\sqrt{\text{Hz}}$, with some small additional technical contributions at lower frequencies. This is within 25% of the estimated rock bottom, which demonstrates just how quiet these detectors are. If it is assumed that the discrepancy between these two numbers is due solely to the intrinsic noise from the detector element, then this yields an intrinsic detector element noise of $49 \text{ nV}_{\text{rms}}/\sqrt{\text{Hz}}$.

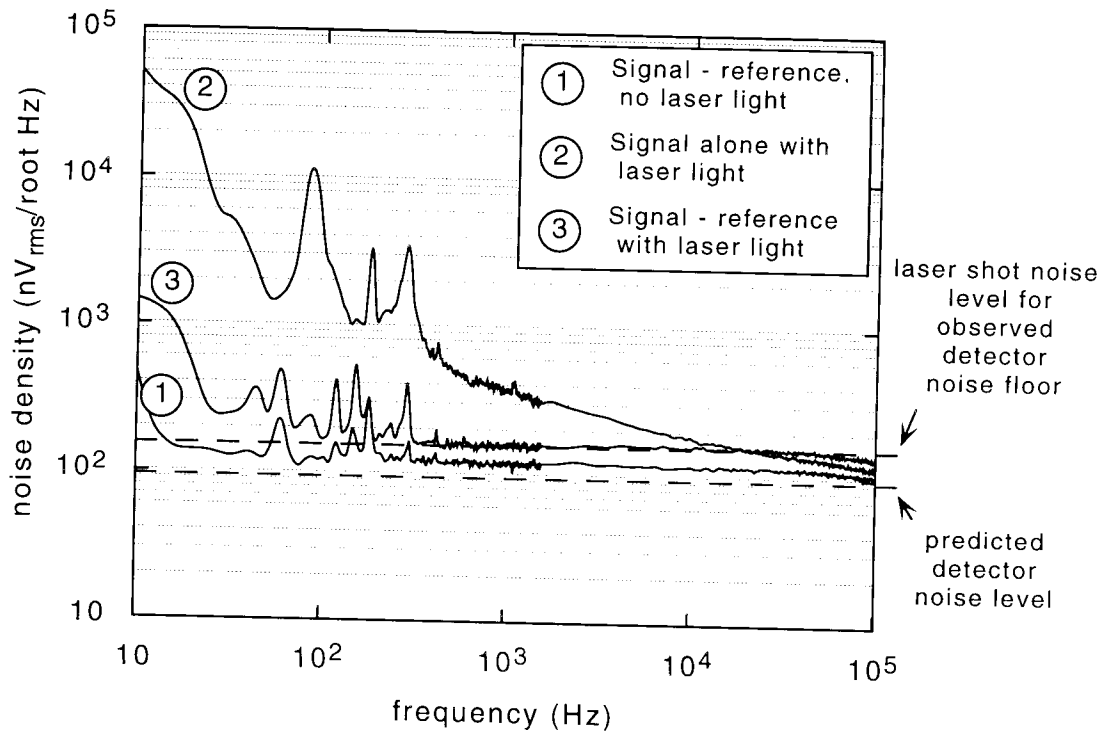


Fig. 2.16: Noise spectral density for InSb PV detectors.

Next, consider the noise spectral density with $0.5 \mu\text{W}$ of 2350 cm^{-1} diode laser light incident on one detector. As can be seen, the diode laser has very little amplitude noise, with the majority coming from low frequency technical contributions such as liquid N_2 boiling off in the diode laser dewar. This type of noise is easily reduced via the subtraction scheme, and as can be seen in Fig. 2.16, the noise level of the laser light is reduced to the shot noise limit with respect to the detector noise floor for frequencies greater than a few hundred Hz. The shot noise is calculated for $0.5 \mu\text{W}$ of 2350 cm^{-1} light incident on either detector, and is found to be $69 \text{ nV}_{\text{rms}}/\sqrt{\text{Hz}}$ for each detector. For lower frequencies, the noise specs are within a factor of 3 of the shot noise limit.

For frequencies $> 10^4 \text{ Hz}$, the noise spectral density begins to decrease. This is due to the finite bandwidth of the detectors. The bandwidth is limited due to the capacitance of the InSb p-n junction in combination with the preamplifier. The

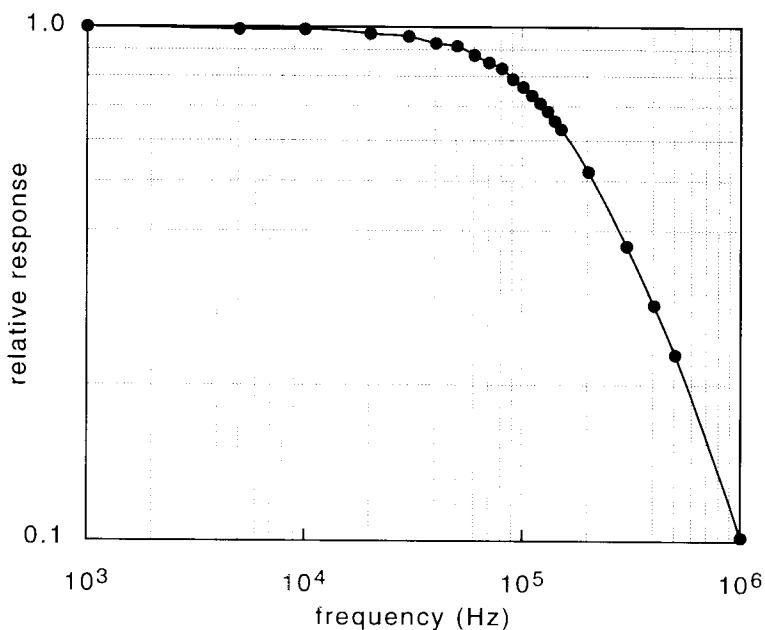


Fig. 2.17: Frequency response of InSb PV detectors

bandwidth can be measured directly by modulating the light of a visible LED with a sine wave voltage, and then observing how the measured peak-to-peak amplitude of the modulation decreases with increasing modulation frequency. To insure that this decrease is not due to the LED, first the amplitude as a function of modulation frequency is measured using a fast FND-100 Si photodiode. It is found that the amplitude modulation is independent of frequency out to > 200 kHz. The same measurement is then made with the InSb detectors, and the results shown in Fig. 2.17. As can be seen, the detector/preamp combination has a -3 dB point of 120 kHz. This is identical for both InSb detectors.

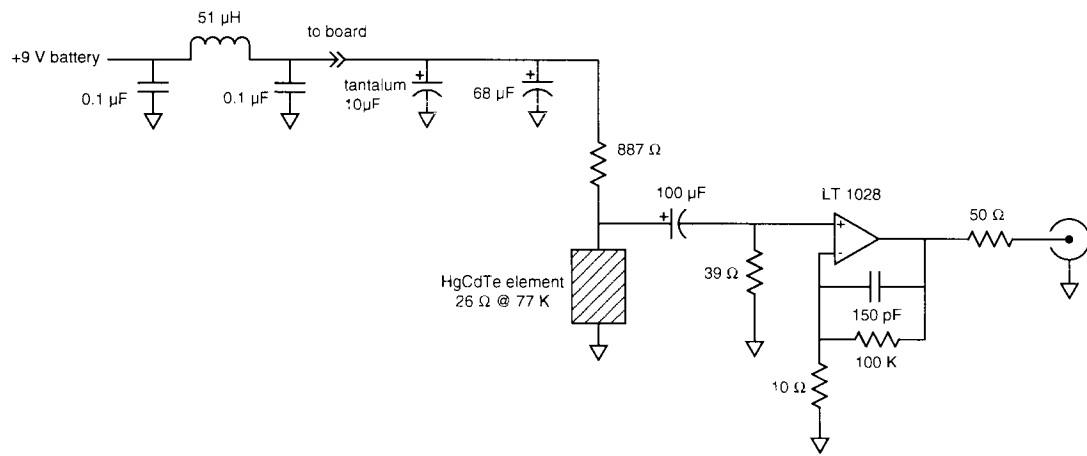
The signal and reference detectors for the $6.2 \mu\text{m}$ H₂O experiments are HgCdTe PC detectors; at 77 K, the InSb detectors are sensitive to light out to $5.5 \mu\text{m}$, while the HgCdTe detectors are sensitive out to $12.5 \mu\text{m}$. The HgCdTe detector elements are $1.0 \times 1.0 \text{ mm}^2$, and are mounted behind a 30° FOV cold shield in a liquid N₂ dewar with a CaF₂ window. These detectors were purchased from InfraRed Associates (now

Graseby Infrared), and came with a custom built preamplifier. This has since been replaced by the circuit in Fig. 2.18a (the original amplifiers are labeled and stored in B241 and can be replaced). The response of the detector/amplifier combination is approximately 1.9 V per μW of $4.3 \mu\text{m}$ radiation. The intrinsic sensitivity of the HgCdTe PC detectors is down by a factor of 5 from the InSb PV detectors. This is consistent with the observed factor of five sensitivity difference between the $4.3 \mu\text{m}$ and $6.2 \mu\text{m}$ experiments: for the CO_2 experiments the ultimate detection sensitivity is 1.0×10^{-4} absorbance per pulse in a 20 kHz bandwidth, while it is 5.0×10^{-4} for the H_2O experiment.

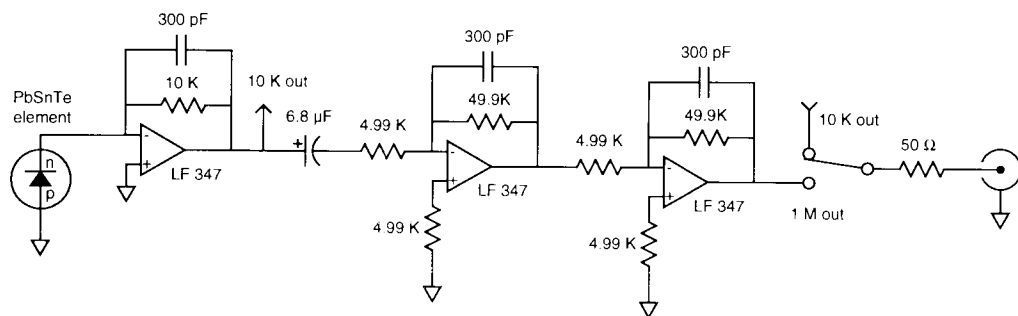
There are three different detectors that can be used for diagnostics, *i.e.*, recording the etalon and reference gas traces. One of these is a PbSnTe PV detector, which is sensitive to wavelengths out to $11 \mu\text{m}$ and can be used for either frequency region in the present experiments. The $1.0 \times 1.0 \text{ mm}^2$ element was taken from an old detector manufactured by Plessey Optoelectronics and Microwave (model LXC 1000S) and remounted behind a 30° FOV cold shield in a new liquid N_2 dewar with a CaF_2 window. The amplifier circuit is home made, and the schematic is in Fig. 2.18b. The background rms noise observed on this detector is a factor of ≈ 35 greater than expected from the background blackbody 300 K radiation shot noise. This is more than an order of magnitude greater than for the InSb detectors, whereas comparison of the relative semiconductor sensitivities would suggest that it should be a factor of 5 different. This extra noise might be due to damage of the detector element; its previous history is unknown. Nevertheless, this sensitivity is more than adequate for use as a diagnostic detector.

The second diagnostic detector is a PbSe PC detector. Since this is a Pb-salt semiconductor, cooling it to 77 K decreases the band gap such that its useful range is extended to $6.5 \mu\text{m}$. It can thus be used for both the H_2O and CO_2 experiments. The

a) HgCdTe detector circuit



b) PbSnTe detector circuit



c) PbSe detector circuit

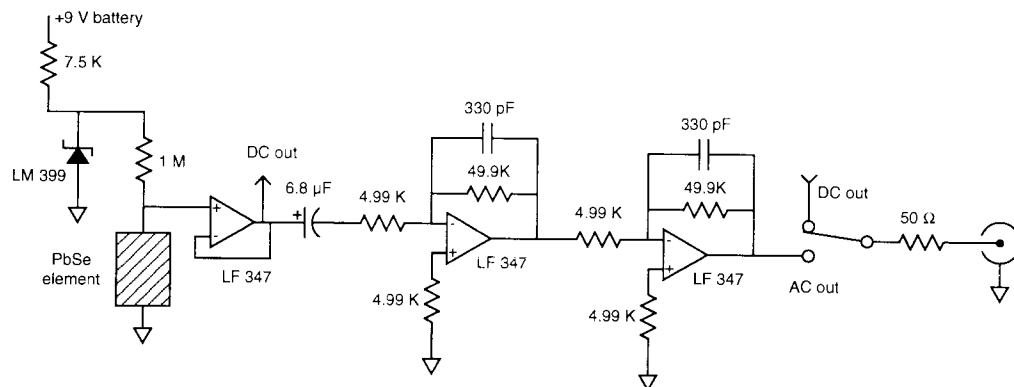


Fig. 2.18: HgCdTe PC, PbSnTe PV, and PbSe PC detector circuit diagrams.

1.0 x 1.0 mm² element is from Infrared Industries (5000 series) and is mounted behind a 30° FOV cold shield in a liquid N₂ dewar with a CaF₂ window. The original detector package was hermetically sealed with a sapphire window. Since sapphire does not transmit out to 6.2 μm, this window was removed on the lathe. The amplification circuit is home made and shown in Fig. 2.18c. This detector is more than adequate to record the reference gas trace; no attempt was made to characterize its noise.

The last detector used for diagnostics is an InSb PV detector. The element is circular with a diameter of 2.0 mm. It is mounted behind an AR coated Ge window cooled to 77 K in a liquid N₂ dewar with a sapphire window. Details of the construction of this detector and its amplifier are presented elsewhere.⁸ This detector is used in the 4.3 μm region.

2.4 Frequency measurement

In order to make accurate frequency measurements, absolute frequencies are determined from reference gas transitions, and the regular transmission fringes from a confocal Fabry-Perot cavity are used to interpolate between the reference gas transitions. The actual algorithm for assigning frequencies will be covered in the data collection and analysis section; particulars of the reference gas and marker cavity are presented here. For the CO₂ studies at 4.3 μm, CO₂ makes an excellent reference gas. A single pass through a 6 cm long, 0.1 torr CO₂ reference cell with sapphire windows provides reference peaks with anywhere from 5% to 90% absorption at intervals of ≤ 0.8 cm⁻¹. The frequencies of the CO₂ transitions have been conveniently tabulated⁹ in the 4.3 μm region.

To interpolate between these transitions, a 10.3 cm confocal Fabry-Perot cavity is used. A 2.54 cm diameter, 7.8 cm long quartz tube with a 2.54 cm diameter, 2.54 cm long piezo tube mounted on one end is used as a spacer for the mirrors. The

mirrors are 10.3 cm radius of curvature (r.o.c.) CaF₂ plano-convex lenses coated on the convex side to be 95% reflective at 4.3 μm . The mirrors are fortuitously reflective at 633 nm, so the cavity can be initially aligned with a HeNe laser by scanning the length of the piezo tube. Once this is done, the cavity can be aligned for the infrared beam by rapidly scanning the frequency of the diode and observing the etalon fringes on an oscilloscope. The fsr of this cavity is found to be ≈ 725 MHz by interpolation from reference gas absorptions. The finesse of the cavity is ≈ 17 as measured with the diode laser. This is reasonable given that the reflectivity limited finesse is 30, and that some additional broadening will be observed due to the diode laser frequency noise.

Although this cavity is not stabilized, the reproducibility of repeated frequency measurements is 12 MHz rms. This level of absolute accuracy and relative precision is obtained with a nonstabilized cavity for three reasons. First, the relatively small spacing between CO₂ reference peaks means that the time to scan between them is on the order of 10 to 20 minutes for the van der Waals complex studies. On this time scale the temperature of the cavity changes little. Second, all the CO₂ studies are carried out in a purge box which is slightly overpressured with N₂. The pressure in the cavity is thus buffered from changes in building pressure on a 10 to 20 minute time scale. Last of all, the majority of the CO₂ scans contain multiple reference gas transitions; the fsr can be recalculated for each scan, thus taking into account day to day changes due to overall differences in temperature and pressure.

For the H₂O studies, the accuracy and relative precision of the frequency measurements is improved by a factor of two by the use of an actively stabilized cavity. Although this is a desirable improvement in and of itself, it is also necessary for the 6.2 μm region given the density of reference peaks. The only frequency standard at present for the 1550 to 1650 cm⁻¹ region is H₂O or HOD.⁹ Since this is around the origin of the ν_2 bend of H₂O at 1595 cm⁻¹, relatively few strong transitions are populated at 300

K, and spacings between reference peaks can be as large as 3.5 cm^{-1} . Clearly it is not possible to include two reference peaks in every scan if the diode can only cover $< 1 \text{ cm}^{-1}$ between mode hops. Therefore, it is necessary to have a constant cavity fsr to use for frequency measurements.

There are two reference gas cells used in this frequency region. The first is 50 cm long with CaF_2 windows and contains 10 torr of H_2O vapor. The laser beam is passed twice through this cell, giving a total path length of 1 m; this is necessary to obtain $> 10\%$ absorption for most of the reference peaks. The second cell is 20 cm long with CaF_2 windows and contains 10 torr of a 2:1 mixture of $\text{H}_2\text{O}:\text{D}_2\text{O}$. Because of the proton exchange in water, this results in a 4.4 torr partial pressure of HOD. This cell is used for the HOD absorptions, and can be inserted or removed from the beam line to determine whether an absorption in the H_2O cell is due to HOD in natural isotopic abundance.

The actively stabilized confocal Fabry-Perot cavity has been described in detail elsewhere,^{10, 11} and a brief summary of its operation, plus a more detailed description of modifications for the present experiment, is presented here. The exceptional stability of this cavity is achieved by locking its length to a transmission fringe from a polarization stabilized HeNe laser.¹² The polarization stabilized HeNe provides 633 nm light that is stable to within 50 kHz on the time scale of an hour, and to within 5 MHz over a *year*.¹³

In order to lock the cavity length to the HeNe transmission fringe, the 30 cm cavity is constructed as shown in Fig. 2.19. An 8 cm long 2.54 cm diameter stainless steel tube is attached on both ends to 2.54 cm diameter Pyrex tubing via a glass to metal seal. A 17Ω heater tape is wound around the metal tube to provide slow variation of the cavity length via thermal expansion/contraction. A 2.54 cm long piezo tube (Channel Industries, material: C-5700, silver electrode, 2.54 cm outer diameter, 1.6

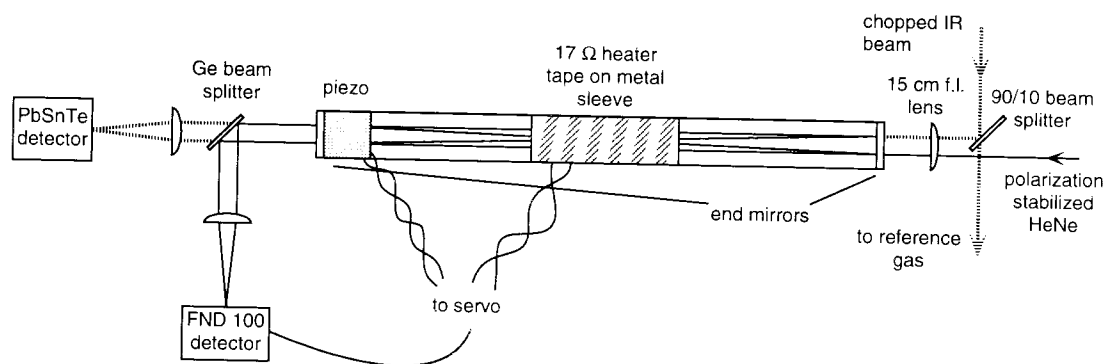


Fig. 2.19: Optical layout for actively stabilized confocal Fabry-Perot marker cavity. The end mirrors are coated for 92% reflectivity at both $6.2 \mu\text{m}$ and 633 nm .

mm wall) is mounted on one end to provide fast (1 kHz) variation of the cavity length. The end mirrors are 30 cm r.o.c. CaF_2 plano-convex lenses coated on the convex side to be 92% reflective at both 633 nm and $6.2 \mu\text{m}$.

The cavity is aligned by first mounting one end mirror to the piezo tube using cellulose nitrate adhesive (can be removed with acetone), then attaching the other end mirror to a suitable translation stage such that it can be translated and rotated with respect to the Pyrex tube/first mirror for fine adjustments. The cavity is then aligned using the HeNe laser by ramping the piezo to view transmission fringes. Once the second end mirror is in the appropriate position, it is attached to the Pyrex tube using the same adhesive. The measured finesse for the HeNe is 14, within 30% of the reflectivity limited finesse of 19.

To actively lock the cavity length to a HeNe transmission fringe, the servo loop circuit in Figs. 2.20 and 2.21 is used. This circuit is similar to previous versions,¹¹ but several simplifying modifications have been made in the design, and it is included for completeness. First, a bias current is sent to the heater tape to heat the tube to approximately 10°C above ambient temperature. The tube can thus be heated or cooled by changing the heater current. Next, the piezo is dithered with a 4.4 kHz , $V_{pp} \approx$

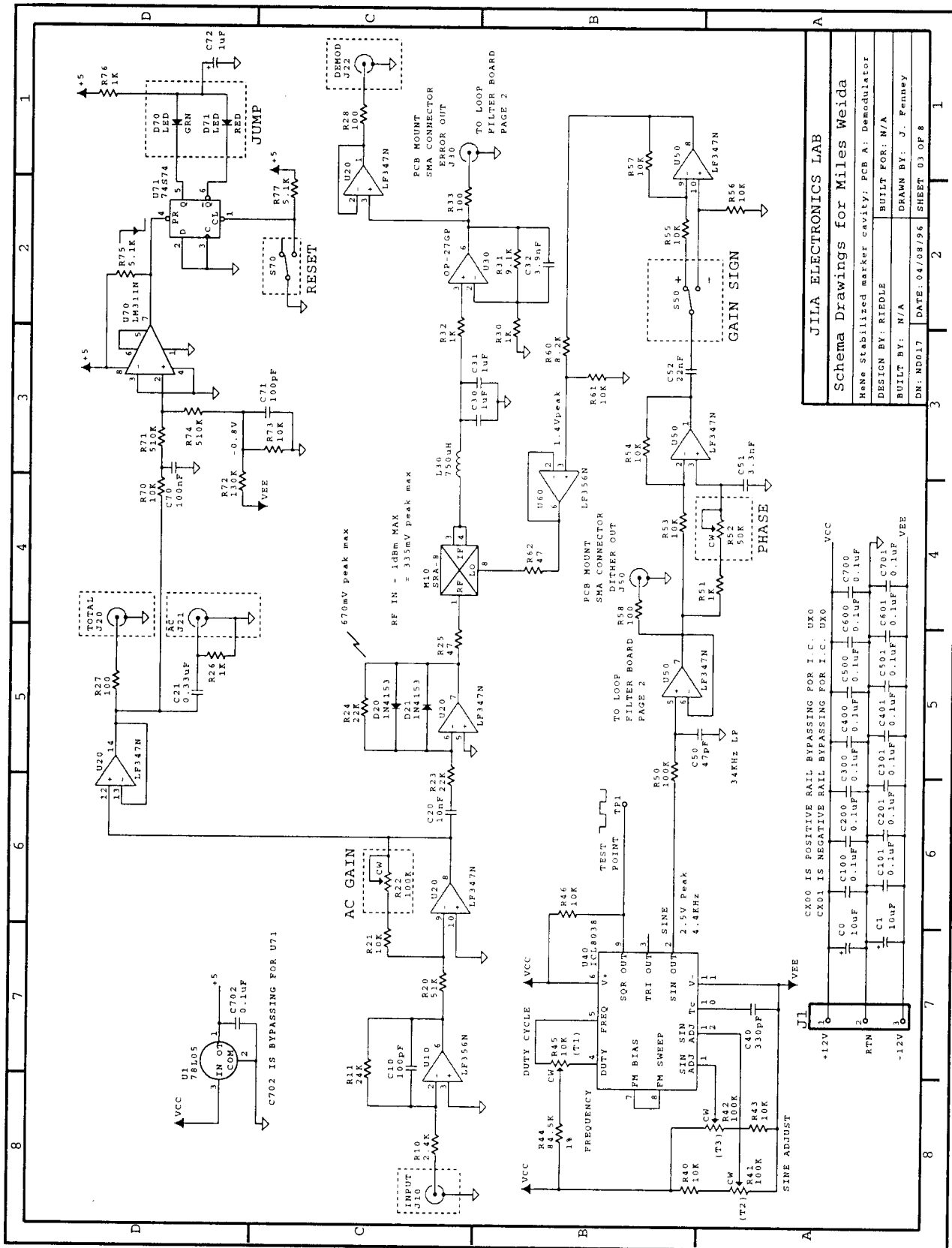


Fig. 2.20: Circuit diagram for actively stabilized Fabry-Perot marker cavity (page 1 of 2).

0.125 V sine wave. This scans the cavity by < 1 MHz, and places a small amplitude modulation on the HeNe transmission fringe. The transmitted HeNe is collected on an FND 100 silicon photodetector, and this signal is heterodyned and demodulated with the 4.4 kHz reference oscillation to obtain a first derivative of the HeNe transmission fringe. Since the first derivative goes to zero at the peak of the fringe, the servo can lock to this point. Fast, proportional corrections to the cavity length are handled mainly by the piezo, while slow, integral corrections are handled by the heater.

To simultaneously align the HeNe beam and the infrared laser beam through the cavity, the arrangement in Fig. 2.19 is used. Because the infrared light available for diagnostics is limited to $< 25\%$ of the total power of the diode, it must be chopped and detected via lock-in techniques to obtain adequate reference gas and etalon fringe signals. Therefore, the chopped infrared beam and unchopped HeNe are brought into the cavity via the two different sides of the "bow-tie" mode. The HeNe beam is then separated from the infrared via a Ge beam splitter after the cavity.

Once the feedback loop is closed, the servo quickly locks onto a HeNe transmission fringe; the various gains in the loop have been preset, and as long as the alignment of the cavity is fine, there is nothing to do but switch the servo on after the tube has been given a couple of hours to warm up to a stable temperature. The entire cavity is placed inside a plexiglass enclosure with holes for the beam to enter and exit. This is to reduce the effects of air currents on the cavity. With this arrangement, the cavity has stayed locked onto the same fringe for over two weeks. This is ascertained by the intensity of the HeNe light on the detector; if it falls below some setpoint, the cavity has moved off of the fringe, and a warning light comes on in the servo.

The fsr of the cavity is determined by "splitting the fringe." The fsr is first determined to 3 digits by counting the number of fringes between two reference peaks separated by $\approx 1 \text{ cm}^{-1}$ in the same scan; linear interpolation is used to determine the

fractional fringe spacings near the reference peaks. Since the cavity is stabilized, the absolute position of the fringes does not shift with time, so it is possible to use this fsr to estimate the relative position of a fringe with respect to a reference peak that is then 2 cm^{-1} away. The actual fringe position is then measured and found to be within one tenth of a fringe spacing from the predicted position. This identifies the number of integral fringes, and with this information, a refined fsr can be calculated, which can be used in turn to estimate a fringe position even farther away. This process is repeated until the fsr is calculated for a 19 cm^{-1} span. It is found to be $8.33775 \times 10^{-3}\text{ cm}^{-1}$, and accurate to 5 significant digits. This is a fsr of 250.132 MHz, as expected for a $\approx 30\text{ cm}$ cavity.

The absolute stability of the cavity is measured over a time span of 3 days by determining the fringe frequency with respect to a reference gas absorption in the slit jet for multiple measurements. The rms deviation in fringe frequency is 7.5 MHz. This is almost identical to the 8 MHz rms uncertainty in frequency measurements of ArH_2O transitions from repeated scans. This is remarkably stable over three days, but is a factor of 5 larger than the stability achieved in the difference frequency lab.¹¹ There are several reasons why this might be the case. First, the fringes in the present experiment are from the infrared laser, while the difference frequency fringes are for the visible laser. There are many atmospheric absorptions due to H_2O at $6.2\ \mu\text{m}$, and these might affect the length of the cavity in the infrared by changing the index of refraction near an absorption. To mitigate this effect, the apparatus is purged with dry N_2 . Second of all, the infrared and HeNe laser beams are not brought into the cavity collinearly. This and the poor spatial mode quality of the infrared beam might lead to small variations in infrared beam path length through the cavity as the laser is scanned. This in turn would appear as drifts with respect to the HeNe transmission fringe. A shift of 8 MHz could

occur for a change in path length of only $5 \mu\text{m}$, which is equivalent to a 0.6 mrad angular beam displacement.

2.5 Optics layout

The complete optical path, as shown schematically in Fig. 2.1, is enclosed in a 460 liter dry N_2 purge box. Due to significant atmospheric concentrations of CO_2 and H_2O , it is not possible to run the experiment without reducing the atmospheric concentrations of these gases by at least a factor of 20. This usually takes ≈ 1500 liters of dry N_2 , or one quarter of a full 1A cylinder. After this point, a small positive pressure of N_2 is maintained to keep the optics path purged.

Unless otherwise noted, the lens and windows are made of CaF_2 for its excellent (95%) transmission through the visible and out to $7 \mu\text{m}$. BaF_2 is used for the diode laser dewar windows; its properties are similar to CaF_2 . All mirrors are gold coated on a flat glass substrate, and are purchased from Edmund Scientific. The beam splitters range from a pellicle beam splitter to overlap the HeNe tracer beam with the infrared laser, several coated CaF_2 beam splitters, and Ge beam splitters; these are often interchanged for different experiments.

For the sublimation and van der Waals complex studies, the infrared beam is multipassed in the vacuum chamber using a 40 cm modified Herriott cell.¹⁴ A schematic of this is shown in Fig. 2.22 along with the slit pulsed valve on its translation stage. The optics consist of two Au coated 40 cm r.o.c. mirrors, 5.08 cm in diameter. It is relatively simple to align the multipass to get anywhere from 10 to 20 passes. The infrared beam (overlapped with the HeNe tracer so that it can be seen) is coupled into the multipass via a 50 cm focal length lens. This is placed so that the focal point is at the center of the multipass. The beam is brought in so that it is incident upon the upper corner of the opposite mirror, and subsequent reflections are directed so that

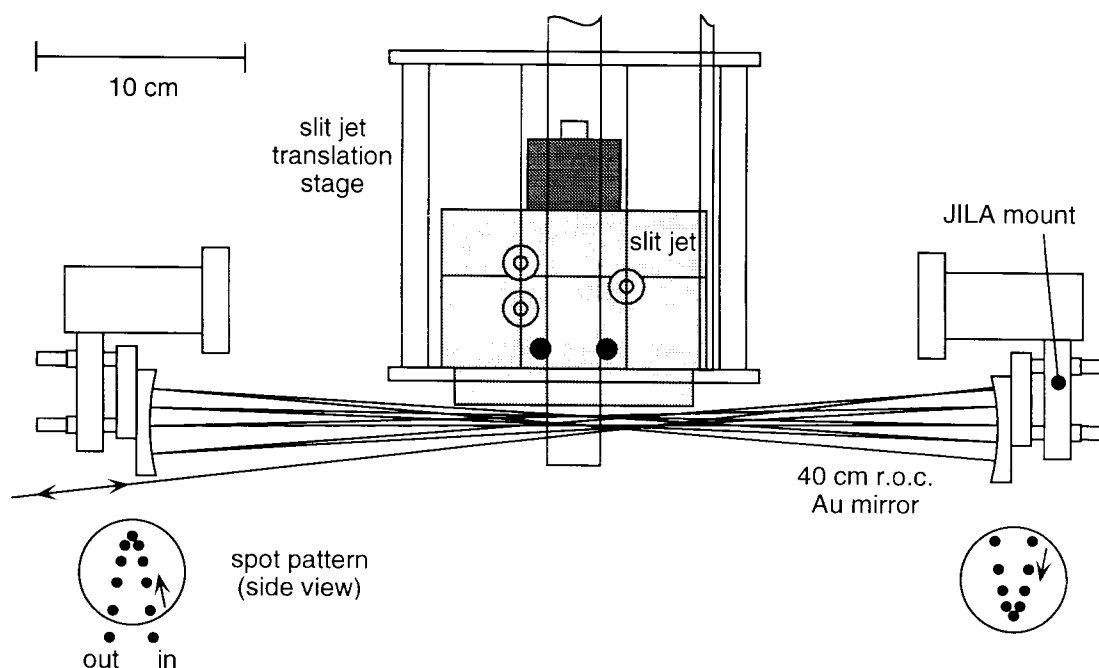


Fig. 2.22: Multipass layout with slit jet translation stage. The arrows for the spot pattern indicate the order of the spots in terms of reflections after the input beam.

they trace out the paraboloid spot pattern as shown in Fig. 2.22. The overall length of the multipass is adjusted so that the exiting beam is as tightly focused as possible. For fewer passes (*e.g.*, 10), this corresponds to a shorter distance (5 to 15 mm decrease from the 40 cm confocal separation) between the mirrors, and for more passes (*e.g.*, 20), this corresponds to a greater separation, approaching the confocal separation of 40 cm.

Once the laser is aligned through the multipass, the slit jet can be positioned relative to it via the translation stage. The slit is slowly lowered and moved side-to-side until the multipassed beam is along the guide slots of the slit. The slit is then raised ≈ 5 mm from where it begins to clip the multipass beam.

Due to the nonorthogonal intersection of the laser beam with the expansion axis, some line broadening is observed with the modified Herriott cell. For example, the

first pass of the laser has the steepest angle, *i.e.*, 7° , with respect to a beam orthogonal to the expansion axis. For a He expansion, this corresponds to a velocity component of 190 m/s along the laser beam. This in turn corresponds to a Doppler shift of 45 MHz for $(\text{CO}_2)_3$. Although this is for the greatest non-orthogonal angle in the multipass, the linewidths for $(\text{CO}_2)_3$ increase from 55 MHz FWHM for a single pass through a He expansion, to 75 MHz FWHM for 20 passes in the modified Herriott cell. This effect is not as great in an Ar expansion, however. For example, the Doppler width of ArH_2O is 11 MHz at an expansion temperature of 6 K. The linewidths measured for 18 passes through the modified Herriott cell are 22 MHz FWHM.

As an aside for the alignment measurements, the modified Herriott cell rotates the polarization of the laser light by $6.8^\circ \pm 2.0^\circ$. This appears to be independent of the number of passes, since the same rotation is observed for 10 or 18 passes. The cell does not significantly change the polarization from linear to elliptical ; the extinction coefficient of 10^{-3} for a second crossed linear polarizer (taking into account the 6.8° rotation) does not change after passing through the cell.

2.6 Vacuum system

The vacuum system consists of an 80 liter aluminum and plexiglass cube for a chamber, evacuated by a liquid N_2 trapped 1000 liter/s 6" oil diffusion pump. The diffusion pump is backed by a 23 liter/s Welch roughing pump (model 1398). The roughing pump is vibrationally isolated from the vacuum chamber via a brass bellows attached to a rigid frame, and rests on large rubber stoppers for vibration isolation from the floor. A gate valve is positioned between the chamber and the liquid N_2 trap. Pressures are measured on an ionization gauge or thermocouple gauge. The base pressure of the system is 1.0×10^{-6} torr. The diffusion pump is used for the sublimation and alignment studies, while just the liquid N_2 trapped roughing pump is

used for the van der Waals complex studies. The roughing pump alone is adequate for these studies; for example, at a slit jet repetition rate of 16 Hz for an Ar expansion at $P_0 = 300$ torr, the pressure in the chamber is 75 mTorr. The mach disk for these conditions occurs ≈ 9 cm from the slit. For faster expansion gases such as He or H₂, background pressures as high as 2 torr (as measured on the thermocouple gauge) are possible without a noticeable decrease in cluster signal, or increase in expansion temperature.

2.7 Gas handling

A variety of gases have to be mixed and delivered to the experiment at either the correct pressure or flow rate. This is accomplished using the gas handling system shown in Fig. 2.23. It is constructed of both copper and stainless steel tubing, and the valves are all stainless steel. Connections are made with either Swagelock or VCR fittings. The system can be evacuated with a liquid N₂ trapped mechanical pump.

Gas mixtures are made in a 1A cylinder via a tee inserted on the high pressure side of the regulator. For the CO₂ studies, the mixing tank is first taken through several purge/pump cycles to ensure that residual contaminants are below a part in 10⁵. Then it is filled with CO₂, typically between 50 and 100 torr; pressures are measured using a 100 torr capacitance manometer (MKS Baratron type 222CA). Finally, the carrier gas is mixed with the CO₂; typically 100 to 200 psi is mixed with the CO₂ as rapidly as possible to ensure turbulent mixing. Gas mixtures made by this process can be used within an hour, *i.e.*, no significant variations in signal due to incompletely mixed gas over the time span of a day are observed. The pressure in the mixing tank can be read using the gauges on the regulator. For the H₂O studies, the mixing tank is replaced with an Ar cylinder and the bubbler is used to introduce H₂O vapor into the carrier gas. The bubbler is filled with distilled H₂O and is kept at 0°C by immersing it

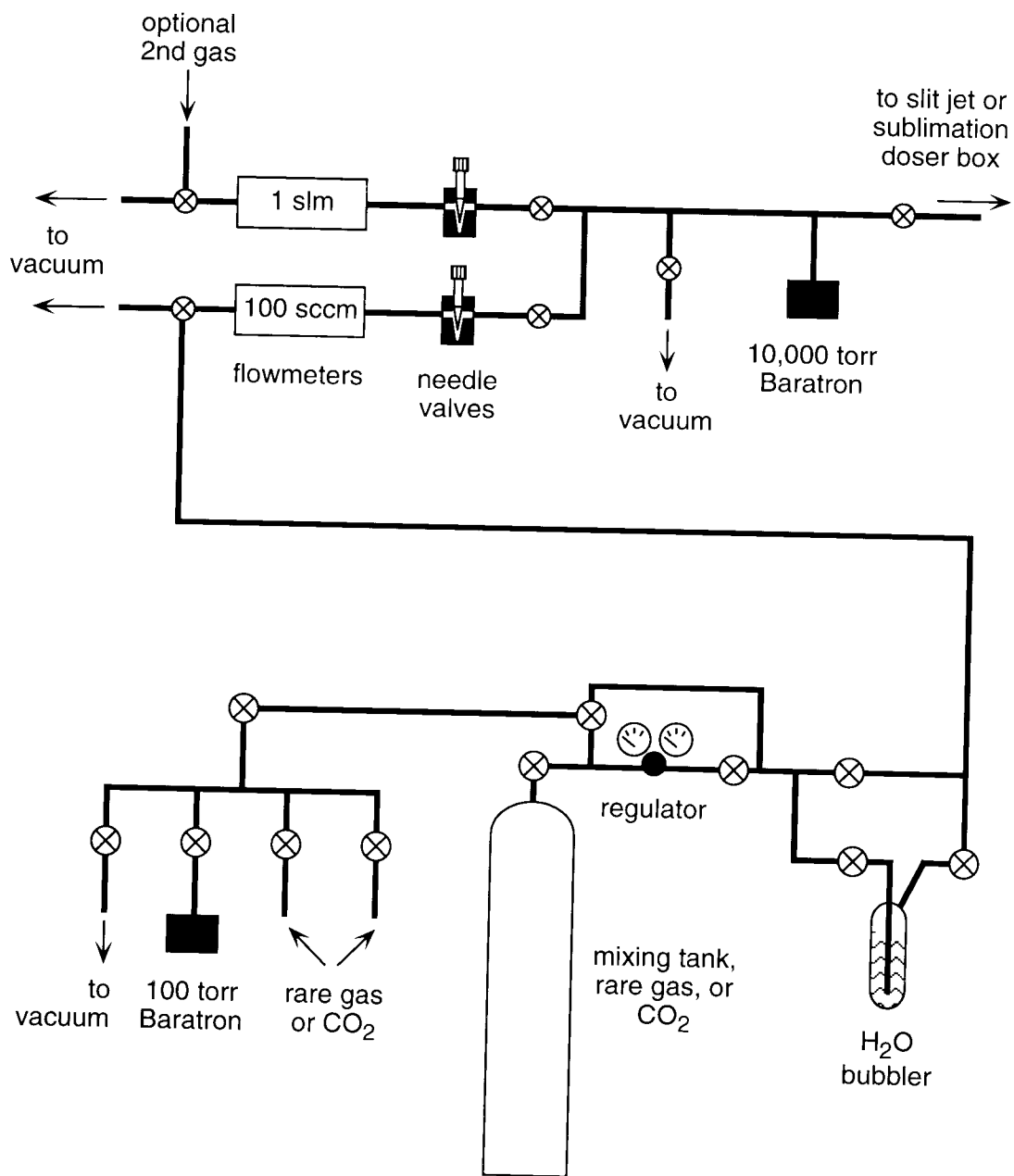


Fig. 2.23: Schematic of gas handling system for slit jet or sublimation doser box.

in an ice bath. The vapor pressure of H_2O at this temperature is ≈ 5 torr, so the relative concentration of water vapor entrained in the carrier gas can be controlled by varying the pressure of the carrier gas through the bubbler. For the studies employing a pulsed supersonic expansion, the gas mixture is throttled down to the appropriate pressure using a needle valve. Stagnation pressures for the expansion are measured with a 10,000 torr capacitance manometer.

To grow the thin films for the sublimation studies, it necessary to deliver CO_2 to the doser box at a precise flow rate. The mixing tank is replaced with a CO_2 cylinder, and this gas is passed through a flowmeter (Tylan, model FM380), and then throttled with a needle valve to regulate the flow. The flow rate can be set before sending gas to the doser box by opening the gas handling system to vacuum right after the needle valve; the needle valve can then be adjusted to give the proper flow rate. The flowmeters must be calibrated for each gas mixture used. This is done by measuring the pressure rise vs. time in a known volume for a certain flow rate. The flowmeter readout can thus be related to the actual flow.

2.8 Supersonic expansion

The workhorse for the majority of the experiments performed in this thesis is the supersonic expansion. Pinhole and slit expansions are commonly used in chemical physics studies for their ability to form weakly bound complexes at rotational temperatures of $\lesssim 20$ K, and to form molecular beams with relatively narrow hyperthermal velocity distributions that can be used to study collision dynamics. Both the theory and operation of supersonic expansions has been considered in detail elsewhere.^{15, 16} In the present section, a brief overview of both the principles behind the expansion, and the construction and operation of the slit and pinhole pulsed valves is presented. Lastly, the formation of $(\text{CO}_2)_n$ clusters is considered.

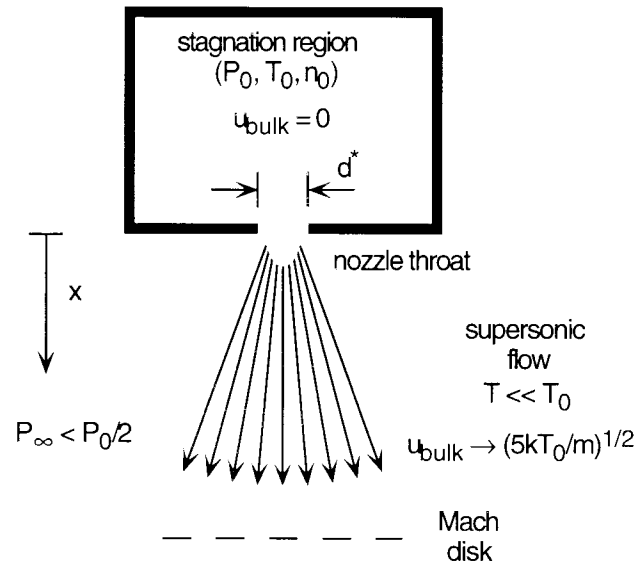


Fig. 2.24: Schematic of a supersonic expansion.

2.8.1 Overview of theory and operation

As shown in Fig. 2.24, if a gas at some stagnation temperature T_0 and pressure P_0 is expanded through an orifice with width d^* into a lower pressure (P_∞) region, then a supersonic expansion can be formed. The requirements for this to occur are *i*) that the mean free path of the gas molecules in the nozzle is $\ll d^*$, and *ii*) that $P_0/P_\infty \gtrsim 2$. The first requirement insures that heat transfer between the walls of the orifice and the expanding gas is negligible, while the second requirement insures that there is some region over which the expanding gas can be considered without the effect of collisions from background gas molecules. If these conditions are met, then the expansion is adiabatic and isentropic, and the temperature of the expanding gas is related to the local density and pressure, *i.e.*,

$$\frac{T}{T_0} = \left(\frac{P}{P_0} \right)^{\frac{\gamma-1}{\gamma}} = \left(\frac{n}{n_0} \right)^{\gamma-1}. \quad (2.3)$$

Here, $\gamma = C_p/C_v$ is the ratio of the heat capacities at constant pressure and volume, and is $5/3$ for a monatomic gas. The temperature of the gas thus drops as it expands to

lower pressures. In addition, the bulk velocity u of the gas increases such that it becomes greater than the local speed of sound, $\bar{a} = \sqrt{\gamma RT/m}$, where R is the universal gas constant, and m is the mass; hence the name supersonic expansion. As the expansion develops, it approaches its terminal velocity¹⁵ $u_{\text{bulk}} \rightarrow \sqrt{5kT_0/m}$ for a monatomic gas. A rigorous fluid dynamics analysis of the expansion can be performed^{15, 16} to demonstrate that ultimate temperatures as low as a few degrees K are reached.

Although the macroscopic thermodynamics properties of the expansion are important to understand the cooling process, it is the *microscopic* dynamics that are of interest for processes such as cluster formation and the creation of rotational alignment. In addition to cooling, three-body collisions are needed to form van der Waals complexes. Hence, the slit expansion geometry is preferable over the pinhole for making clusters, since the density drop is slower for a line than a point source. This leads to more binary and three-body collisions. For the creation of rotationally aligned molecules, however, the driving force is the initial "velocity slip" between the heavier CO₂ molecules and the lighter carrier gas atoms. The velocity slip decreases with increasing number of binary collisions, and thus fewer binary collisions are required to create and preserve aligned molecules. Hence the pinhole geometry is preferable to the slit to create aligned molecules. Additional aspects of the microscopic dynamics will come into play when considering how nonequilibrium populations can be "frozen out" in the expansion; this will be central to the discussion of cluster formation dynamics in Chapter 8, and will be covered in detail there.

One aspect of the supersonic expansion that is relevant to an experimental section is the Mach disk. This is a shock wave where the expanding gas begins to come into equilibrium with the background gas in the vacuum chamber. It is referred to as the Mach disk because it is the point at which the bulk velocity of the expanding gas

drops below the local speed of sound. An *empirical* relation¹⁷ for the downstream distance x of the Mach disk for a slit with width d^* is given by

$$x = 1.23d^* \left(\frac{P_0}{P_\infty} \right)^{0.775} . \quad (2.4)$$

This relation can be used to estimate what background pressures can be tolerated for a given stagnation pressure before the expansion is disrupted in the laser probe region.

For the van der Waals complex studies, a pulsed slit expansion is used. In addition to the higher degree of clustering obtainable in a slit, the expansion geometry also leads to significantly narrower linewidths than in a pinhole expansion. The velocity distribution parallel to the slit is predominately due to thermal motion of the gas, since the slit dimensions (4 cm x 120 μm) approximate an infinite line over a majority of the slit, *i.e.*, edge effects are small. The resulting linewidths can be Doppler limited, and widths as narrow as 22 MHz FWHM are observed in the ArH₂O studies. In contrast, linewidths in unskimmed pinhole expansions are predominately due to projections of the beam velocity on the laser probe, and widths on the order of 100 MHz are observed in the pinhole alignment studies. Lastly, the expansion is pulsed to reduce the gas load on the vacuum system, and to create a transient absorption signal for more sensitive detection.

The pulsed slit valve shown in Fig. 2.25 is used for the van der Waals cluster studies; details of its construction and operation are presented elsewhere.^{16, 18} Briefly, the valve is constructed in the JILA shops from 300 series stainless steel, while the lifting rod is made of 17-4 ph stainless steel. The seal assembly consists of a piece of Viton o-ring attached with cyanoacrylate adhesive to a titanium holder (the poppet). The poppet is fastened to the lifting rod by first screwing the lifting rod into the poppet, then holding this in place by pressing a nickel slug against the lifting rod threads via a set screw on either side of the poppet. A second set screw is then used to lock the first

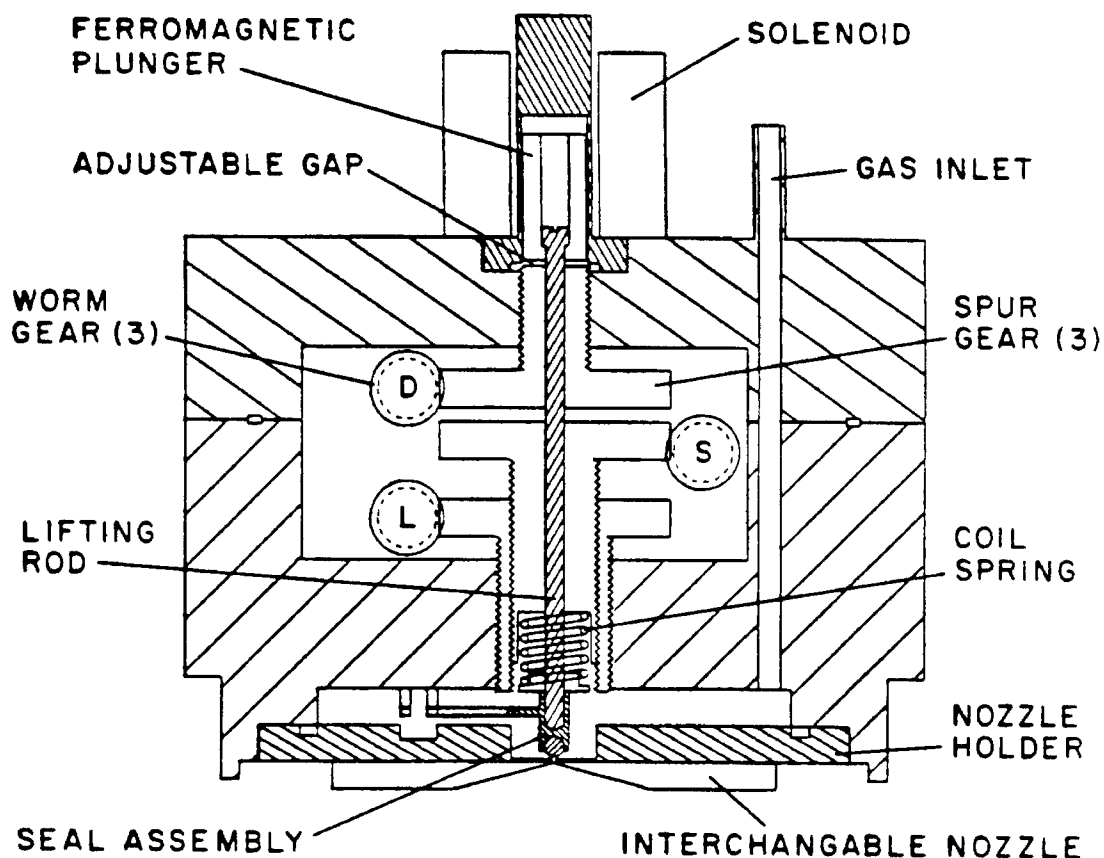


Fig. 2.25: Cut-away view of pulsed slit valve (from ref. ¹⁶).

in place. The valve is opened by accelerating the magnetic plunger (type 440 magnetic stainless steel) against the lifting rod with a current pulse through the solenoid (rated at 1.8 V dc, 0.6 Ω resistance, 370 μ H inductance). The current pulse is supplied by the SCR based circuit in Fig. 2.26, and has a peak of 70 A with a FWHM of 440 μ s. The pulse driver is capable of driving the valve at repetition rates of up to 25 Hz.

A sample CO₂ monomer transient absorption signal from the slit valve is shown in Fig. 2.27. The valve typically takes $\sim 50 \mu$ s to open, and $\sim 100 \mu$ s to close. The flat middle section of the pulse corresponds to the valve being fully opened. To adjust the slit valve, either a monomer or cluster absorption is used along with the following procedure. 1) Evacuate the vacuum chamber and supply ~ 1 atmosphere of gas

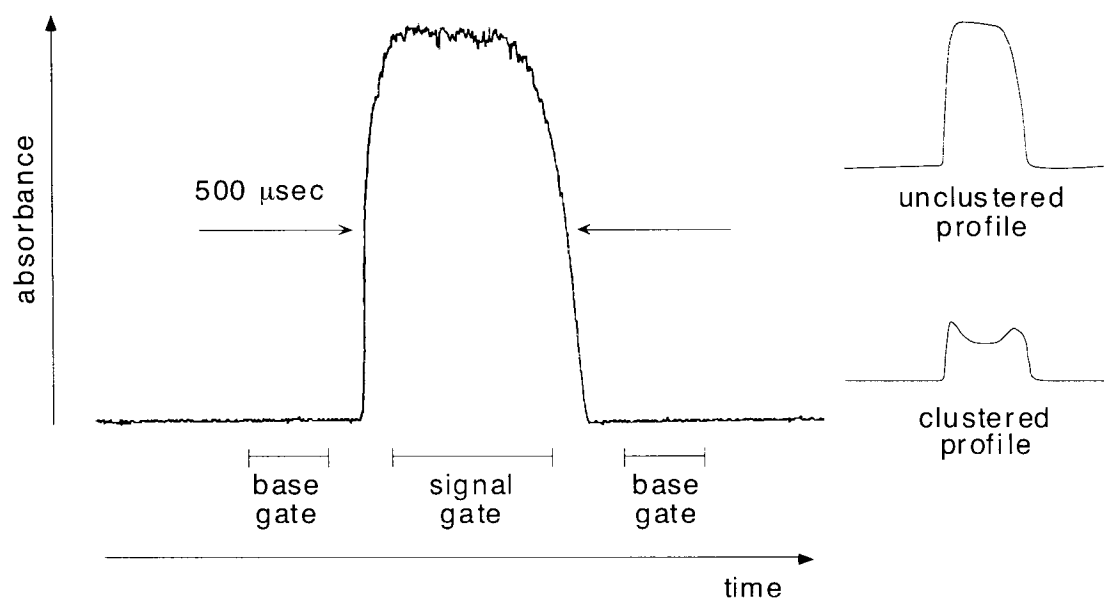


Fig. 2.27: Sample absorption pulse from pulsed slit valve. ($P(4)$ of CO_2 , conditions: 0.05% CO_2 in He at $P_0 = 450$ torr.)

mixture to the slit jet. Decrease the spring tension (counter clockwise (c.c.w.) on knob 'S' in Fig. 2.25) until a pressure rise is observed in the chamber. Then increase the spring compression just to the point where the leak stops. 2) Begin pulsing the valve by providing 285 V across the solenoid as shown on the gauge of the pulse driver. Use the appropriate stagnation pressure to observe the absorption signal of interest. 3) While observing the absorption pulse on an oscilloscope, adjust the plunger travel ('D' in Fig. 2.25, c.w. = more) until the leading edge of the pulse is $\sim 700 \mu\text{s}$ after the trigger. 4) Adjust the poppet travel ('L' in Fig. 2.25, c.w. = more) until the trailing edge of the pulse is $\sim 500 \mu\text{s}$ after the leading edge. 5) The trailing edge of the pulse can then be improved by increasing the spring compression and varying the poppet travel. Increasing the spring compression also reduces "ringing," *i.e.*, secondary bounces of the seal assembly. 6) For the final pulse, make sure the valve is fully open by verifying that increasing the pulse length does not increase the absorption.

Once the valve is adjusted, small corrections must be made on a day to day basis, since the pounding of the plunger against the lifting rod slowly changes the plunger travel distance. After a few months of operation, the trailing edge of the pulse will often degrade to the point where adjustments can not bring it back to its original state. It is then time to replace the Viton seal. Another problem experienced with the valve was due to bent lifting rods. In this mode of failure, the *leading* edge of the pulse changed on nearly a pulse to pulse basis, sometimes by as much as 400 μ s. This problem was solved by replacing the lifting rod.

The transient absorption pulse can also be monitored for evidence of extreme clustering. This is apparent as a dip in absorption in the center of the pulse, as shown in Fig. 2.27. This is due to clustering of the monomer signal, or even secondary clustering if a dimer or trimer signal is being monitored. Because the leading and trailing edges of the pulse correspond to the valve being partially open, the expansion is slightly warmer at these times. Hence, the degree of clustering is less than when the valve is fully open, and clustering or secondary clustering depletes the signal more in the center of the pulse than at the warmer edges. If a cluster signal is being optimized, the stagnation pressure is decreased until the pulse resembles the unclustered profile.

In addition to the pulsed slit jet, a pulsed pinhole expansion is used for the alignment studies. The valve is solenoid activated (General Valve, Series 9, 28 V DC) with a 150 μ m pinhole aperture. Either Teflon or KEL-F poppets (available from General Valve) are used. The Teflon poppets only last for a few days of operation before the pulse shape degrades, however, so the sturdier KEL-F poppets are used for most of the measurements. The driver for the pulsed valve is a home-made supply borrowed from the crossed beam experiment in lab B214. Adjusting the pinhole valves is quite simple. After replacing the magnetic slug/spring/poppet assembly, lightly screw the pinhole cap onto the valve body. Pressurize the valve with N₂, and place a

small amount of leak tracer over the pinhole. Tighten the pinhole cap just until the N_2 stops leaking through the pinhole. The pulse length can then be adjusted by lengthening the current pulse and monitoring a monomer absorption. The pinhole valve takes $\sim 200 \mu s$ to open or close, so total pulse lengths are typically $800 \mu s$.

2.8.2 $(CO_2)_n$ cluster formation

At this point it is interesting to consider the actual formation of $(CO_2)_n$ clusters in the slit expansion. The simplest picture for this process is based on three-body collisions. If two particles collide elastically in the expansion, the total energy of the combined system exceeds the van der Waals binding energy, and the particles do not stick together. A *third* particle can carry off some of this energy during a collision, however, leaving the first two particles without enough energy to separate, *i.e.*, they have formed a complex. Lovejoy¹⁶ has estimated the number of three-body collisions a particle experiences in a slit supersonic expansion for a variety of "typical" expansion conditions for different carrier gases: $P_0 = 400$ torr for Ar, $P_0 = 1500$ torr for Ne, and $P_0 = 2000$ torr for He. In each instance, somewhere between 10% to 50% of the particles in the expansion are estimated to undergo a three body collision for these conditions. If every one of these three-body collisions results in a complex, then a zeroeth order guess for the fraction of monomer ending up in clusters would be somewhere between 10% and 50%.

For expansions of CO_2 in a He carrier gas, however, most of the three-body collisions will probably not end up forming a complex due to the difficulty in forming He - CO_2 complexes, as will be covered in Chapter 4. This is in contrast to Ar expansions, where significant clustering is observed even at backing pressures as low as 100 torr. If it is assumed that only three-body collisions containing at least two CO_2 molecules will form complexes, then it is possible to estimate the fraction of monomer

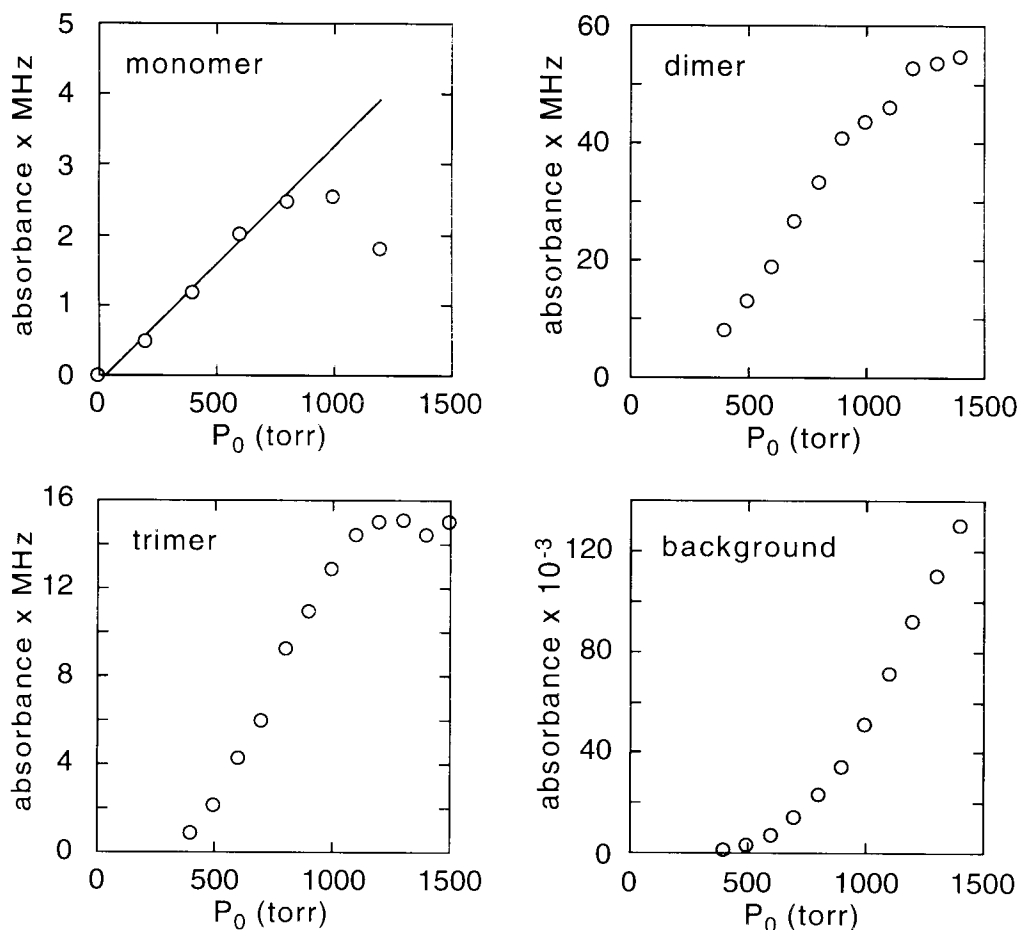


Fig. 2.28: Curves of growth for $R(1)$ of monomer ($^{17}O^{12}C^{16}O$), a -type Q -branch of $(CO_2)_2$, rQ_0 of $(CO_2)_3$, and background at 2353.26 cm^{-1} . The ordinate is the integrated absorbance of the transition, except for the background, where just the absorbance is reported. (Conditions: 2% CO_2 in He).

lost to clustering for 2% CO_2 expanded in He for "typical" expansion conditions; only one in fifty of the three-body collisions a CO_2 molecule experiences will involve a second CO_2 . If one factors in the fraction of molecules experiencing three-body collisions, less than 1% of the monomer will be lost to $(CO_2)_n$ clusters at typical expansion conditions for three-body cluster formation.

This can be rigorously tested via curves of growth and the absolute infrared cross sections of the absorbing species. Shown in Fig. 2.28 are the curves of growth

for $^{17}\text{O}^{12}\text{C}^{16}\text{O}$ monomer, $(\text{CO}_2)_2$, cyclic $(\text{CO}_2)_3$, and a broad background absorption that has been attributed¹⁹ to $(\text{CO}_2)_n$ clusters where $n \sim 10^2$. Basically, the integrated absorbance of one transition or Q -branch is monitored as a function of stagnation pressure. If no monomer is lost to clusters, then the monomer curve of growth should increase linearly with stagnation pressure, since the density of absorbing gas is also increasing linearly. As can be seen in Fig. 2.28, though, the monomer signal deviates from the linear trend for $P_0 \gtrsim 750$ torr. If the linear portion of the curve of growth is extrapolated to higher pressures, it is simple to estimate the fraction of monomer clustered at higher pressures; it is $> 50\%$ at $P_0 = 1200$ torr. Clearly this exceeds the estimate of 1% clustering based on three-body collisions alone.

To reconcile this difference, it is necessary to follow where the clustered CO_2 is going. As mentioned above, very little is going into HeCO_2 clusters for a room temperature stagnation gas, so it must be going to $(\text{CO}_2)_n$ clusters. The curves of growth demonstrate this quite well. At increasing pressures where the monomer begins to cluster, first the dimer, the trimer, then the larger clusters grow in. This sequential growth with stagnation pressure is partly consistent with the three-body collision model. After all, a dimer must be the basis for trimer formation unless even rarer four-body collisions are to be considered. However, both the dimer and trimer curves of growth level off at higher pressures, indicating that these species are either not being as readily formed, or are themselves being lost to secondary clustering. In addition, the curve of growth for the background continues to increase with backing pressure. This suggests that as larger and larger clusters are formed, the cluster formation process takes on a qualitatively different form than the three-body collision model.

To highlight this, the integrated absorbances from Fig. 2.28 are turned into absolute concentrations of CO_2 in each cluster, making the assumption that the infrared oscillator strength of the CO_2 ν_3 asymmetric stretch changes little upon complexation.

Table 2.1: Degree of $(\text{CO}_2)_n$ clustering as a function of stagnation pressure P_0 . (Conditions: 2% CO_2 in He)

| P_0 (torr) | Percentage of | Percentage of total CO_2 in: | | |
|--------------|--------------------|---------------------------------------|-------------------|-------------------------|
| | monomer clustered | $(\text{CO}_2)_2$ | $(\text{CO}_2)_3$ | Background ^a |
| 400 | < 5.0 ^b | 0.8 | 0.2 | 0.8 |
| 500 | ... ^c | 1.0 | 0.4 | 1.8 |
| 600 | < 5.0 | 1.2 | 0.7 | 3.3 |
| 700 | ... | 1.5 | 0.8 | 6.1 |
| 800 | 5.2 | 1.7 | 1.1 | 8.5 |
| 900 | ... | 1.8 | 1.1 | 11.3 |
| 1000 | 22.5 | 1.7 | 1.2 | 15.1 |
| 1100 | ... | 1.7 | 1.2 | 19.1 |
| 1200 | 54.0 | 1.7 | 1.2 | 22.6 |
| 1300 | ... | 1.6 | 1.1 | 25.0 |
| 1400 | ... | 1.5 | 1.0 | 27.5 |

^aThe background is a broad absorption centered about $2353.26 \pm 0.25 \text{ cm}^{-1}$ with a FWHM of approximately 4 cm^{-1} .

^bThe absolute accuracy should be taken as approximately ± 0.5 of the stated values. See the text for assumptions made in the analysis.

^cMeasurements were not made at these stagnation pressures for the monomer.

This is done based on measured rotational temperatures in the expansion and Hönl-London factors from theory. For the broad background absorption, the peak height at $2353.26(25) \text{ cm}^{-1}$ times the FWHM of $\approx 4 \text{ cm}^{-1}$ is taken as the integrated absorbance. The results are presented in Table 2.1.

As can be seen, when clustering initially begins in the expansion at $P_0 \sim 500$ torr, only a few percent of the monomer ends up in clusters, in agreement with the three-body collision model. For higher pressures, the concentration of CO_2 in the dimer and trimer remains remarkably constant at a few percent, but the large clusters take off. (The discrepancy between the monomer lost to clusters and the sum of the

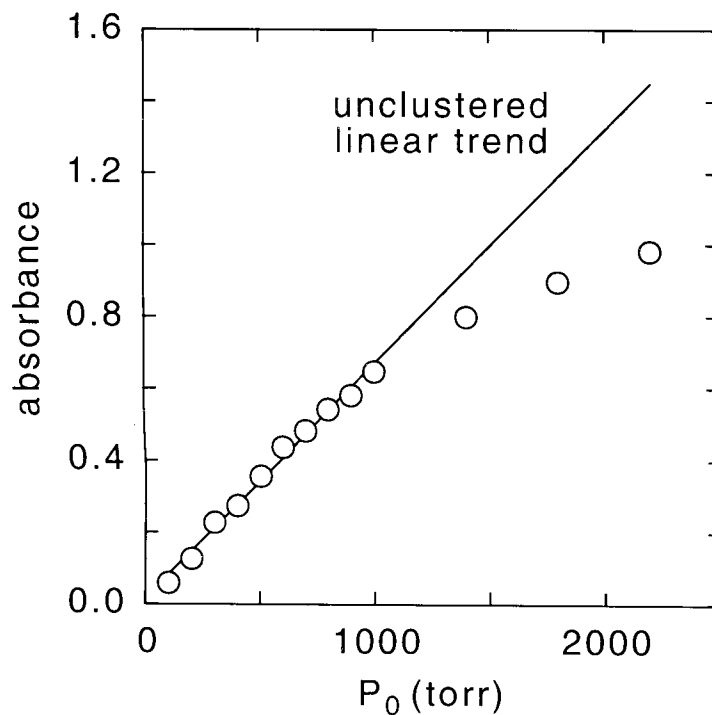


Fig. 2.29: CO_2 monomer curve of growth for pinhole expansion. (Conditions: 10% CO_2 in He, $d^* = 150 \mu\text{m}$).

three cluster sizes considered here is just a statement that several intermediate cluster sizes are being populated as well that are not considered in the analysis.)

The rapid growth of the large clusters can be viewed as the onset of "snowballing." Above a certain cluster size, the binding energy of the cluster and the density of cluster vibrational states is high enough that the excess collisional energy involved in a two body collision can be readily absorbed by the large cluster. These larger clusters then "sweep" through the expansion, picking up smaller clusters and monomers as they go via the much more frequent two body collisions. This is one possible explanation for the dramatic increase in clustering at higher pressures over that predicted by three-body collision rates.

As a final note, the relative $(\text{CO}_2)_n$ cluster formation in a pinhole and slit expansion is compared. Shown in Fig. 2.29 is the CO_2 monomer curve of growth for

10% CO₂ in He expanded through a 150 μm pinhole nozzle. Even though the concentration of CO₂ in the stagnation mixture is a factor of five greater than for the slit expansion monomer curve of growth in Fig. 2.28, significant clustering of the monomer is only observed at $P_0 \gtrsim 1500$ torr in the pinhole expansion. This is a clear example of the enhancement in clustering due to the slower density drop off in the slit expansion as opposed to the pinhole.

2.9 Measuring alignment

As discussed in detail in Chapter 3, it is possible to determine the second moment of the M_J distribution, *i.e.*, the alignment, by measuring the difference in absorbance for light linearly polarized parallel and perpendicular to the quantization axis. In the present section we present the details for rotating the polarization of the laser light and extracting the difference in absorbance.

The polarization of the laser light is rotated at 75 kHz between orthogonal linear polarizations using a photoelastic modulator (PEM). This rapid rotation is advantageous for two reasons. First, in the supersonic expansion experiments, the polarization is rotated ≈ 40 times during the 500 μs pulse from the pulsed valve. The alignment can thus be measured within one pulse, minimizing effects due to pulse to pulse fluctuations. Second, the alignment information is encoded at 75 kHz. At these frequencies the laser/detector noise is within a factor of two of the shot noise limit; by using sensitive lock-in techniques very weak alignment signals can be measured.

The PEM (Hinds International, PEM-80 ZS) consists of an octagonal ZnSe crystal that is brought into a resonant oscillation of 37.5 kHz by two piezo transducers, as shown in Fig. 2.30. When the crystal oscillates, it experiences either a compression or expansion along its two principle axes. Due to stress induced birefringence, the index of refraction changes along the principle axes. If light is brought into the crystal

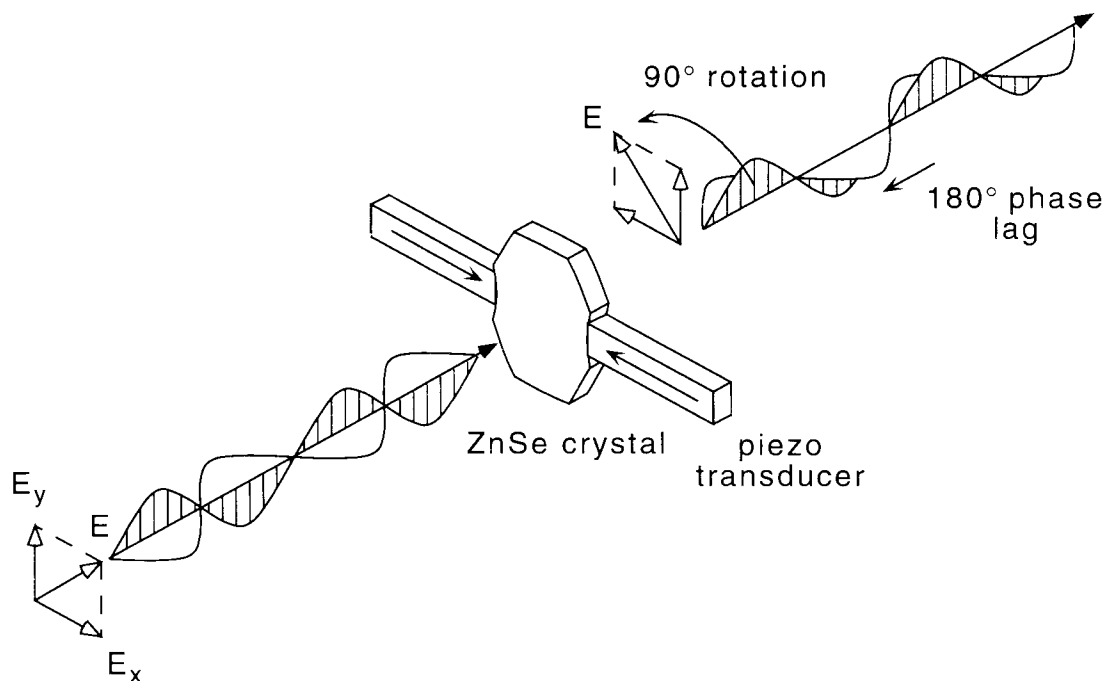


Fig. 2.30: Polarization rotation by the PEM. The piezo transducers set the ZnSe crystal into resonant oscillation. When the incident light is brought in at 45° with respect to the crystal's principle axes, the compression/expansion stress induced birefringence leads to a phase lag between the two polarizations, which is equivalent to rotating the polarization.

linearly polarized 45° with respect to the principle axes, then the electric field of the light can be viewed as being decomposed into a linear combination of two electric fields along the principle axes. As shown in Fig. 2.30, the changing index of refraction causes the phase of these electric fields to lead or lag one another, *i.e.*, they are phase shifted. The amount of phase shift increases with the stress, and at some value the shift is 180° . This corresponds to the polarization being rotated 90° . For large enough oscillations of the crystal, the 180° phase shift occurs twice during the oscillation period, so the polarization is rotated at 75 kHz.

During the oscillation of the crystal, the stress induced birefringence goes smoothly from zero to the value needed to rotate the polarization 90° . Therefore, the polarization of the light is also rotated through elliptical and circular polarizations

corresponding to different stress induced phase shifts. The PEM must first be set so that the crystal oscillation amplitude corresponds to a 90° rotation of the polarization. To do so, first the laser light is brought into the PEM linearly polarized at 45° with respect to the principle axes of the crystal. This is accomplished by passing the laser first through a MgF_2 Rochon polarizer (Karl Lambrecht, MFRV-9). Then a second MgF_2 Rochon polarizer is placed after the PEM at right angles to the first polarizer. With the PEM off, no light is transmitted through the crossed polarizer configuration. The PEM is then turned on, and the oscillation amplitude increased while viewing the transmitted light on a detector. A 75 kHz nearly sinusoidal wave will be observed, which will increase in amplitude until the oscillation magnitude corresponding to 90° rotation is reached. The oscillation magnitude can be increased further, but the amplitude of the transmitted light will not increase. Instead, the PEM is now rotating the light through 90° , and then on to further elliptical polarizations. The transmitted light will no longer have a near sinusoidal pattern.

Once the polarization is being rotated a full 90° , and the PEM is oriented with respect to the quantization axis of interest, an alignment measurement can be made. Consider alignment in a pulsed pinhole expansion. The collisionally aligned molecules result in a greater amount of light linearly polarized parallel to the expansion axis to be absorbed than light perpendicularly polarized. Hence an (exaggerated) absorption pulse might look like that in Fig. 2.31. The overall shape of the absorption is apparent, but the difference in absorbance between the two polarizations shows up as an oscillation on the pulse. Two quantities are of interest to determine the alignment. The first is the total absorbance for the two polarizations, *i.e.*, $A_{\parallel} + A_{\perp}$, and the second is the difference between the two, *i.e.*, $A_{\parallel} - A_{\perp}$. The first quantity can be determined by integrating the absorption pulse (discussed further in the data acquisition section). The second quantity can be determined as shown in Fig. 2.31. The raw signal is filtered to

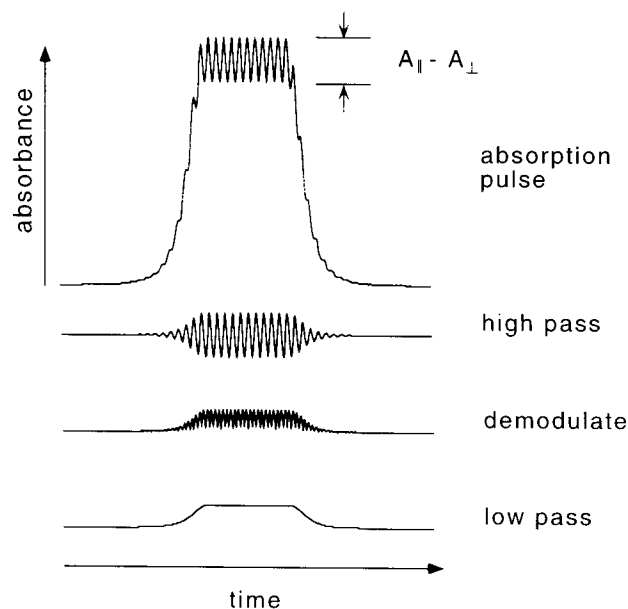


Fig. 2.31: Extracting polarization-dependent absorbance from an absorption signal.

isolate the 75 kHz signal, then rectified by heterodyning it against a 75 kHz reference signal at the correct phase. The high frequency components are then filtered to obtain an "alignment pulse" that is proportional to $A_{||} - A_{\perp}$.

This process is carried out by the phase sensitive polarization signal demodulator; a circuit diagram is shown in Fig. 2.32. Electronically, the process in Fig. 2.31 is carried out via standard lock-in techniques. A commercial instrument is not used for this because the fast time constant necessary to capture the transient absorption pulse is (presently) not available on standard lock-ins. In order to use the demodulator, the correct phase between the reference 75 kHz signal from the PEM and the measured signal must be set. To do this, once again use the crossed polarizer configuration. The polarizers can be set so that the maximum attenuation of light occurs when the polarization is parallel with the quantization axis. The signal from the crossed polarization configuration is sent to the demodulator. Then, using the phase settings in Table 2.2, the demodulated signal is first minimized and the phase recorded

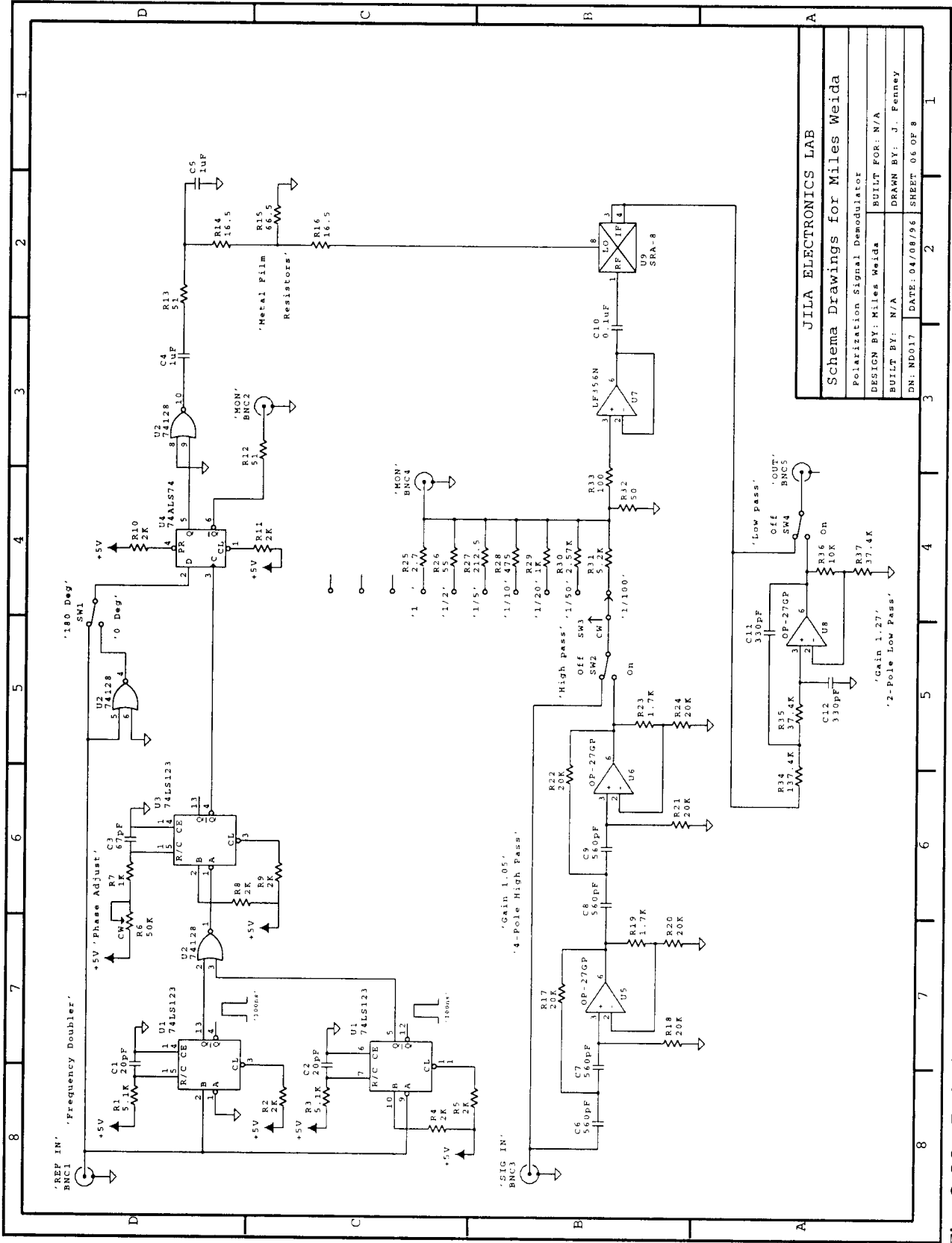


Fig. 2.32: Polarization signal demodulator.

Table 2.2: Phase shift settings for polarization signal demodulator (at 75 kHz).

| Phase shift: | Dial reads: | Phase shift: | Dial reads: |
|----------------------|-------------|------------------------|-------------|
| min \rightarrow 8° | 0 | 90° | 286 |
| 10° | 8 | 100° | 321 |
| 20° | 45 | 110° | 354 |
| 30° | 82 | 120° | 387 |
| 40° | 118 | 130° | 421 |
| 50° | 152 | 140° | 456 |
| 60° | 186 | 150° | 492 |
| 70° | 221 | 160° | 530 |
| 80° | 253 | max \rightarrow 170° | 569 |

at which this occurs. The phase is then set to a value 90° from this to optimize the signal, just like a standard lock-in is optimized. The signal from the demodulator can then be calibrated to the actual peak to peak amplitude modulation by comparing both the raw and demodulated signals on an oscilloscope.

Although this is everything that needs to be done to make an alignment measurement as discussed in the data acquisition section, there are a few additional corrections that need to be made to the demodulated signal. The first is due to the finite bandwidth of the detector/amplifier combination. For example, the InSb PV detectors used in the CO₂ experiments have a -3 dB point of 120 kHz. This leads to a 14.6% attenuation of the signal at 75 kHz. The final demodulated signal must be corrected by this amount.

The second correction is due to stray birefringence in the optical path and strong absorption pulses. Stray birefringence can result in amplitude modulation of the laser light by 0.1% - 0.5% that is synchronous with the PEM modulation. As highly exaggerated in Fig. 2.33, this amplitude modulation can lead to an offset of the demodulated signal. This would not be bad in and of itself, but when there is a strong

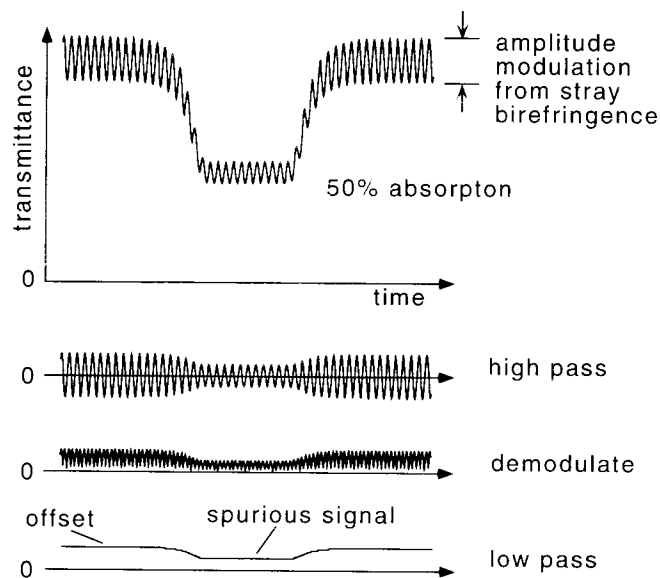


Fig. 2.33: Spurious alignment signal resulting from stray birefringence plus an absorption.

absorption of the light, the peak to peak amplitude of the modulation due to stray birefringence decreases by an amount proportional to the absorption. As shown in Fig. 2.33, this leads to a dip in the offset demodulated signal that appears to be an alignment signal. To correct for this, the dc offset of the demodulated signal and the fractional attenuation are recorded for each pulse. The corresponding correction for this dip is then added to the demodulated signal.

As a final note of caution, optical feedback from the PEM or elements down beam from the PEM can lead to spurious alignment signals. Because an absorption line shape makes an excellent frequency to amplitude transducer, this type of spurious signal occurs when scanning over an absorption. The appearance of this type of signal varies from pulse to pulse, but because the sign of the transducer is opposite for the two sides of the absorption profile, the spurious signals have a mirror symmetry about the peak center when scanning over the absorption profile. This can be avoided by

using the same techniques discussed above for reducing optical feedback to the diode laser.

2.10 Sublimation studies

The sublimation experiment is described in detail in Chapter 9. In the present section we therefore concentrate on the construction of the sublimation plate, temperature measurement, and temperature control. In addition, details concerning the growing of surfaces will be considered. A drawing of the sublimation plate assembly is shown in Fig. 2.34. The plates and thermal conduit from the liquid N₂ cold finger to the sublimation plate are all made of oxygen-free high-conductivity (OFHC) copper. All thermal connections are made with indium foil. A thin Teflon spacer is inserted in the thermal conduit, as shown in Fig. 2.34, to increase the thermal resistance between the cold finger and the sublimation plate. This enables us to heat the sublimation plate from 80 to 120 K while keeping the catch plate at < 80 K. The 75 μm width of this spacer was chosen to maximize cooling rates for the sublimation plate while maintaining sufficient thermal isolation from the catch plate.

The temperature of the sublimation plate is measured with two Si diode temperature sensors (Omega CY7 Series). The diodes are placed at the middle and end of the sublimation plate to check for nonuniform temperatures across the plate. Temperature can be measured with the diodes because the voltage drop across the p-n junction is temperature dependent. As shown in Fig. 2.3, the voltage drop is due to the depletion region in the diode. The lower the temperature, the less thermal energy the mobile electrons and holes have to diffuse, and the depletion region becomes larger, *i.e.*, the voltage drop increases. The diodes used in the present experiment are provided with a voltage to temperature conversion factor, and have an accuracy of ± 0.5 K and precision of ± 1 mK. To operate the temperature sensors, 10 μA ± 0.05%

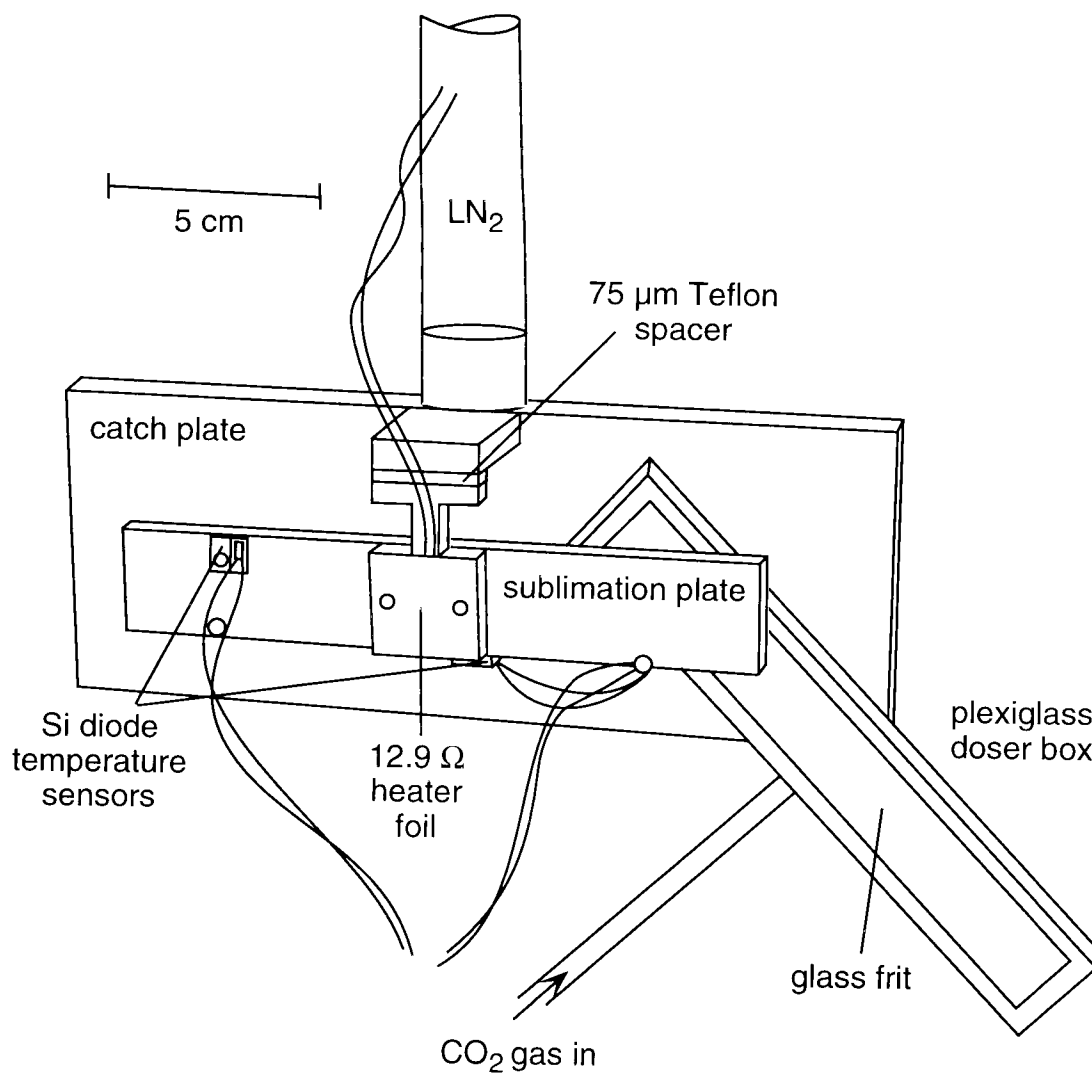


Fig. 2.34: Sublimation plate assembly with doser box. The doser box can be rotated so that it is flush with the sublimation plate to grow surfaces. It can then be rotated out of the optical path. An additional Cu shroud (not shown) is thermally attached to the back of the catch plate.

is driven across the diode, and the voltage is measured using a sensitive instrumentation amplifier; the circuit is shown in Fig. 2.35. The current supplied to the diode is set by measuring the voltage across a reference resistor with a microvoltmeter. The trimpot for the LM334 current supply is then adjusted until the current falls within the stated tolerance for the temperature conversions to be valid.

The temperature of the sublimation plate is controlled via the proportional and integral (PI) servo shown in Fig. 2.36. This servo zeroes the difference between the set point and the temperature sensor voltage. It can drive up to 0.93 A through the 12.9 Ω heater foil attached to the back of the sublimation plate. The temperature stability of the sublimation plate with the servo loop is measured to be $\lesssim 5$ mK over 10 minutes. With the maximum heater current of 0.93 A, the heating rate of the sublimation plate between 95 and 100 K is 125 mK/s, while the maximum cooling rate over this range with the heater off is 38 mK/s.

Surfaces are grown on the sublimation plate by swinging the doser box in Fig. 2.34 up to the plate, then pulling it tight against the plate. The plexiglass doser box has a recessed (5mm) glass frit with an average pore size of 10 μm . CO_2 gas is supplied to the opposite side of the frit, and the surfaces are typically grown at rates of 10^4 monolayers (ML)/sec for 100 sec. During this time, the sublimation plate rises in temperature from 80 to 95 K. The resulting surfaces appear uniform and "frosty." As discussed in Chapter 9, the characteristics of the surface do not depend on the growth conditions. We note for future reference, however, that identical tests were also carried out with surfaces grown using a frit with an average pore size of 50 μm . At growth rates of $\geq 10^4$ ML/s, the resulting surfaces were shiny and smooth, and highly fractured, *i.e.*, a visible network of cracks were observed across the top of the surface. Presumably these cracks penetrated through the entire thin film thickness. The flux from these surfaces was considerably less than for the surfaces grown with the fine frit

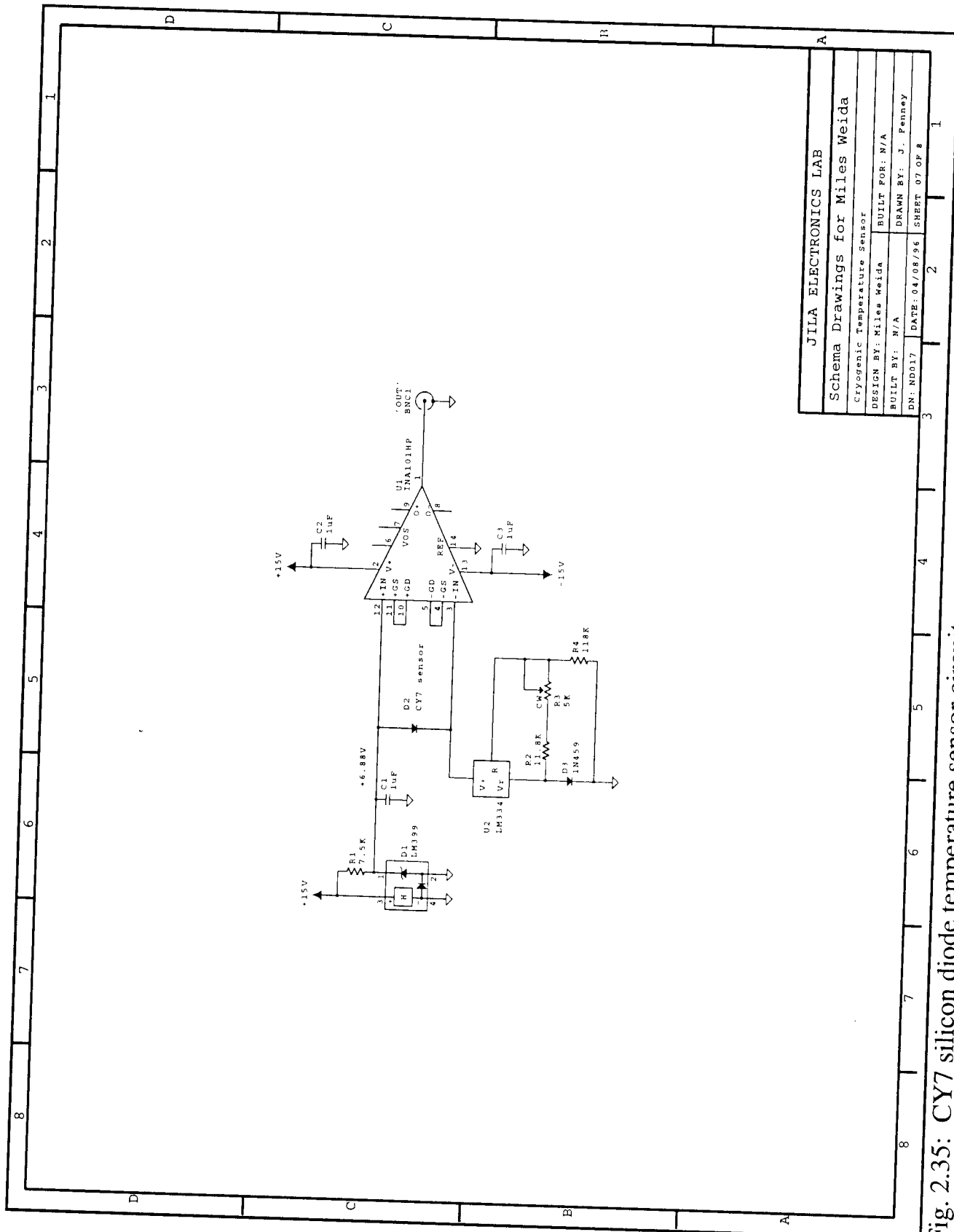
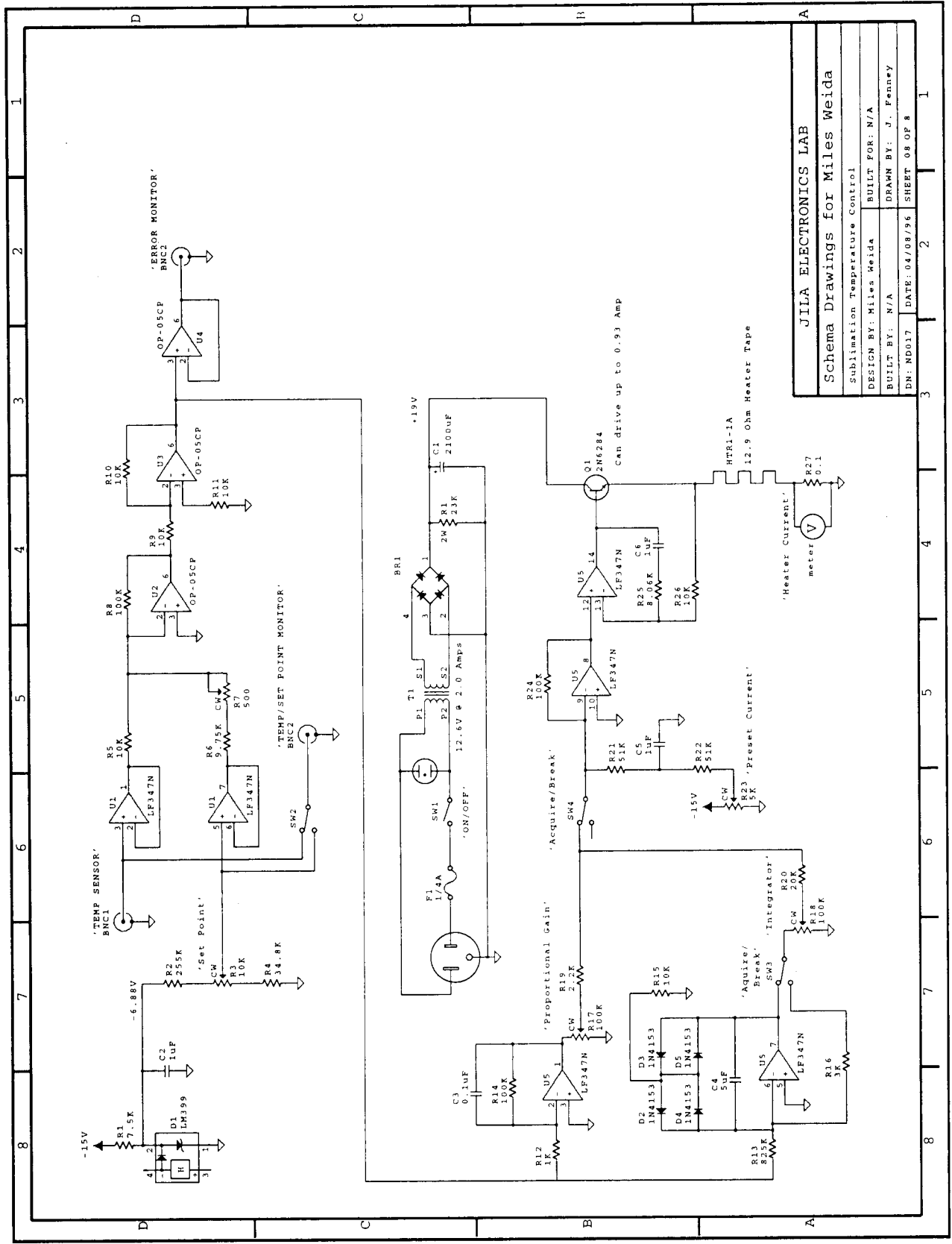


Fig. 2.35: CY7 silicon diode temperature sensor circuit.

| | |
|---------------------------------|---------------------|
| JILA ELECTRONICS LAB | |
| Schema Drawings for Miles Weida | |
| Cryogenic Temperature Sensor | |
| DESIGN BY: Miles Weida | BUILT FOR: N/A |
| BUILT BY: N/A | DRAWN BY: J. Fenney |
| DN: N0017 | DATE: 04/08/96 |
| SHEET 07 OF 8 | |



| | |
|---------------------------------|---------------------|
| JILA ELECTRONICS LAB | |
| Sublimation Temperature Control | |
| Schema Drawings for Miles Weida | |
| DESIGN BY: Miles Weida | BUILT FOR: N/A |
| BUILT BY: N/A | DRAWN BY: J. Fenney |
| DN: MD017 | DATE: 04/08/96 |
| | SHEET 08 OF 8 |

Fig. 2.36: Sublimation plate temperature servo.

under identical conditions. However, thin films grown at rates of $< 10^4$ ML/s with the coarse frit had fluxes identical to those grown with the fine frit. We believe that the quickly grown surfaces from the coarse frit fractured and had poor thermal contact with the sublimation plate. Therefore, the fine frit was used exclusively in the experiment.

2.11 Data acquisition

There are three different types of data acquisition routines used in the different experiments in this thesis. The first is for the acquisition of high resolution spectra of weakly bond complexes. It involves stepping the laser frequency by discrete amounts and acquiring an absorption signal as well as diagnostic information at each step; this will be called a standard scan. The second scheme is for the measurement of alignment in supersonic expansions. It is qualitatively similar to the standard scan, except that an alignment signal is also collected at each frequency step; this will be called an alignment scan. The final scheme is used to measure the cw absorption signal from subliming molecules, and involves rapidly sweeping the laser frequency and recording an absorption, alignment, and etalon trace; this will be referred to as a sublimation scan. The remainder of this section is devoted to discussing these schemes in more detail.

2.11.1 Standard scan

For the standard scan, the data acquisition is controlled by a micro-computer (Gateway 2000 75 MHz Pentium), which communicates with a digital oscilloscope (Tektronix 2430A) and two analog lock-in detectors (Stanford Research Systems SR510) via a GPIB card (National Instruments GPIB-PCIIA (488.2)). The GPIB (general purpose interface bus) system is chosen for its ease of use and high level commands for controlling the oscilloscope and lock-in detectors. The lock-ins also

have two 13 bit D/A outputs and four 13 bit A/D inputs that are controlled via the GPIB interface. The diode laser frequency is controlled via one of the D/A outputs: the D/A voltage is fed first to a variable attenuator for fine control of the step size, then to the external modulation input on the diode laser current supply. The computer can then send a command to the lock-in to step the D/A voltage by a certain amount, which then steps the diode laser frequency.

The procedure for the standard scan is as follows. First, begin pulsing the valve. This is done by sending a square wave trigger signal from a function generator (Wavetek model 144) to the slit valve pulse driver in external trigger mode. The repetition rate (typically between 1 and 20 Hz depending on the gas load) of the slit valve is controlled by this function generator, and the same trigger signal is sent to the digital oscilloscope. Next, put the computer into data acquisition mode by running the program SCAN.BAS. The computer resets the laser frequency and prompts the user for various scan parameters, such as laser step size, number of pulses to average, and the position of the integration gates for the absorption pulse (discussed subsequently).

The computer then sends a signal to the oscilloscope to begin acquiring absorption pulses. The oscilloscope is triggered from the function generator and acquires the number of absorption traces specified by the computer. These traces are averaged, digitized, and sent to the computer. Simultaneously, the computer acquires the demodulated reference gas and etalon fringe signal from the lock-in detectors. The absorption pulse is then integrated, and the absorption, reference gas, and etalon signal are stored in the computer memory. The computer then steps the diode laser frequency, and repeats this process. The diode laser step size is chosen to be *at least* a factor of three smaller than the FWHM of the absorption profile. A sample scan containing the absorption signal, etalon fringes, and reference gas trace is shown in Fig. 2.37. When

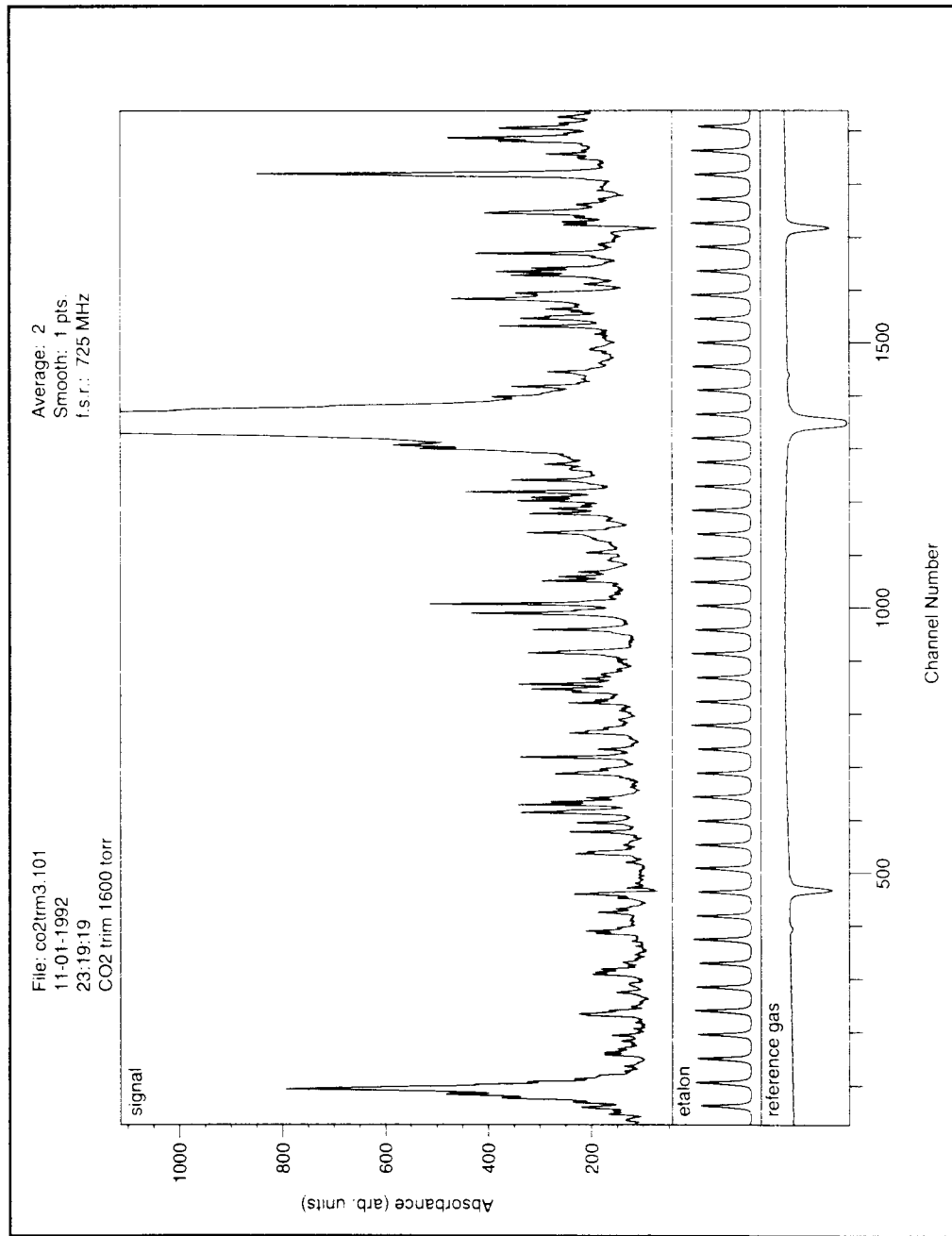


Fig. 2.37: Sample scan over the spectral region containing Q -branches of $(\text{CO}_2)_2$ and cyclic $(\text{CO}_2)_3$. The large absorption is $R(2)$ of CO_2 monomer. The scan step size is 16 MHz.

the scan is finished, a final data file is transferred to floppy disk. The format of the data file is presented in Appendix A.

To extract the absorption information from the transient absorption pulse, an integration scheme is used. The digitized pulse is broken up into three parts: two baseline gates and a signal gate, as shown in Fig. 2.27. The absorption pulse is then integrated by subtracting a baseline, fit between the two base gates, from the signal gate, *i.e.*,

$$\text{signal} = \frac{1}{N_{\text{sig}}} \sum_{i=1}^{N_{\text{sig}}} \text{sig}(x_i) - \frac{1}{2N_{\text{base}}} \left(\sum_{i=1}^{N_{\text{base}}} \text{base1}(x_i) + \sum_{i=1}^{N_{\text{base}}} \text{base2}(x_i) \right). \quad (2.5)$$

Here, $\text{sig}(x)$ is the array containing the digitized signal gate information, and N_{sig} is the number of points in the array. The definitions for the base gates are similar. The baseline integration scheme effectively filters low frequency fluctuations in the baseline. The computer program allows one to adjust the position and length of the different gates for maximum noise rejection. Typically, a signal gate of 400 μs is used, with base gates of length 200 μs each. The base gates are positioned as close as possible to the leading and trailing edge of the pulse.

Finally, information for the power scaling of the absorption signal is also collected during the scan. This can take two forms, depending on the experiment. For the CO_2 experiments, the detectors are InSb PV detectors, which record a dc signal that is proportional to the power incident on the detector. This dc level is recorded by feeding the dc signal out (prior to AC filtering and subtraction) from the subtraction circuit in Fig. 2.15 to one of the lock-in A/D inputs. The computer then records the dc light level in volts for each laser step. Since the detectors have a dc offset due to background blackbody radiation alone, the computer also prompts the user for this offset value (recorded in a separate measurement) to subtract from the recorded dc level to obtain the true dc light level. Since the absorption pulse is also recorded in volts by

the oscilloscope, it is simple to scale the absorption data to retrieve the absorbance, first taking into account the factor of 100 gain introduced in the subtraction circuit.

For the H₂O experiments, the signal detector is a HgCdTe PC detector, and the output is ac coupled. Hence, the above procedure cannot be used to record the power level. Instead, the demodulated reference gas signal is used for this purpose. Barring beam steering effects during the scan, the light level on the reference gas detector is proportional to the light level on the signal detector. Since the reference gas signal is first chopped and then demodulated, the dc level information is present. Therefore, before the scan, the proportionality constant between the light level on the signal detector and the demodulated reference gas detector on the lock-in is determined by chopping the light incident on the signal detector. This proportionality factor can then be used in the data analysis section to scale the recorded absorption pulses to retrieve the absolute absorbance.

2.11.2 Alignment scan

The same acquisition procedure is used for the alignment scan as for the standard scan. The only difference is that the demodulated alignment signal (as discussed in Sec. 2.9) is input into channel two of the digital oscilloscope. The scope then digitizes both the absorption and alignment pulses and sends them to the computer. The baseline integration scheme is carried out on both the absorption and alignment pulses, and the resulting signals are recorded along with the etalon fringes and reference gas trace. The program that handles this is called ALSCAN.BAS; the data format for files from this program is covered in Appendix A.

Power measurements are also different. Since each alignment scan is over a single ~ 200 MHz FWHM monomer absorption profile, the light level does not change significantly over the course of the scan. Thus, the light level at line center is recorded

before starting each scan by chopping the signal light. This information is recorded along with the data file to accurately scale the measured signals. The ALSCAN program also uses this information to correct for spurious alignment signals due to stray birefringence, as discussed in Sec. 2.9.

2.11.3 Sublimation scan

As opposed to the other experiments, the absorption signal due to the subliming molecules is cw. Hence the laser frequency is swept over the absorption profile (5 ms over ~ 2.5 GHz) by inputting a sawtooth voltage wave from the function generator into the external modulation input of the diode laser current supply. The oscilloscope is then simultaneously triggered by the function generator, and acquires a scan over the absorption profile and etalon fringes. This is digitized and sent to the computer for storage. For the sublimation alignment measurements, first the absorption signal is recorded, then the demodulated alignment signal in a separate measurement, since three traces (including the etalon fringes) cannot be recorded simultaneously. The program that handles this is called SUBLIME.BAS, and the data file format is covered in Appendix 1. The acquisition procedure, though quite simple, has proven to be remarkably stable in frequency. Although one could trigger the data acquisition sweep from an etalon fringe, this has not been found to be necessary. Multiple averages of sweeps taken over a 10 s period show no discernible broadening of the ≈ 75 MHz FWHM absorption profile.

Power measurements are made by rapidly subliming away a thin film so that the transition of interest is optically black. The peak height of this saturated signal corresponds to the light intensity on the signal detector, and can be used to scale the recorded sublimation signals to retrieve absorbance information. This procedure ensures that the measured signals are correctly scaled to the light level in the diode laser

mode of interest, since ~ 5% of the total light power is sometimes in secondary diode modes.

For each sweep over an absorption profile, both the temperature of the sublimation plate and the background pressure in the chamber as measured by the ion gauge (Varian Vacuum Ionization Gauge, model 843) are recorded via the A/D inputs on one of the lock-ins. These raw signals are scaled using simple algorithms supplied by the manufacturers (Omega for the temperature sensors, Varian for the ionization gauge) to obtain the true temperature and pressure. For the temperature programmed desorption (TPD) experiments, the sublimation plate is either continuously heated by providing a constant current, or cooled by reducing the current, and the computer monitors the temperature of the plate and starts data acquisition at specified temperature or time intervals. The program that handles this is called TPD.BAS, and the data file format is covered in Appendix A.

2.12 Data analysis

2.12.1 Standard scan

As seen in Fig. 2.37, the standard scan is recorded as a function of channel number, *i.e.*, frequency steps of the diode laser. It is necessary to convert this into frequency before the peak positions and line shapes can be determined. This is done in two ways, depending on whether the unstabilized marker cavity is being used in the CO₂ experiments, or the stabilized marker cavity is used for the H₂O experiments. For the unstabilized cavity, the analysis program used is called SPECTRA.BAS; first the etalon fringe peaks are located as a function of channel number. A simple peak finding algorithm is implemented that locates the maximum of each etalon fringe above a specified level. The maximum and two points located to either side of the maximum are then fit to a parabola to more accurately determine the fringe center. The fringe center

in channel numbers is then stored for all fringes in an array. Next, two reference peaks are chosen from the reference gas trace. These are typically two peaks with well defined centers and well separated in the scan; in Fig. 2.37, they would be the two smaller "hot band" peaks on either side of the strong monomer fundamental absorption. The center of these peaks is determined using the same algorithm for finding the etalon fringe center. The channel number of the reference peaks is then stored, as well as the frequency⁹ of each peak.

After this is complete, the fsr of the etalon is determined by dividing the frequency separation of the two reference peaks by the number of etalon fringes between them. Fractional spacings on the ends are determined by linear interpolation between two fringes. If there are not two sufficiently separated reference peaks in the same scan, the fsr from a scan made very near in time to the scan of interest is used instead. Once these steps are finished, it is relatively straightforward to assign a frequency to each channel number. The number of etalon fringes between the channel number of interest and one of the reference peaks is determined by counting integral fringes, and using linear interpolation for fractional spacings on the ends. This is then multiplied by the fsr and added or subtracted from the reference peak frequency to determine the frequency of the channel number.

For the stabilized cavity H₂O experiments, the procedure for assigning frequencies to each channel is very similar. The etalon fringe centers are found in the same manner as above. But now one of the actual etalon fringes is used as the reference peak. The only trick is to determine the frequency of this "reference fringe" in the scan. To do this first an *absolute* reference fringe is chosen; this fringe is separate from the reference fringe used in a particular scan, and is the foundation for all frequency measurements made with the stabilized cavity. The absolute reference fringe is measured relative to an H₂¹⁷O or H₂¹⁸O monomer transition in the slit jet. For

consistency, these reference fringes are always chosen to be the first fringe to the red, *i.e.*, lower frequency, from the reference peak. Since the fsr of the stabilized cavity is accurately known, linear interpolation can be used to determine the frequency for the absolute reference fringe using the program FRINGE.BAS. This measurement is made several times to assign the absolute reference fringe as accurately as possible.

Next, the frequency of the reference fringe in a particular scan is assigned using the absolute reference fringe. First, the approximate frequency position of the reference fringe is determined from a reference gas absorption or an assigned absorption in the signal trace using the same procedure as above. The difference between this approximate frequency for the reference fringe and the absolute reference fringe frequency is then divided by the fsr to determine the number of integral fringes between the two. The resulting number is typically within 0.1 of an integral number. This unambiguously identifies the number of integral fringes between the two, and the reference fringe frequency is then assigned by multiplying the number of fringes by the fsr and then adding or subtracting this from the absolute fringe frequency.

Once the frequency of each channel number can be assigned, peak positions can be determined. The channel number of the center of each peak is determined by fitting the peak maximum plus two points to either side to a parabola. These peaks are presmoothed using a Pascal's triangle smoothing algorithm to minimize the effects of amplitude fluctuations on this analysis. There is also the option in the programs SPECTRA.BAS for the unstabilized cavity and CAVITY.BAS for the stabilized cavity to specify the peak position in terms of integral channel number if necessary. The frequency of each peak is then calculated by counting the number of etalon fringes to the reference peak or fringe, with fractional spacings once again being determined by linear interpolation between two fringes. It is also possible to extract line shape information by saving a particular peak as a text file of absorbance vs. frequency (this

is a self explanatory option in the analysis programs) that can then be used with the group line shape fitting routines in the B212 account.

Lastly, the vertical scale of the standard scan can be scaled to obtain the absorbance. For the CO₂ measurements, the total infrared power is stored in the data file for each frequency step, and the analysis program uses this to scale the signal. For the H₂O measurements, the reference gas trace times the appropriate scale factor (see Sec. 2.11.1) is used to scale the signal. The analysis program has an option to excise the absorption peaks from the reference gas trace so that it can be used for this purpose. Once the vertical axis is scaled to the absorbance, it is possible to determine the integrated absorbance of spectral features using the self explanatory options in the analysis programs. This is very useful information for determining absolute concentrations of species in the expansion.

2.12.2 Alignment scan

For the alignment scans, it is not necessary to measure the absolute frequency of the scanned CO₂ monomer transitions, since these are already known. Instead, the relevant frequency axis is the shift from line center. The line shapes are recorded such that they are surrounded by two etalon fringes. The peak center is obtained from the reference gas trace, and the shift from line center is determined via linear interpolation between the two etalon fringes. This procedure is carried out using the analysis program ALIGN.BAS; a sample print out from this program is shown in Fig. 2.38 with the frequency shift assigned for the absorption signal (bottom trace) and the demodulated alignment signal (top trace). The results are presented in actual volts, which are then scaled with the known calibration factor for the demodulated signal and the recorded infrared light level. In this way, the relevant alignment information, *i.e.*, $P = (A_{\parallel} - A_{\perp}) / (A_{\parallel} + A_{\perp})$, can be determined.

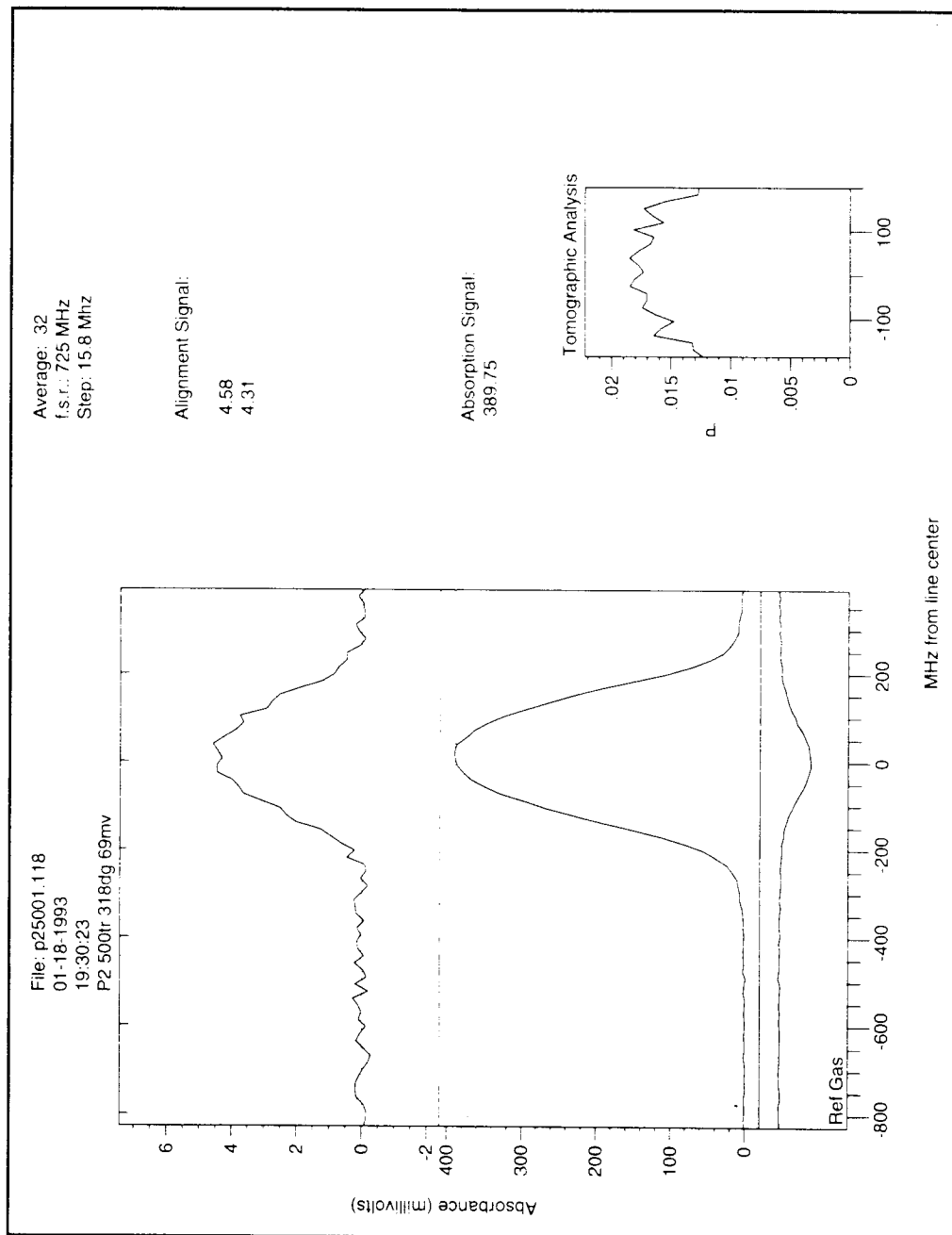


Fig. 2.38: Sample output from alignment scan analysis program. The absorption pulse and demodulated alignment signal are recorded in volts, which can be scaled to retrieve the polarizance as a function of frequency shift.

A "tomographic analysis" is also carried out for each scan. In addition to measuring the alignment at line center, the alignment as a function of position in the supersonic expansion is of interest. The position in the beam can be related to the Doppler shift from line center. Hence by determining P as a function of frequency shift, a slice can be taken through the beam. The analysis program carries out a tomographic analysis by dividing the demodulated signal by the absorption signal for each frequency shift. This is an approximate analysis meant to alert the user to any significant variations in alignment across the beam profile. The tomographic analysis is also printed out for quick visual reference, as shown in Fig. 2.38.

2.12.3 Sublimation scan

Similar to the alignment scans, only the frequency shift from line center is of interest for the sublimation scans. The sublimation line shapes are also recorded surrounded by two etalon fringes, so the same procedure as above is used to assign the frequency shift from line center. The program that handles this is called SUBAN.BAS. After the frequency shift is assigned, two quantities are of interest: the integrated absorbance of the peak and the line shape. However, for very weak sublimation signals, there are frequency dependent modulations of the baseline during a rapid scan, as shown in Fig. 2.39. These are due to changing infrared light level over the scan, or residual etaloning due to optical feedback to the diode laser.

Clearly the fluctuations in the baseline must be accounted for before accurate integrated absorbances and line shapes can be determined. To do so, the analysis program fits the baseline surrounding the absorption peak and then subtracts this from the entire signal. The baseline is fit to a quadratic polynomial to account for the gross offset, slope, and curvature. It is also fit to two sinusoidal components to account for the rapid oscillation due to etaloning. The period of these two oscillations from the

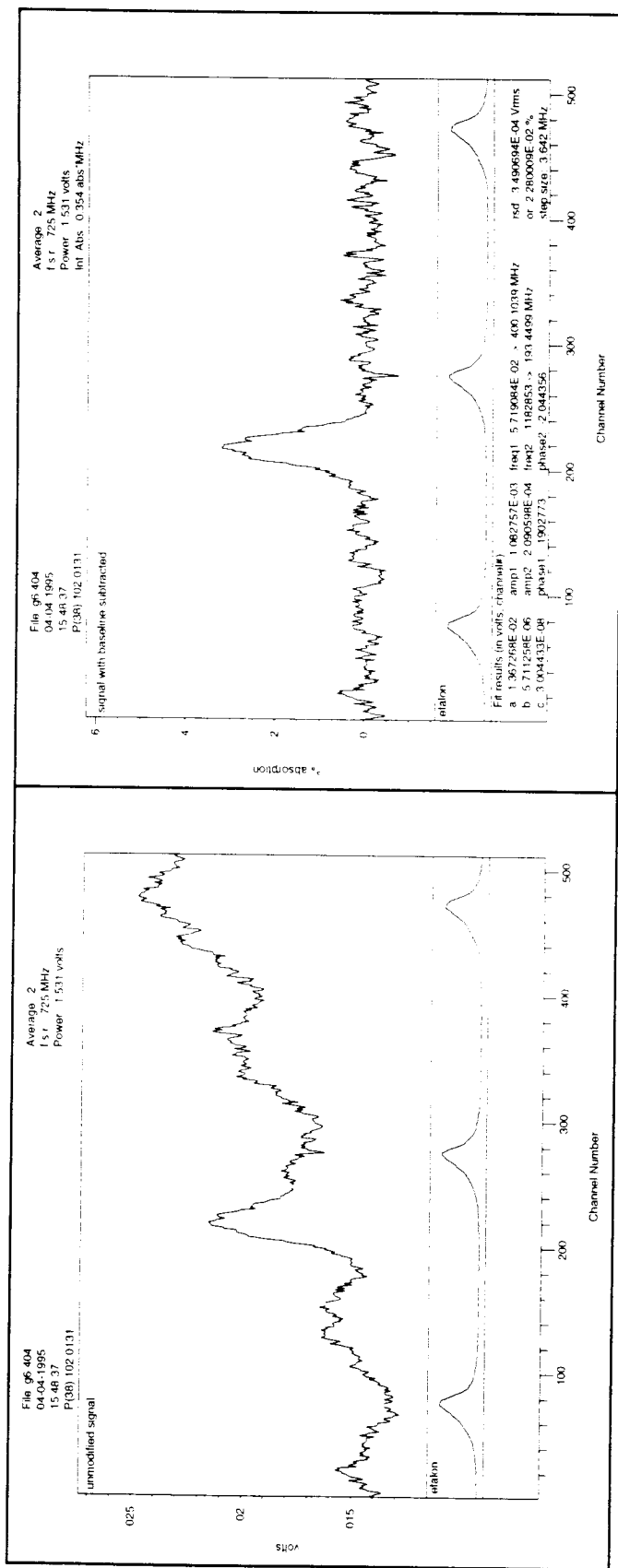


Fig. 2.39: Sample output from sublimation scan analysis program. The unmodified scan of P(38) of CO₂ subliming from a thin film has a sloping, curved baseline due to small changes in diode laser power over the scan. In addition, a sinusoidal pattern is present at these lowest signal levels due to residual etaloning. The baseline is fit to a sum of a second order polynomial and two sine waves of different phase and frequency. The baseline can then be subtracted to yield the true sublimation line shape.

least squares fit is found to be ≈ 400 MHz and ≈ 200 MHz. The results of the baseline subtraction are shown Fig. 2.39. The absorption signal is then scaled to the infrared light level to and integrated to obtain the integrated absorbance. Line shapes are saved to a text file of absorbance vs. frequency and then fit using the line shape analysis programs in the B212 account. Finally, small corrections to the integrated absorbance are made due to background 300 K CO₂ gas in the chamber. This process is discussed in Chapter 9.

References for Chapter 2

1. G. P. Agrawal and N. K. Dutta, Semiconductor Lasers, 2nd ed. (Van Nostrand Reinhold, New York, 1993).
2. W. W. Chow, S. W. Koch and M. Sargent III, Semiconductor-Laser Physics. (Springer-Verlag, Berlin, 1994).
3. G. H. B. Thompson, Physics of Semiconductor Laser Devices, (Wiley, New York, 1980).
4. C. E. Wieman and L. Hollberg, Rev. Sci. Instrum. **62**, 1 (1991).
5. K. B. MacAdam, A. Steinbach and C. Wieman, Am. J. Phys. **60**, 1098 (1992).
6. R. E. Simpson, Introductory Electronics for Scientists and Engineers, (Allyn and Bacon, Inc., Boston, 1987), p. 151.
7. C. H. Henry, IEEE J. Quantum Electron. **QE-18**, 259 (1982).
8. M. D. Schuder, Ph. D. thesis, University of Colorado, Boulder, 1991.
9. G. Guelachvili and K. N. Rao, Handbook of Infrared Standards, (Academic Press, Inc., Orlando, Florida, 1986).
10. E. Riedle, S. H. Ashworth, J. Farrell, J.T. and D. J. Nesbitt, Rev. Sci. Instrum. **65**, 42 (1994).
11. J. J. T. Farrell, Ph. D. thesis, University of Colorado, Boulder, 1995.
12. R. Balhorn, H. Kunzmann and F. Lebowsky, Appl. Opt. **11**, 742 (1972).
13. T. M. Niebauer, J. E. Faller, H. M. Godwin, J. L. Hall and R. L. Barger, Appl. Opt. **27**, 1285 (1988).
14. D. Kaur, A. M. de Souza, J. Wanna, S. A. Hammad, L. Mercorelli and D. S. Perry, Appl. Opt. **29**, 119 (1990).
15. G. Scoles, Atomic and Molecular Beam Methods, (Oxford University Press, New York, 1988).
16. C. M. Lovejoy, Ph. D. thesis, University of Colorado, Boulder, 1990.
17. G. Dupeyrat, in Rarefied Gas Dynamics, edited by S. S. Fisher, (AIAA, New York, 1981), Vol. 74, pp. 812-19.
18. C. M. Lovejoy and D. J. Nesbitt, Rev. Sci. Instrum. **58**, 807 (1987).
19. J. A. Barnes and T. E. Gough, J. Chem. Phys. **86**, 6012 (1987).